Realia et Realia naturalia

MADIS PAALO

Synthesis of CNT-metal oxide
nanocomposites: sol-gel process, rheology,
structural and functional properties

TARTU ÜLIKOOL · UNIVERSITAS TARTUENSIS · 1632

DISSERTATIONES SCIENTIAE MATERIALIS UNIVERSITATIS TARTUENSIS

9

MADIS PAALO

Synthesis of CNT-metal oxide nanocomposites: sol-gel process, rheology, structural and functional properties

Institute of Physics, Faculty of Science and Technology, University of Tartu, Estonia.

The dissertation was admitted on March 23, 2014 in partial fulfillment of the requirements for the degree of Doctor of Philosophy (material science), and allowed for defence by the Scientific Council on Material Science of the Faculty of Science and Technology of the University of Tartu.

Supervisors: Dr. Tanel Tätte, Institute of Physics, University of Tartu, Estonia;

Dr. Uno Mäeorg, Institute of Chemistry, University of Tartu, Estonia;

Dr. Ilmar Kink, Institute of Physics, University of Tartu, Estonia.

Opponents: Dr. Alex Rozhin, School of Engineering and Applied Science, Aston University, UK;

Dr. Mihkel Koel, Department of Chemistry, Faculty of Science, Tallinn University of Technology, Estonia.

Defence: April 30, 2014, University of Tartu (Tartu, Estonia)

CONTENTS

LIST OF ORIGINAL PUBLICATIONS

I. T. Tätte, M. Hussainov, **M. Paalo**, M. Part, R. Talviste, V. Kiisk, H. Mändar, K. Põhako, T. Pehk, K. Reivelt, M. Natali, J. Gurauskis, A. Lõhmus,U. Mäeorg, "Alkoxide-based precursors for direct drawing of metal oxide micro- and nanofibres", *Science and Technology of Advanced Materials*, 2011 **12**(3), 1–12.

II. T. Tätte, **M. Paalo**, V. Kisand, V. Reedo, A. Kartushinsky, K. Saal, U. Mäeorg, A. Lõhmus, I. Kink, "Pinching of alkoxide jets – a route for preparing nanometre level sharp oxide fibres", *Nanotechnology*, 2007, **18**(2), 125301.

III. **M. Paalo**, M. Hussainov, T. Tätte, I. Hussainova, "Rheological studies of carbon nanotube doped titanium-oxo-alkoxide materials and their use for fibers drawing", *Materials Science and Engineering: B*, (*submitted*) 2014.

IV. V. Kisand, J. Shulga, T. Tätte, U. Visk, M. Natali, G. Mistura, **M. Paalo**, M. Lobjakas, I. Kink, "Preparation of structured sol-gel films using tape casting method", *Materials Science and Engineering B-Solid State Materials for Advanced Technology*, 2007, **137**(1–3), 162–165.

V. V. Kiisk, T. Kangur, **M. Paalo**, T. Tätte, S. Lange, S. Pikker, I. Sildos, "Structural and luminescence characteristics of SnO_2:Eu and SnO_2:Eu,Sb nanophosphors upon annealing at high temperatures", *Materials Chemistry and Physics*, 2011, **130**(1–2), 293–298.

VI. **M. Paalo**, T. Tätte, M. Hussainov, K. Hanschmidt, M. Lobjakas, A. Lõhmus, U. Mäeorg, I. Kink, "Preparation and Characterization of CNT/TiO_2 Based Transparent Fiber Electrodes", *IOP Conf. Series: Materials Science and Engineering*, 2012, **38**, 012023.

VII. **M. Paalo**, T. Tätte, E. Shulga, M. Lobjakas, A. Floren, A. Lõhmus, U. Mäeorg, I. Kink,. "Preparation and Characterization of Transparent Electrodes Based on CNT-s Doped Metal Oxides", *Advanced Materials Research*, 2011, **324**, 133–136.

VIII. **M. Paalo**, T. Tätte, A. Juur, A. Lõhmus, U. Mäeorg, I. Kink, "Preparation of transparent electrodes based on CNT-s doped metal oxides", *In: Technical Proceedings of the 2008 NSTI Nanotechnology Conference and Trade Show: NSTI Nanotechnology Conference and Trade Show 2008; Boston, USA; June 1.–5. 2008*. Nano Science & Technology Institute, 2008, 389–391.

Other papers in related field not included in the thesis:

IX. P. Reemann, T. Kangur, M. Pook, **M. Paalo**, L. Nurmis, I. Kink, O. Porosaar, K. Kingo, E. Vasar, S. Kõks, V. Jaks, M. Järvekülg, "Fibroblast growth on micro- and nanopatterned surfaces prepared by a novel sol-gel phase separation method", *Journal of Materials Science: Materials in Medicine*, 2013, **24**, 783–792.

X. V. Kiisk, T. Kangur, **M. Paalo**, T. Tätte, S. Pikker, I. Sildos, "Optical characterization of sol-gel-derived SnO_2:Eu nanopowders annealed at high temperatures", *Physica Status Solidi (C)*, 2011, **8**(9), 2641–2644.

XI. M. Hussainov, T. Tätte, **M. Paalo**, J. Gurauskis, H. Mändar, A. Lõhmus, "Structure and Rheological Behavior of Alkoxide-Based Precursors for Drawing of Metal Oxide Micro- and Nanofibres", *Advanced Materials Research*, 2011. **214**, 354–358.

XII. T. Tätte, M. Hussainov, J. Gurauskis, H. Mändar, G. Kelp, R. Rand, **M. Paalo**, K. Hanschmid, I. Hussainova, "Alkoxide-based precursors for direct drawing of metal oxide micro- and nanofibres", *In: Technical Proceedings of the 2010 NSTI Nanotechnology Conference & Expo – Nanotech 2010. Vol.2: Nanotechnology 2010: Electronics, Devices, Fabrication, MEMS, Fluidics and Computational, Anaheim, CA, USA, June 21–25, 2010.* USA: Taylor & Francis, 2010, 245–248.

XIII. T. Tätte, R. Talviste, **M. Paalo**, A. Vorobjov, M. Part, V. Kiisk, K. Saal, A. Lõhmus, I. Kink, "Preparation and applications of transition metal oxide nanofibres and nanolines", *In: Technical Proceedings of the 2008 NSTI Nanotechnology Conference and Trade Show: NSTI Nanotechnology Conference and Trade Show 2008; Boston, USA; June 1.–5. 2008*, Taylor & Francis 2008, 109–111.

XIV. G. Kelp, T. Tätte, U. Mäeorg, S. Pikker, A. Tamm, **M. Paalo**, "The method of preparation of nanocolloidal SnO_2 water sol and its uses", Priority number: EE 2010-96; Priority date: 31.12.2010.

Author's contribution

Paper I: the author is responsible for SEM analysis, sample preparation and viscosity measurements, and actively participated in preparation of manuscript.

Paper II: the author is responsible for preparation of precursor materials, viscosity measurements, preparation of samples and microscopy analyses. The author actively participated in data analysis and in preparation of the manuscript.

Paper III: the author is responsible of precursor's preparation, fibers preparation, SEM-FIB analysis, development of electrical conductivity measurement set up and electrical conductivity measurements. The author is responsible for writing substantial part of the manuscript.

Paper IV: the author is responsible for preparation of precursor material and writing the experimental part of the manuscript.

Paper V: the author is responsible for preparation of precursor material.

Paper VI: the author is responsible for sample preparation, electrical measurements, SEM-FIB analysis and writing substantial part of the manuscript.

Paper VII: the author is responsible for CNT-composite fibers preparation, electrical measurements, SEM-FIB analysis and writing the manuscript.

Paper VIII: the author is responsible for sample preparation, electrical measurements, SEM-FIB analysis and writing the manuscript.

ABBREVIATIONS AND SYMBOLS

3D	three-dimensional
AFM	atomic force microscopy
AQ	aqueous
CMC	ceramic matrix composite
CNF	carbon nanofiber
CNT	carbon nanotube
CVD	catalytic chemical vapour deposition
DMSO	dimethyl sulfoxide
DWCNT	double-walled carbon nanotube
EBSD	electron backscatter diffraction spectroscopy
EDS	energy-dispersive X-ray spectroscopy
FIB	focused ion beam
FTIR	Fourier transform infrared spectroscopy
iPr	isopropyl group
L	ligand group
M	metal
M_2O_n	metal oxide
$M(OR)_n$	metal alkoxides
MTSAL	micelles templated by self-assembly of ligand
MWCNT	multi-walled carbon nanotube
NAQ	non-aqueous
Ph	phenyl group
Pr	propyl group
R	alkyl group
R	water to metal alkoxide ratio
RH	relative humidity
ROH	alcohol
SAXS	small-angle X-ray scattering spectroscopy
SDBS	sodium dodecylbenzene sulfonate
SDS	sodium dodecylsulfate
SEM	scanning electron microscopy
SWCNT	single-walled carbon nanotube
TEM	transmission electron microscopy
TEOS	tetraethyl orthosilicate
TMOS	tetramethyl orthosilicate
WDS	wavelength-dispersive X-ray spectroscopy
XRD	X-ray diffraction spectroscopy

PREFACE

In 21st century one class of the most beneficial materials is considered to be the composite materials – two or more known materials together can yield a material with new and extraordinary properties, capable of improving existing technologies or giving birth to new ones. Additionally, the ability to shape obtained materials into macroscopic and/or microscopic geometries is equally important for their successful utilization in practical applications.

Among others, ceramic materials are important for many advanced applications. Aside from being generally stable and hard materials, the most notable drawbacks of the ceramics are seen to be brittleness and small electrical and thermal conductivity. Aforementioned deficiencies can be eliminated by inserting reinforcing and/or conductive fillers into the ceramic matrix. Provided, that the filler is evenly distributed in the matrix and there is sufficient interaction between them, a reinforced ceramic matrix with improved toughness and electrical and/or thermal conductivity can be obtained. Compared with competing techniques, sol-gel method can provide a simple, inexpensive and novel way to obtain ceramics and ceramic composite structures with different geometries. Furthermore, as sol-gel processes are usually conducted in a liquid media at room temperature, addition of inorganic or organic fillers into resulting semicrystalline or crystalline ceramic material is relatively simple.

Discovery of carbon nanotubes (CNTs) in the early 1990s initiated general interest for nanotechnology and to the potential benefits from it. Because of their extraordinary properties CNTs have great potential as reinforcing elements, use in solar cells, as actuators, use in hydrogen storage, etc. Although CNTs have been used to reinforce lots of different matrixes from plastics to concrete, the problems with their purification procedures, dispersions and integrating them with the surrounding media have largely remained unsolved. Determination of processing parameters for different CNT-filled systems, promoting theoretical knowledge and understanding CNTs behavior in precursor and in the final material are essential for developing CNT-based composite materials.

The dissertation begins with a literature overview chapter that gives a brief summary of used methods, materials, experimental and theoretical aspects needed to comprehend the current thesis. The first of the four sub-chapters describes the structure of CNTs and their properties, and gives a brief overview about their synthesis, purification and dispersion methods. In describing CNTs the following works were used: [11], [21], [22], [35], [53], [54]. The second sub-chapter focuses at recent developments in metal alkoxide hydrolysis-condensation processes and formation of corresponding sols and gels. The following works were used: [69], [79], [80], [81], [86], [93]. The third sub-chapter gives a brief overview of rheology of sol-gel materials, and formations of powders, films, fibers and specialty shapes from metal alkoxide gels. The following references were used: [69], [93], [123], [127], [140]. The last sub-

chapter describes CNT-reinforced ceramic matrix composites, CNT percolation effects and influence of CNTs on rheological properties of materials. The following literature was used to prepare the last chapter: [150], [169], [174], [176], [180].

The aims of the thesis are formulated in the second chapter of the thesis.

The experimental chapter introduces conventional and novel methods, procedures and characterization techniques used in this study.

In the fourth chapter the preparation and characterization of metal alkoxide sols, their transition into differently shaped gels, and the role of external parameters affecting the shape formation processes are discussed in detail. Additionally, application of sol-gel method to obtain CNT-reinforced metal alkoxide sol precursors, their rheology, and CNT-reinforced metal oxide materials is also described.

In the final chapter all the results are summarized and the conclusions of the thesis are presented.

1. LITERATURE OVERVIEW

1.1. Carbon nanotubes

By the 19th century it became clear that carbon could exist in more than one form in nature – as graphite or as diamond. At the beginning of 20th century the discovery of X-ray diffraction enabled to describe the differences of the structures of diamond and graphite [1], and by the early 1980s the carbon science was considered unlikely to yield any major surprises [2]. This situation was changed in 1985 by Kroto *et al.* who managed to synthesize a big group of closed chained and spherical carbon compounds called fullerenes [3]. The most well known fullerene is formed from 60 carbon atoms and is called buckminsterfullerene (also marked C_{60}). This discovery, which brought Harry Kroto, Robert Curl and Richard Smalley a Nobel Prize in Chemistry, led to the further synthesis of fullerene-related carbon structures. As a by-product of fullerene synthesis in 1991, Iijima *et al.* found hollow tubular nanostructures now called multi-walled carbon nanotubes (MWCNT) [4]. Two years later, in 1993, single-walled carbon nanotubes (SWCNT) where synthesized and described simultaneously by two groups, Iijima *et al.* [5] and Bethune *et al.* [6]. A perfect single-walled carbon nanotube can be conceptualized as indefinitely long cylinder of one-atom-thick graphite (or graphene) layer. When the tube consists of several graphene cylinders nested inside another it is called MWCNT. Both ends of the carbon nanotubes can be capped by hemi-fullerenes or they can be open.

Long before Iijimas discoveries, there were several reports about different carbon nanofilaments and carbon crystals including the works of Radushkevich and Lukyanovich in 1952 [7], Hillert and Lange in 1958 [8], Oberlin, Endo and Koyama in 1976 [9], Abrahamson in 1979 [10] and Tennent in 1987. Unfortunately their works were not known to the broader scientific community nor were the hollow carbon structures such as carbon nanotubes, and therefore no significant impact was created. Iijima was the first to recognize the technological potential and possible applications of the carbon nanotubes. Furthermore, the report about CNTs by Iijima accelerated the pursuit of scientific community towards nanoscience and nanotechnology [11]. Good example for that is the growing list of different carbon nanostructures discovered and synthesized ever since. Coiled carbon nanotubes [12], SWCNT ropes [13], "peapods" [14], carbon nanofoam [15], CNT Y-junctions [16], "herringbone" and "bamboo" nanofibers [17, 18], nanobuds [19] and nanohoops [20] are just some of the new and interesting carbon materials available for material engineering in 21st century.

1.1.1. Structure and properties of CNTs

Physical and chemical properties of all carbon structures are directly related to the properties of a bonded carbon atom. The bonded carbon atom has six electrons from which two of them fill 1s atomic orbital and four fill 2s and 2p atomic orbitals. Because of the weaker bond strength and small energy difference between the valence electrons in the outer atomic orbitals (2s and 2p), the hybridization (mixing) is made possible and outer electrons can fulfill the sp^3 (diamond), sp^2 (graphite) (Figure 1) or sp (carbyne) hybrid orbital configurations. The sp-hybridization corresponds to a linear chain-like arrangement of atomic orbitals. Diamond's high hardness and density come from sp^3-type tetrahedral covalent bonding – each carbon atom is linked to four others at the corners of a tetrahedron via covalent bonding. Graphene, a one-atom thick layer of graphite, has sp^2–type bonding and each atom is joined to three neighbors in a trigonal planar arrangement to form sheets of hexagonal rings. This arrangement also makes graphene electrically conductive. In graphite, these single sheets are joined together only via van der Waals forces and as a result graphite is known to be soft material [21].
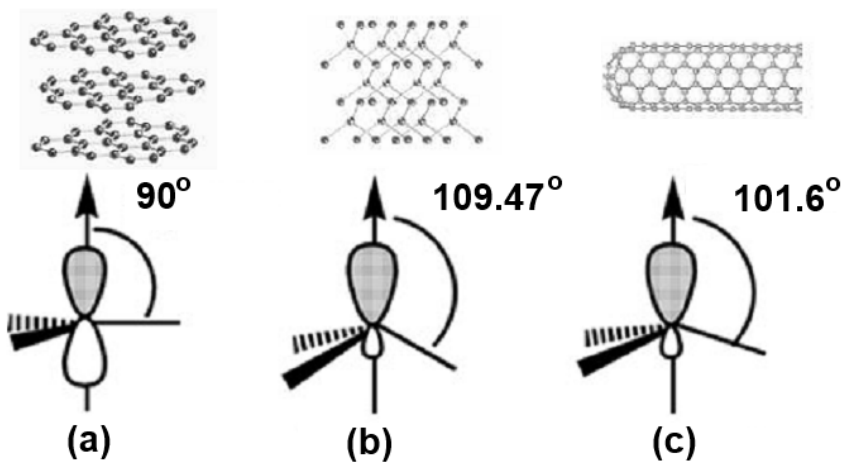
Figure 1. Hybrid orbital configurations of carbon atom in graphite (sp^2), diamond (sp^3) and nanotubes-fullerenes (rehybridized-sp^2). The angles shown in the figure are between the π orbital and σ bond. When a graphite sheet is rolled over to form a nanotube, the sp^2 hybrid orbital is deformed for rehybridization of sp^2 toward sp^3 orbital illustrated by the angle between the π orbital and σ bond. Rehybridization effect together with π electron confinement, give nanotubes unique, extraordinary electronic, mechanical, chemical, thermal, magnetic, and optical properties [22].

When the graphite sheet is rolled into a tube, the circular curvature will cause quantum confinement and σ-π rehybridization in which three σ bonds are slightly out of plane [22]. To compensate that, the π-orbitals are delocalized on the surface of the tube which makes carbon nanotubes electrically more conductive than graphite (Figure 1) [22]. Rehybridization also allows topological defects such as pentagons and heptagons to be incorporated into the hexagonal network to form capped, bent, toroidal, and helical nanotubes. As a result electrons will be localized in pentagons and heptagons because of redistribution of π electrons and nanotube overall electrical characteristics are disturbed. A nanotube is called defect free if it is of only hexagonal network and defective if it also contains topological defects such as pentagons and heptagons or other chemical and structural defects [22]. σ-π rehybridization also gives to the nanotubes the highest Young's modulus and tensile strength, and remarkable electronic response to strain, and metal-insulator transition. Nanotubes' high specific surface and σ-π rehybridization facilitate molecular adsorption, doping, and charge transfer on the nanotubes which, in turn, modulates electronic properties [22].

The hexagonal structured graphene sheet can be rolled into three different structures: zig-zag, armchair and chiral (Figure 2) [21]. The structure can be described by using a chiral vector (C_h) defined by the following equation:

$$\vec{C}_h = n\,\vec{a}_1 + m\,\vec{a}_2 \qquad (1)$$

In the formula (1) a_1 and a_2 are unit vectors in a two-dimensional hexagonal lattice, and n and m are integers. The structure of any nanotube can be expressed by the two integers n,m and/or chiral angle, θ. Armchair structure is produced when $n=m$ and $\theta=30°$ while zig-zag nanotubes are formed when m or $n=0$ and $\theta=0°$. Chiral nanotubes are formed for any other values of n and m, having θ between $0°$ and $30°$ [23]. Mathematical expression for carbon nanotube diameter is then defined [24] as follows

$$d = \frac{a\sqrt{m^2 + n^2 + nm}}{\pi} \qquad (2)$$

In formula (2) a is the lattice constant in the graphene sheet and $a = \sqrt{3}a_{C-C}$; a_{C-C} is the carbon-carbon distance (1,421 Å). The chiral angle, θ, is given by:

$$\tan\theta = \frac{\sqrt{3}m}{2n + m} \qquad (3)$$

SWCNTs unique electrical properties are also related to the tube structure and the rolling direction of the graphene layer. For a given (n,m) SWCNT, if $n=m$,

the CNT is metallic [25], and the rest of the SWCNTs can be either metallic or semiconducting depending on their chirality (or equivalently speaking, their diameter), as theoretically predicted [26–28] and experimentally confirmed [29, 30]. Although the structural chirality effects provide a richer range of physical phenomena as compared to the MWCNTs, it also significantly limits the range of applications. To date, there is not an easy procedure for routine synthesis of bulk quantities of SWCNTs with defined chirality [31].
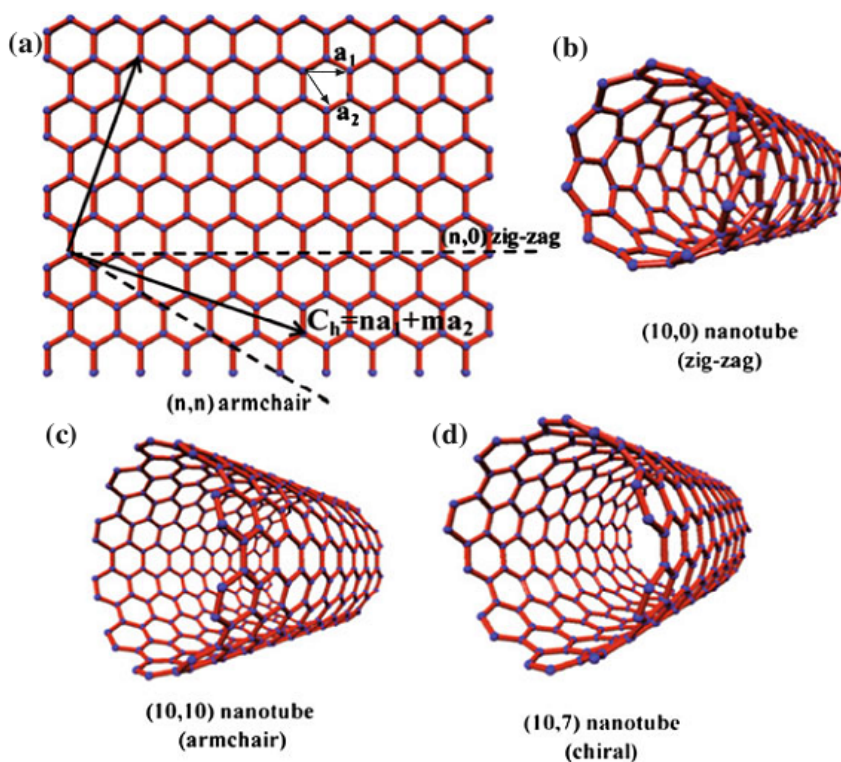

Figure 2. (a) An infinite graphite layer with (*n,m*) nanotube naming scheme describing how a nanotube is rolled up. a_1 and a_2 are the unit vectors of graphite layer in real space. (b) SWCNT of zig-zag structure, (c) SWCNT of armchair structure, and (d) SWCNT of chiral structure. From Rao *et al.* [31].

MWCNTs comprise of concentric tubes with an interlayer spacing of ~0.34 nm, approximate distance between graphene layers in graphite [32]. MWCNTs structures are described by two models – by "Parchment" model and by "Russian doll" model. According to the "Parchement" model a graphitic layer scrolls or rolls up to form concentric tubes. In the "Russian doll" model several graphene cylinders are nested inside another. The "Russian doll" structure of MWCNT is observed more often. Compared to SWCNTs, the physical properties of MWCNTs are typically worse. On the other hand, from the point

of view of possible applications, MWCNTs are more homogeneous in their physical properties as the large number of coaxial tubes smears out individual tube properties. Altogether, MWCNTs electrical properties can be similar to metallic SWCNTs [33], while growing metallic SWCNTs is very challenging because of the lack of control on SWCNT chirality [11]. This makes MWCNTs suitable candidates for applications where large amounts of CNTs with conducting properties are needed – for example, as conducting fillers in different composite materials.

Interesting members of the CNT family are double-walled carbon nanotubes (DWCNTs), as their morphology and most of their physical properties are very similar to SWCNTs but due to the additional graphene layer their electrical and chemical properties are significantly improved for many applications [32]. DWCNTs are especially important when functionalization is required to add new properties to the CNTs. In the case of SWCNTs, covalent functionalization will break some C=C bonds, leaving holes in the CNT structures and thus modifying both their mechanical and electrical properties. However, in the case of DWCNTs, only the outer walls are modified and therefore many properties are well preserved [11].

The lengths of the CNTs depend strongly from the synthesizing methods but usually can range from less than 100 nanometers to several millimeters. However, nanotubes up to several tens of centimeters can also be grown (e.g. [34]). SWCNTs diameters are typically 0.8–2 nm [35]. These characteristics make the SWCNTs exhibit very large aspect ratios. The strong van der Waals attractions that exist between the surfaces of CNTs cause them to assemble into "ropes" and bundles. SWCNTs are mostly known to exist as SWCNT "ropes" in bulk or in high concentration mediums. SWCNT ropes may have a diameter of 10–20 nm and a length of 100mm or above [21]. As MWCNTs consist of multiple graphene cylinders, the diameters of MWCNTs can exceed 100nm, but typically stay between 5 to 20 nm [35].

1.1.2. Synthesis, purification, and sorting of CNTs

CNTs are synthesized by three main methods and their variations and/or combinations: electric arc discharge [36], laser ablation [37], and catalytic chemical vapor deposition (CVD) methods [38]. DWCNTs and MWCNTs can be also grown by so called fullerene peapods method [39]. The distinct advantages of the laser ablation include ease of operation and production of high quality product, because it allows better control over processing parameters [21]. The electric arc discharge method benefits from the high temperature of the arc plasma as the grown carbon nanotubes exhibit a high degree of crystallinity [36]. Drawbacks of both methods are equipment requirements and the energy consumption which makes them less favorable for large scale production. Additionally, the electric arc discharge and laser ablation procedures are able to produce only powdered samples with tangled carbon

nanotube bundles [40]. For most of the practical applications CNTs bundles are highly undesirable and converting them into "single-tube state" can be time and energy consuming.

Aforementioned disadvantages are the reason why CVD is more often used for CNT synthesizing and has became a dominant mode of high-volume CNT production. CVD is a versatile and cost-effective technique for CNT synthesis because it enables the use of a feedstock of hydrocarbons in solid, liquid or gas phase and a variety of substrates (Figure 3), and permits the growth of nanotubes in the forms of powder, thin film or thick coating, randomly oriented or aligned tubes [21]. Generally SWCNTs are produced at higher temperatures (900–1200 °C) whereas MWCNTs are synthesized at lower temperatures (600–900 °C). However, MWCNTs prepared by CVD techniques contain more structural defects than those fabricated by the arc discharge. This implies that the structure of CVD-prepared MWCNTs is far from the ideal rolled-up hexagonal carbon ring lattice [21]. Large-scale CVD methods can also still yield contaminants that can influence CNT properties and often require thermal annealing and/or chemical treatment for their removal. These steps however can introduce defects in CNT sidewalls and shorten CNT length [21]. Because SWCNT synthesis by CVD requires much tighter process control than MWCNT synthesis bulk MWCNT prices are lower than for SWCNTs [35]. Use of MWCNTs is therefore favored for composite material applications.
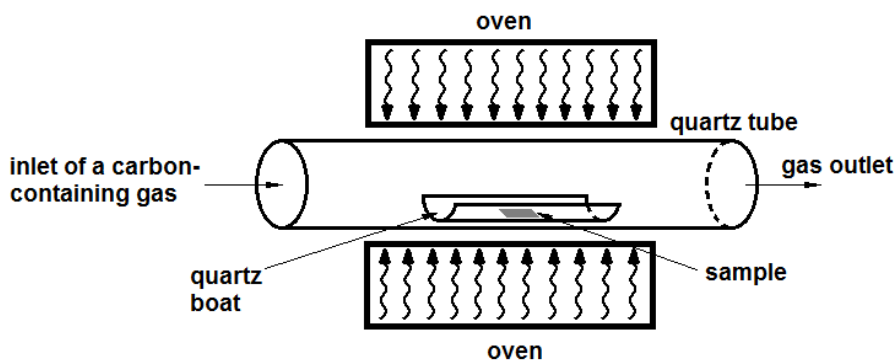

Figure 3. Schematics of a hot-wall thermal CVD experimental setup which has became one of the dominant mode of high-volume CNT production.

CVD also enables to grow nanotubes on surfaces as aligned and ordered nano-tube structures, as first demonstrated by Ren and coworkers by growing large-diameter MWNTs forming oriented "forests" on glass substrates by plasma-enhanced CVD [41]. CNTs can self-assemble into aligned structures during CVD growth to form vertically aligned films or patterns perpendicular to the substrate surface [40]. Those oriented CNT "forests" can be several hundred micrometers up to tens of millimeters high and can be manipulated into dense solids [42], aligned thin films [43], intricate three-dimensional (3D)

microarchitectures [44] and can be directly spun or drawn into long yarns and sheets [45, 46]. Additionally, CNT "forests" can be excellent source for the non-entangled and contaminant free carbon nanotubes.

As mentioned above, as-prepared CNTs can contain various impurities such as amorphous carbon, fullerenes, graphite particles and metal catalysts which can affect the performance of CNTs and their functional products significantly. Impurities can be removed using gas-phase oxidation [47], liquid-phase oxidation [48] and physical separation [49]. In the gas-phase oxidation procedure CNTs are oxidized in air, pure oxygen or chlorine atmosphere at 500 °C [47]. The liquid-phase oxidative treatment can be carried out simply by dipping nanotubes into strong acids such as concentrated HNO_3, H_2SO_4, mixed 3 : 1 solution of H_2SO_4 and HNO_3 or other strong oxidizing agents such as $KMnO_4$, $HClO_4$ and H_2O_2 [21]. Physical separation techniques are based on the initial suspension of CNTs in a surfactant solution followed by size separation using filtration, centrifugation or chromatography [21]. Although many CNT powders and suspensions are available commercially, the production of stable CNT suspensions requires chemical modification of the CNT surface or addition of the surfactants. Washing or thermal treatment is typically needed to remove surfactants after deposition of the solution, such as by spin-coating or printing [35].

Apart from high purity, length control is another important issue for successful application of CNTs in industry. Long entangled nanotubes tend to form large agglomerates, thus they must be dispersed or separated into shorter individual tubes prior to the incorporation into composites [21]. CNTs are inevitably shortened through gas-phase thermal oxidation and liquid-phase acid purification. Further mechanical cutting and dispersing procedures include ultrasonication, ball milling, and high speed shearing [50–52]. Wang *et al.* demonstrated that mechanical treatments can only break up the as-prepared agglomerates of nanotubes into smaller parts of single agglomerates while chemical treatment led to the dispersions with individual MWCNTs [51].

1.1.3. Solubility, dispersions, and functionalization of CNTs

Uniform and stable CNTs solutions are a prerequisite for many CNT-composite production procedures. Unfortunately pristine CNTs are rather non-soluble in most solvents due to the strong van der Waals forces between individual nanotubes causing CNTs to assemble into bundles. To successfully disperse CNTs, the dispersing medium should be capable of both wetting the hydrophobic tube surfaces and modifying the tube surfaces to decrease tube aggregation [53].

To characterize the degree of dispersibility, three CNT dispersion states are defined by Ham *et al.*: dispersed, swollen, and sedimented (Figure 4) [54]. In the dispersed state CNTs show no signs of aggregation and phase separation even for several months after dispersion by sonication, resulting in a stable

brown or black uniform suspension. Swollen describes the partial dispersion of CNTs, with aggregation, precipitation, and phase separation of the CNT solution. The separated dispersion typically has a hazy brown or black supernatant, with visible "fluffy" sediment of CNTs in the medium. In sedimented dispersions, CNT aggregates typically form sediment within minutes after sonication, have a low sedimentation volume, and a clear supernatant [53].
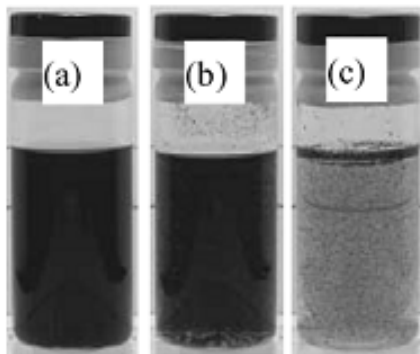

Figure 4. Nanotubes after sonication (a) in *N,N*-dimethylformamide, (b) in dimethyl sulfoxide, and (c) in water. (a), (b), (c) represent examples of "dispersed", "swollen" and "sedimented" solvents, respectively. From Ham *et al.* [54].

Carbon nanotube dispersions can be obtained by simply dispersing unmodified tubes in solvents or by chemically modifying them prior dispersion procedure. Chemical modifications of CNTs are achieved by noncovalent exohedral functionalization with surfactants, noncovalent exohedral functionalization with polymers or big molecules, defect-group functionalization or by covalent sidewall functionalization (Figure 5) [55].

The chemistry and mechanisms behind unmodified CNTs dispersions in solvents are not yet clear but some of the organic solvents that can be used to achieve carbon nanotube dispersions are *N,N*-dimethylformamide, *N*-methyl-2-pyrrolidone, chloroform, and dimethyl sulfoxide (DMSO) [53]. These suspensions retain dispersion for several days. Irrespective of the dispersion approach, the "dissolution" process is aided by prolonged sonication of the solution. It provides mechanical energy to overcome the inter-tube van der Waals forces in CNT bundles and contributes in exfoliation into smaller bundles, ropes and individual CNTs. Prolonged sonication cause cutting and breaking of the tubes, additionally improving the dispersion homogeneity of CNTs [56].
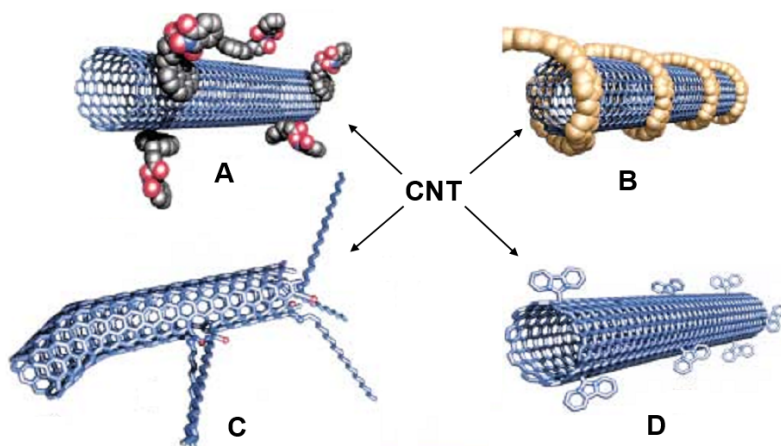
Figure 5. Functionalization possibilities for CNTs: A) noncovalent functionalization with surfactants, B) noncovalent functionalization with polymers or biomolecules, C) defect-group functionalization, and D) covalent sidewall functionalization. For methods A, B, D the tubes are drawn in idealized fashion, but defects are found in real situations. Based on the figure from Hirsch *et al.* [55].

Usually the surfactants are selected so that the hydrophilic regions of surfactants interact with polar solvent molecules, and the hydrophobic regions can adsorb onto nanotube surfaces [57]. Thus, the process of dispersing CNTs from aggregates, bundles, or ropes into separated individual CNTs depends strongly on the length of the hydrophobic regions and the types of hydrophilic groups of the surfactant [58]. Most widely used surfactants include sodium dodecylsulfate (SDS), Triton® X surfactants (e.g. polyethylene glycol p-(1,1,3,3-tetra-methylbutyl)-phenyl ether), sodium dodecylbenzene sulfonate (SDBS) and numerous ionic liquids.

Because small molecules or polymers can adsorb onto CNT surfaces by π–π interactions, polymers and biopolymers have also been used to modify CNT surfaces. Strong π–π interaction between CNTs and used polymers drives the wrapping of the polymer around a CNT (see Figure 5). The inter-tube van der Waals interactions are weakened and increase the dispersibility of CNTs while the sp^2-conjugated structure and the electronic performance of CNTs are preserved. Surfactants, polymers and biopolymers in general can be useful for dispersing CNTs but the current limitations of surfactant-based solubilization are the relatively low levels of solubility and that the surfactant often remains as an impurity in downstream processes [53].

Van der Waals forces between individual tubes or bundles can also be eliminated by introducing polar functional groups on the walls and/or defect sites of nanotubes. The most common functionalization occurs already during the purification or separation of CNTs with strong acids [21]. Depending on the reaction conditions, defects and opening of nanotube tips are introduced, followed by the formation of carbonyl and carboxyl functional groups on these

sites [58]. The formation of such functional groups is detrimental to the physical properties of CNTs. However, it is widely used to fully introduce CNTs into matrices that otherwise react very little with the nanotubes. After initial carboxylation, the carboxylated intermediates can subsequently derivatized with different types of molecules to further increase CNTs interfacial interaction with the surrounding media. Alternatively, CNT sidewalls can be directly functionalized by addition reactions or by fluorination, for example [58]. Chemical compounds are then bonded directly with CNT wall electrophilic π-system without introducing any defect sites. Covalent sidewall functionalization is expected to produce the most stable dispersion, because the dispersion becomes a function of the bound functional groups and the density of the bound groups [53].

1.2. Sol-gel technology

In his famous works the promoter of modern colloid science Wolfgang Ostwald, a son of a graduate of University of Tartu and Nobel Prize winner Wilhelm Ostwald, proposed classifications of colloidal dispersions based on three states of matter – gas, liquid and solid [59]. "Combining" states of matters results in eight groups of colloidal dispersions including one with small solid particles suspended in a liquid medium – henceforward referred as a "sol". Under appropriate conditions, certain sol particles are able to form non-fluidal networks that are expanded throughout their whole volume by a fluid [60] – "sol" is transformed into a "gel". Above defined material stages, "sol" and "gel", and the ability to shift equilibrium between these two stages is the very basis of "sol-gel" technology.

The phenomena where metal-oxo-organic nanocolloidal particles at relatively low temperatures form 3D-networks in liquid (sol) up to the point where the network connects all the particles throughout the liquid medium (gel) was first scientifically described by Ebelman in 1846 [61]. Although the term "sol-gel" was not used in his study on formation of silicate glasses, it can be considered as the very first sol-gel related publication. Almost a century later, in 1931, one of the first practically applicable sol-gel products was invented when Kistler desiccated waterglass-silica gels and as a result obtained the first aerogels [62]. The earliest sol-gel works already researched also the possibility to modify surfaces of different solid substrates with oxide layers [63], an application heavily exploited by modern industry. Nevertheless, it seems that the investigations in sol-gel technology were generally episodic until early 1970s when the studies of Dislich [64, 65] with borosilicate glass successfully aroused great interest among scientific community.

Before further approach to the topic it should be made clear that while the term "sol-gel process" marks transition from sols to gels, the term "sol-gel technology" is used to describe a cascade of technological steps with a final

purpose to obtain solid polycrystalline oxide structured materials (bulks, films, powders, fibers, etc.). This cascade of processes is named by its most crucial step – materials transformation from sol to gel – and thus, the papers published under the topic discuss broad range of aspects, from preparation and structure of neat chemicals to sintering and applications of resulting materials.

Structured ceramic/glass materials with diverse functionalities can be easily obtained *via* sol-gel technologies for several reasons. Firstly, as the sol-gel transition is conducted in liquids, the resulting ceramic/glass materials homogeneity, possibility of doping and composition controlling is much better than competing methods like grinding, hot pressing and sintering of ceramics directly from metal oxides (e.g. [66]). Secondly, the encapsulation of organic specimens [67] or use of organic additives in oxides is possible only by sol-gel technology due to its mild synthesis conditions. It is even possible to safely trap living cells and bacteria using sol-gel technology so that they retain their bioactivity protected by the oxide cage [68]. Thirdly, the gel phase of the process enables to shape self-standing structures in macro-, micro- and nanoscale as described in the following chapters (see chapter 4.4.). The list of structures with different geometries varies from simple monoliths to spheres, fibers, tubes, hollow spheres, needles, structured films etc. Finally, when compared with other procedures, the lower cost of the technology and the possibility to use it for coating complicated and/or large surfaces cannot be underestimated either [69]. For example, sol-gel preparation of TiO_2/Pd coated architectural glass for sun reflecting windows [70] is not limited by a vacuum chamber, needed to deposit films by vapor deposition or sputtering.

The flexibility and simplicity of the sol-gel technology have made it one of the leading procedures to design and prepare novel composite materials with diverse composition, structures, functionality and morphology. Large variation of micro- and nanostructures including porous (aerogel, xerogel), dense (glasses, ceramics), organic-inorganic hybrids, multi-layer structures and nano-composites can be fabricated using sol-gel method. Comprehensive review articles and books have emerged in recent years, e.g. [69, 71, 105], from where one can observe the multiplicity and potential of the modern sol-gel technology for producing wide variety of materials for photonic-, electronic-, mechanical-, chemical-, biological- and biomedical applications.

According to market analysis published by the American Ceramic Society, the global market of sol-gel derived products was worth $1.4 billion in 2011 and will grow up to $2.2 billion by 2017 (a compound annual growth rate of 7.9 percent) [72]. Among the companies developing, supplying and/or utilizing sol-gel based products are for example 3M Co. [73] and Boeing [74]. Products based on sol-gel technology for example include corrosion protective coatings on metals [75], superhydrophobic and superhydrophilic coatings on glass [75], thermal insulators [76], specialty ceramics, antireflective coatings on glass lenses [75], fiber optic sensors [77], aerogels [78] and etc. just to name a few.

Simultaneously with impressive technological achievements, fundamental understanding of precursor material properties, sol-gel processes and post processing steps also evolves. Fine example is the idea that hydrolysis-condensation processes of silicon alkoxides and metal alkoxides are conceptually different [79]. Based on the numerous experimental observations on metal alkoxides structures, hydrolysis-condensation processes and formation of sol particles, V. Kessler *et al.* have proposed a new model for the metal alkoxide hydrolysis processes and formation of the resulting particles [79–83]. Experimental and theoretical works by the research groups of U. Shubert *et al.* [84] and M. Nygren *et al.* [85] have also contributed to the deeper understanding of metal alkoxide sol-gel processing.
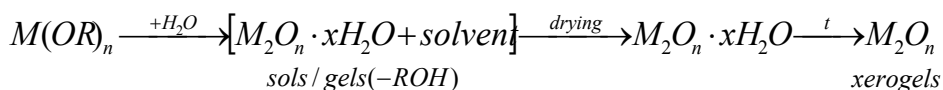
As a result, acquired knowledge from direct and indirect measuring and observation methods allows synthesis of new materials and structures and opens up new synthesizing routes for existing materials. For example, monitoring rheological parameters of the sol-gel transition allows determination of the gel materials processing parameters and to understand gel materials dynamics and microstructure [69].

1.2.1. Metal alkoxides

Although different classes of chemical compounds are used as neat materials in preparation of precursors for sol-gel processing, alkoxides or modified alkoxides (with partial substitution of alkoxide groups by other organic ligands) are by far the ones used most frequently [86]. Historically, and even today, most extensively researched and industrially employed alkoxide have been different silicon alkoxides like for example tetraethyl orthosilicate (TEOS) and tetramethyl orthosilicate (TMOS). The fact that metal alkoxides and silicon alkoxides have very similar physical characteristics (like high boiling point, viscosity etc.), gave a lot of researches expression that both alkoxide groups chemical properties are generally similar with the only exception that metal alkoxides are many orders of magnitude more reactive. Because of aforementioned reasons, for a long time the hydrolysis-condensation mechanism of silicon alkoxides has also been used to describe corresponding processes in main group and transition metal alkoxides [87, 88]. Presumption that metal center in alkoxides behave in the same way as silicon, which is metalloid and its chemical-physical properties resemble more carbon than metals, is not correct in many ways as recently demonstrated [80, 84]. Furthermore, the colloidal particles formed as a result of hydrolysis-condensation reactions of metal alkoxides have different structure and chemical-physical properties from their silicon alkoxides counterparts [79].

Metal alkoxides ($M(OR)_n$) are derivatives of alcohols (ROH), where R stands for an alkyl group (C_xH_{2x+1}). RO- can be easily removed via hydrolysis and thermal treatment, resulting in high purity unhydrated oxides and corresponding

alcohol [89]. The overall process of formation of oxide from metal alkoxide can be presented by the following scheme:

$$M(OR)_n \xrightarrow{\ +H_2O\ } \underset{sols/gels(-ROH)}{\left[M_2O_n \cdot xH_2O + solvent\right]} \xrightarrow{\ drying\ } M_2O_n \cdot xH_2O \xrightarrow{\ t\ } \underset{xerogels}{M_2O_n}$$

In practice, the process starts from the metal alkoxide solution – containing alcohol as solvent, water as hydrolysing agent and an acid or base as catalyst. Alkoxides undergo hydrolysis and condensation processes at room temperature, giving rise to a sol, where fine oxide nanoparticles are dispersed. Further reactions lead to the formation of homogeneous solid network of oxide particles throughout the liquid, eventually solidifying sol into wet gel. Removing excessive water and solvents enables to obtain dry gels, also called xerogels [69].

From the practical point of view, the main advantages for using alkoxides in preparation of oxide materials by sol-gel method are presented in comprehensive review book "The Chemistry of Metal Alkoxides" by N. Y. Turova *et al* [86]:

- majority of the $M(OR)_n$ derivatives (with n≤3) can easily be subjected to deep purification by distillation or sublimation (below 200 °C) or by recrystallization from organic solvents;
- metal alkoxides easily undergo hydrolysis, forming hydrated oxides not containing any extra anions, in contrast to precipitation from the aqueous solutions of inorganic salts;
- forms of $M_2O_n \cdot xH_2O$ are the least agglomerated and maximally hydrated (their structures do contain the minimal amounts M–O–M bridges), and therefore they easily form stable colloid systems – sols and gels – and have high reactivity;
- dehydration of sols/gels occurs at rather low temperatures, sometimes directly during the hydrolysis, and is accompanied by the formation of very small oxide particles with well-developed surfaces, high chemical activity, and often amorphous or metastable phases that on subsequent thermal treatment are transformed into more stable forms.
- from the applications point of view, metal alkoxides are pure, inexpensive and easily accessible while providing synthesis of highly homogeneous oxide gels, films, coatings, glasses, fibers, and so on.

From the perspective of theoretical analysis, because of the domination of electrostatic interaction between alkoxide ligand (-OR) and metal cation, metal alkoxides ($M(OR)_n$) can be described as salts – more precisely salts of alcohols. Alcohol anions behave as strong Brønsted bases and contribute to metal alkoxides ability to react immediately with acidic ligands [90]. At the same time, extreme Lewis basicity of the alkoxide anions RO- causes metal alkoxides

oligomerizaton. Metal alkoxides ability to form aggregates using ligands for bridging, rather than exist as monomers like silicon alkoxides, was already reported by Bradly *et al.* in the early 1960s [91]. Particles size and agglomeration are responsible for more general physical properties, like viscosity changes for example [91]. Metal alkoxides ability to form solvates, important property also for practical applications, is only possible if the solvating ligand can form a hydrogen bond to an alkoxide ligand, i.e. act as a Brønsted acid [80].

1.2.2. Hydrolysis and condensation of metal alkoxide

The sol-gel process involving silicon alkoxide, include two steps – the hydrolysis of the alkoxide and its polycondensation [92]. Common silicon alkoxides, are not very reactive in water derived hydrolysis processes, thus the process usually requires acid or base catalysis [80]. Excellent review can be found in [93]. The hydrolysis of a silicon alkoxide by base-catalyzed S_N2 or by acid catalyzed S_N1 nucleophilic substitution mechanism leads to the formation of a reactive Si-OH group. Initial hydrolysis products can react further either *via* another hydrolysis reaction or a condensation reaction. Acidic catalysis leads to a much quicker hydrolysis than basic catalysis resulting in different final structures for the gel networks [92].

The major difference in reactivity of metal alkoxides from those of silicon lies in their very facile and rapid reaction with water in the absence of catalysts [80]. For example, the reaction times for hydrolysis of zirconium alkoxides are 10^5–10^8 times faster than that for silicon alkoxides [94, 95]. As seen from the Figure 6, metal alkoxide ligand exchange reaction, i.e. both hydrolysis and chemical modification, is known as proton-assisted S_N1-type transformation where ligand protonation is followed by speed-limiting cation formation step and addition of the corresponding base of the new ligand with elimination of alcohol [96]. The reaction speed is determined by the acidity of HZ reactant and the nucleophilic properties of the entering ligand Z- have no influence on the ligand exchange process [97]. Earlier proposition that metal alkoxides higher reactivity was due the S_N2 reaction mechanism [88] has been rejected by theoretical calculation. Calculated ligand exchange energies for S_N2 mechanism is about 600 kJ/mol, which is 20 times higher than is measured experimentally [98].
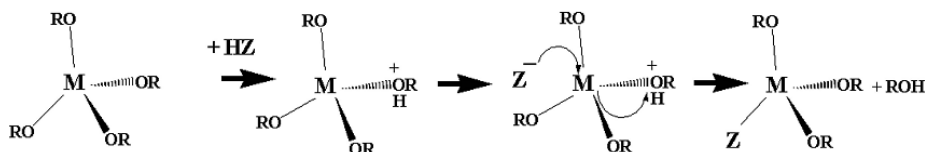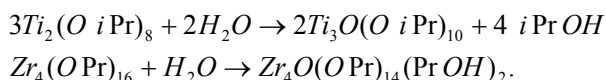

Figure 6. Proton-assisted S_N1-type mechanism for ligand exchange in metal alkoxides. From Kessler *et al.* [80].

After the first hydrolysis cycle, the partially hydrolyzed molecule can be hydrolyzed further or it can be subjected to condensation processes. In the instance of silicon-based compounds the condensation/polycondensation reactions are kinetically independent from the hydrolysis reaction and, according to a literature, can follow three competitive pathways – oxolation, alkoxolation and olation e.g., [99, 93]. The structure and rheology of the forming colloidal medium is greatly dependent upon the preparation condition. Partially hydrolyzed silicon alkoxide species, undergoing base catalyzed S_N2-type process, are more prone for further hydrolysis than condensation processes and thus cause initially formed monomeric particles to form cross-linked aggregates with micellar type rheology. The acid catalyzed nucleophilic substitution reaction (proton-assisted S_N1 mechanism) intermediate species acidic dissociation is hindered by the low pH of the solution. This makes further condensation processes possible, which results in colloids containing less cross-linked long chain polymeric molecules [100]

Unlike from silicon precursors, metal alkoxides low activation energies of ligand exchange and simple rearrangement of the metal-oxygen cores convert the microhydrolysis (addition of small amounts of water) and condensation into single process that leads to oxoalkoxide products [82, 85]. Good examples are homometallic titanium and zirconium alkoxides which microhydrolysis results in well-defined oligonuclear oxo-alkoxide species through one-step hydrolysis-condensation transformation associated with profound restructuring of the precursor molecules [98, 83]:

$$3Ti_2(O\,i\Pr)_8 + 2H_2O \rightarrow 2Ti_3O(O\,i\Pr)_{10} + 4\,i\Pr OH$$
$$Zr_4(O\Pr)_{16} + H_2O \rightarrow Zr_4O(O\Pr)_{14}(\Pr OH)_2.$$

The modification of metal alkoxides with chelating ligands has demonstrated that the size and shape of the primary particles formed in sol-gel treatment of metal alkoxides are defined not by kinetic factors in their hydrolysis and polycondensation but by the interactions on the phase boundary, which is in its turn directed by the ligand properties [80]. Metal alkoxide microhydrolysis products are also known to have extremely complicated structures (Figure 7).

Nevertheless, the main parameter that affects the course of hydrolysis reaction and permits to achieve the formation of a distinct structure is the molar ratio of reactants (i.e., the water to metal alkoxide ratio $R=[H_2O]/M(OR)_n]$) [86]. Alternatively, the hydrolysis ratio, defined as mole ratio of water to alkoxy groups, is also used in sol-gel processing of metal alkoxides [60]. Structures formation is determined by dense packing of metal cations and oxygen atoms of the ligands and is a result of coordination equilibrium [81].
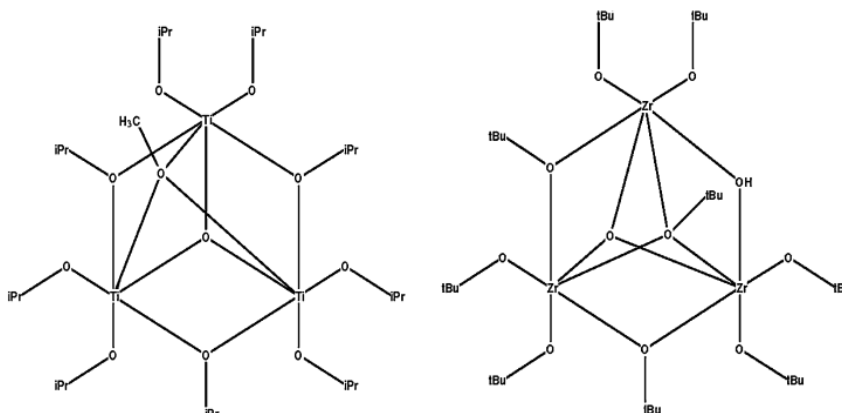
Figure 7. Molecular structures of the microhydrolysis products of titanium [101] and zirconium alkoxides [102].

In addition to aqueous hydrolysis method, a non-aqueous process has also been applied for growing metal oxide nanoparticles [103, 104]. Whereas the hydrolysis with water is a conventional chemical process and the basis of the sol-gel technology [69, 71, 105], the non-aqueous thermal process has been almost forgotten since some early works [106–108]. At relatively low condensation temperatures, alkoxides decomposition reaction gives ethers as the major products:

$$M - OR + RO - M \rightarrow M - O - M + R_2O$$
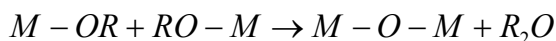
The formation of oxo bridges is analogous to ageing of oxide hydrates accompanied by condensation of two hydroxy groups with elimination of a water molecule [103]. Similarly to the aqueous hydrolysis method, thermal condensation of metal alkoxides results in metal-oxo-alkoxides – small, (partially) crystalline, nanometre-sized oxide nanoparticles stabilized by a shell of alkoxy groups.

1.2.3. Formation of sols from metal alkoxides

Kessler *et al.* concludes from their researches with heteroligand molecules that the sol-gel transition of metal oxide colloids produced from metal alkoxides is only possible trough tremendously quick hydrolysis-condensation reaction which leads to the equilibrium molecular oxoalkoxide products with structures derived from dense packing of cations and anions (Figure 8) [81]. When the formed hydrolysis-condensation products grow too big, they will lose coordination equilibria and become heterogeneous particles stabilized by residual organic ligands on the surface which determine their interaction with surrounding media.

Physical evidences of aforementioned particles from different metal alkoxides have been presented by numerous research groups [109–112]. Kessler *et al.* have denoted these primary particles as Micelles Templated by Self-Assembly of Ligand (MTSALs) [79–81]. MTSALs size depends on the condition of coordination equilibrium and ligand-solvent interactions and varies between 2–5 nm (Figure 8) [81]. Aggregates in this size which are related to coordination equilibrium are common in inorganic chemistry and incorporate usually dozens of metal atoms, as $Au_{39}(PPh_3)_{14}Cl_8$ for example [113]. According to Kessler *et al.* hypothesis, the particle size is limited by several factors – solubility of the forming oxides and the diffusion coefficients of the multivalent cations in organic media, activation energies for incorporating of an additional cation on the surface of an already formed particle [81]. The heterogeneous growth kinetics can become hindered when the aggregate obtain certain limiting size, as theoretical calculations show that activation energies for particle growth increase when the surface curvature is decreasing and the particle diameter is increasing [114, 115].
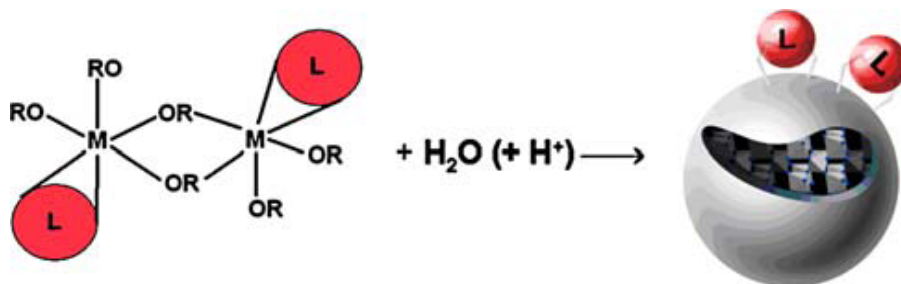

Figure 8. Formation of primary product of the sol-gel process. Kessler *et al.* has denoted these as MTSAL particles. L marks the ligand group. From Kessler *et al.* [81].

About 5 nm size oxide or sulfide particles, analogous to MTSALs, have been also reported to form in the non-hydrolytic sol-gel procedures [116, 117]. The main difference with the particles formed on hydrolytic processes, is the avoidance of dehydration process which allows obtaining fully crystallized primary particles.

1.2.4. Gel formation

Successive processing of the initial hydrolysis products will determine their further characteristics. Fully crystalline particles result from hydrothermal treatment while without thermal treatment high reactivity of the amorphous shells causes the particles to interact with each other. Particles interaction is possible via hydrogen bonding or via coalescence with formation of M-O-M bridges. Aggregation of the initial particles has two pathways as seen in Figure 9.
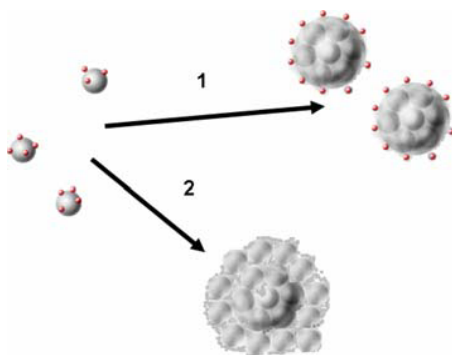
Figure 9. Aggregation of sol particles in case of low hydrolysis ratio and essential amount of ligands interacting with the solvent (1) results in uniform transparent sols and gels. Higher hydrolysis ratio in the absence of necessary ligands (2) forms dense and non-uniform aggregated gels or precipitates. From Kessler *et al*. [81].

In the case of low hydrolysis ratio and/or the presence of chelating ligands that strongly interact with the solvent (pathway 1 in Figure 9), aggregates with common surface and strong interaction with the solvent are formed [94, 118]. Further aging or hydrothermal processes will lead to coarsening and aggregation of particles [119]. When higher hydrolysis ratios are achieved and no heteroligands are used, the initial particles will form dense gels or precipitates by aggregating trough the volume of solvent (second pathway in Figure 9) [81]. T. Sugimoto *et al*. has demonstrated that the formation of primary particles is completed within a period less than 2 s and that the size of the primary particles remains practically unchanged in systems rich of organic solvent, and the gelation is a result of their aggregation [120]. Raveendran *et al*. has published series of TEM images of TiO_2 nanoparticles formed in accordance to the concept described above (Figure 10) [121].
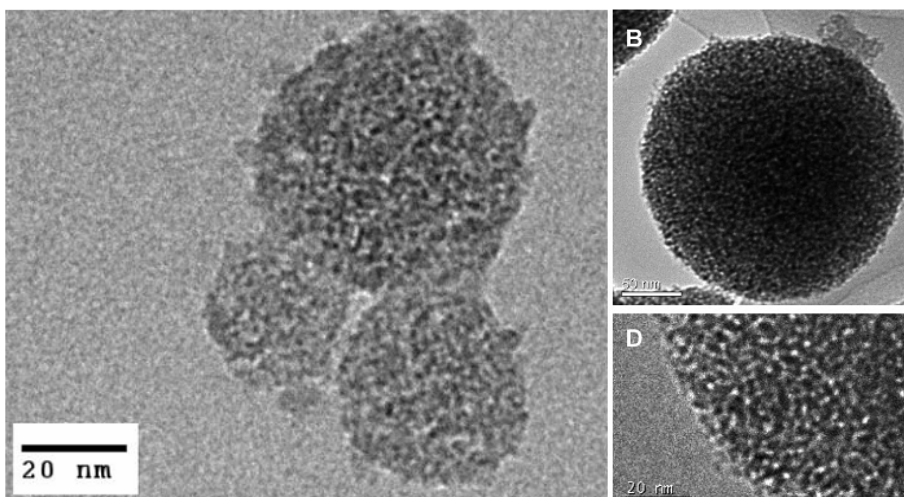

Figure 10. TEM view of hierarchical aggregates produced from TiO_2 nanoparticles. Image on the left is from Kessler *et al.* [109] and images on the right are from Raveendran *et al.* [121].

Simplified explanation of gelation is that clusters of particles grow by aggregation until the clusters collide and link to produce a single giant cluster that is called a gel. Before so called "gel point", many clusters are present in the sol phase, entangled in but not attached to the spanning cluster. With time, bigger clusters progressively become connected to the network and the stiffness of the gel increases. At the gel point, two last big clusters link together and continuous solid network is formed [93]. As a result, material viscosity abruptly rises and elastic response to stress appears (Figure 11) [122]. The interactions that provoked gelation continue long beyond the gel point, permitting flow and producing gradual changes in the structure and properties of the gel. The gel structure depends on the size and distribution of the particles and the strength of the attractive forces between them [93].
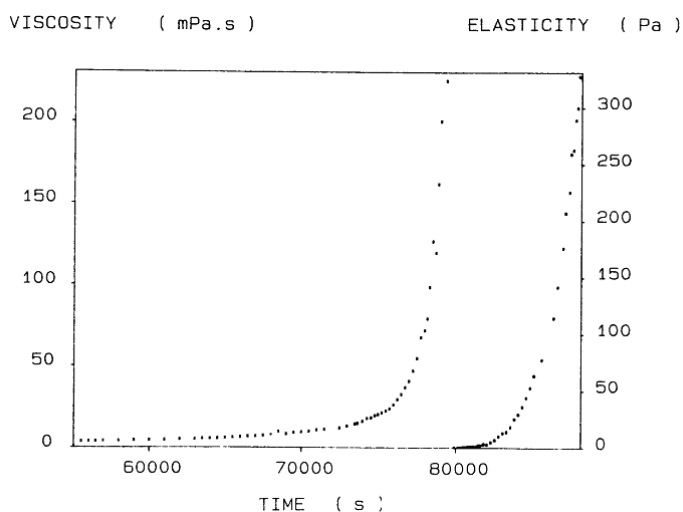
Figure 11. Evolution of viscosity (left curve) and elasticity (right curve) in time for silica gel synthesized from TMOS. From Gauthier-Manuel *et al.* [122].

1.3. Rheology and shaping of viscous metal alkoxide sols

1.3.1. Brief introduction to rheology

As the reaction proceeds during sol to gel conversion, the viscosity of the solution gradually increases until the solution is transformed to a gel. For this reason, the measurements of viscous or viscoelastic behavior of the samples are expected to give important information on the degree of polymerization-condensation reaction and on the size and shape of the formed particles. The rheological behavior of a real material is expressed by a combination of elastic deformation, viscous flow and plastic flow [69].

31

When a stress is applied to an elastic body, the corresponding strain occurs instantaneously. Upon removal of the stress, the strain instantaneously disappears – the stress is proportional to the strain. When a solid is deformed by a shear stress σ the following formula holds:

$$\frac{\sigma}{\gamma} = G \tag{4}$$

Here γ is the shear strain and G is a constant called shear modulus [69].

In simple shear (Figure 12), the response of a viscous fluid is characterized by a linear relationship between the applied shear stress and the rate of shear [123]:

$$\sigma = \frac{F}{A} = \eta\dot{\gamma} \tag{5}$$

Here, η is a constant called viscosity and $\dot{\gamma}$ is a shear rate. Liquids for which η is a constant, regardless of the values of σ and $\dot{\gamma}$ are called Newtonian liquids and such a flow is called Newtonian flow. Shear strain caused by the viscous flow is not recovered even if the stress is removed. The strain varies as a function of time [69].
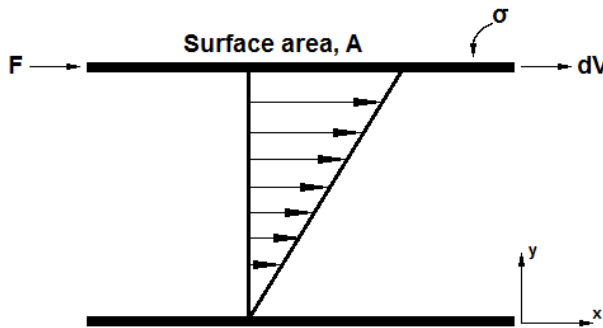
Figure 12. Schematic representation of a unidirectional shearing flow where *F*=force, *A*=area, *dV*=velocity, *σ*=shear stress.

In shear thinning and shear thickening flows (Figure 13), the viscosity of the liquid as expressed by equation (Equation 5) is not constant. Therefore, these liquids are considered as non-Newtonian liquids. The viscosity, defined as the ratio of shear stress to shear rate, is called the apparent viscosity, η_α, and it changes with $\dot{\gamma}$ as shown in Figure 13 [69].

Figure 13. Qualitative flow curves of Newtonian, pseudoplastic (shear thinning), dilatant (shear thickening), viscoplastic and Bingham plastic liquids. From Deshpande *et al.* [123].

Substances having a threshold stress (called yield stress or apparent yield stress, σ_y), which must be exceeded for the fluid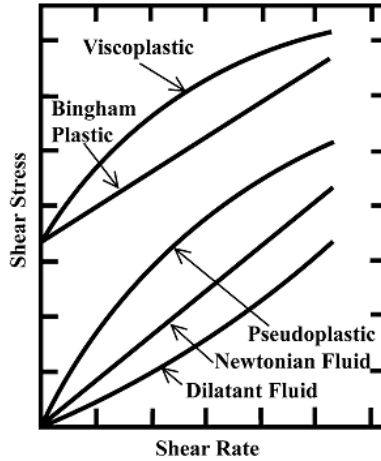 to deform (shear) or flow, behave like an elastic solid when the externally applied stress is less than the yield stress, σ_y. Once the magnitude of the external yield stress exceeds the value of σ_y, the fluid may exhibit Newtonian behaviour (Bingham plastic) or shear thinning characteristics (viscoplastic) [123].

Flow behavior that is different from viscous flow (Newtonian flow) is called non-Newtonian in the broad sense. Many real liquids exhibit flow behavior possessing both viscous and elastic nature, that is, viscoelastic flow or deformation. From the experimental observation it has been noted that a material tends to show elastic behavior at low temperatures or for a short time stress application while viscous behavior is observed at high temperatures or for a long duration of applied stress. Additionally, viscoelastic behavior is inherent for solution containing low molecular weight polymers or fine particles at low concentrations and for solutions and melts consisting of high molecular weight polymers or large particles. The viscous and viscoelastic properties of sol-gel solutions are characterized by measuring viscosity under different conditions. Following viscometers are mostly employed – rotating cylinder viscometer, cone and plate viscometer, capillary viscometer, falling sphere viscometer and pulling-up-sphere viscometer [69].

The viscosity plotted as a function of time (see Figure 11) provides qualitative information on the growth of particles and formation of cross-linking between the particles. In order to relate the shape of particles to the flow behavior of the sol, determination of the reduced viscosity, η_{sp}/C and the intrinsic viscosity, is needed [124–126]. The specific viscosity, is defined as

$$\eta_{sp} = \frac{(\eta - \eta_0)}{\eta_0} \qquad (6)$$

where η is the viscosity of the solution and η_0 is that of the solvent. The reduced viscosity is calculated by dividing η_{sp} by the concentration of particles, C, of the sol

$$\eta_{sp}/C = \frac{\eta - \eta_0}{\eta_0} \frac{1}{C} \qquad (7)$$

The reduced viscosity represents the increase in viscosity assigned to a single particle. The intrinsic viscosity *[η]* can be obtained by extrapolating the η_{sp}/C vs. *C* curve to *C*=0. The intrinsic viscosity represents the increase in viscosity attributed to one particle in the solution of very low concentrations [69].

The extensional rheology is used to understand the materials processing behaviours, for example, in fiber spinning, inkjet printing, or curtain coating. Elongational flow occurs when a force acts perpendicular to an area with a finite cross section (Figure 14). Because the volume of an incompressible fluid must remain constant, elongation is accompanied by a simultaneous transverse contraction. Hence during steady elongational flow, an infinitively small volume of fluid with an initial cross-section A_0 accelerates in the direction of flow under the action of the elongating force. In the steady state, the outflow is continuously replaced by inflow through the area A_0. Analogous terms with shear flow can be defined also for elongational flow [127]:

$$\sigma = \frac{F}{A} = \eta_E \dot{\varepsilon} \qquad (8)$$

Here $\dot{\varepsilon}$ is elongation rate and η_E is called elongational viscosity (also extensional or Trouton viscosity).

From his experiments on elongating liquid fibers or filaments, Trouton revealed that for an incompressible Newtonian material the elongational and shear viscosities are related as follows: $\eta_E = 3\eta$ [128]. For the non-Newtonian liquids, except in the limits of $\dot{\gamma} \rightarrow 0$ and $\dot{\varepsilon} \rightarrow 0$, there does not appear to be any simple way enabling the prediction of η_E from a knowledge of η (or vice versa), and the determination of η_E rests entirely on experiments [123].

One distinct feature of viscoelastic fluids is the so-called memory effect. For instance, viscous fluids have no memory whereas an ideal elastic solid has a perfect memory as long as the stress is within the linear limit. Thus, viscoelastic fluids are characterized by using a relaxation time, or a spectrum of relaxation times, which is roughly a measure of the span of their memory [123].
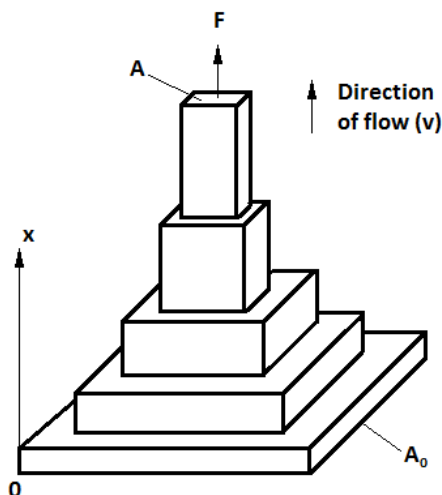
Figure 14. Schematics of monoaxial steady-state elongational flow. *F*=force; *A*=area, *x*=coordinate axis; *v*=velocity.

1.3.2. Rheology and spinnability of alkoxide sols

Firstly, it should be noted that qualitative rheological investigations have been mostly performed on numerous Si-alkoxide systems. Those few publications describing metal alkoxides flow behavior, are presuming that metal alkoxide sols inner structure is similar to silicon alkoxide sols [93]. As discussed thoroughly in chapter 1.2, the latter assumption is not always valid.

Flow behavior of a material can be found by measuring its viscosity as a function of shear rate, using the rotating viscometer or the cone and plate viscometer. In this case, the measured viscosity is the apparent viscosity. However, the word viscosity and the symbol η are used for simplicity [69].

Sakka and coworkers [129–132] and Kamiya *et al.* [133] investigated the rheology of siloxane systems prepared from TEOS. Evaluating concentration dependence of the reduced viscosity, η_{sp}/C, it was demonstrated that usually silica sols behave as Newtonian liquids when the viscosity is low due to low concentration of particles, small particle size and/or separated particles [69]. In that case, the reduced viscosity, η_{sp}/C of a solution (for non-interacting spherical particles) is independent of concentration, C [134]:

$$\eta_{sp}/C = k/\rho \qquad (9)$$

where k is a constant and ρ is the density of the particles. Further aging leads to aggregated structures and causes a progressively larger dependence of η_{sp} on C, increasing system viscosity. As the shear rate is increased, these tenuous aggregates break down releasing immobilized liquid and thus reducing

viscosity. This corresponds to shear thinning behavior. According to the Huggins equation, chain-like or linear polymers show a concentration dependence of the reduced viscosity [135]

$$\eta_{sp}/C = [\eta] + k[\eta]^2 C \qquad (10)$$

where $[\eta]$ is the intrinsic viscosity and k is a proportionality constant. Therefore the progressively larger dependence of η_{sp}/C on C with aging time may be explained as arising from a gradual progression of the silicate structure from small noninteracting species to extended, weakly branched polymers [93]. Further aging leads to extensive network formation imparting elastic character to the system which can be indicated by the yield stress in the shear stress versus shear rate curve. After exceeding the yield stress, the shear thinning behavior and hysteresis are observed (thixotropic flow behavior) [93].

Both Newtonian and non-Newtonian behaviors have also been observed for alumina sols [136] while Wolf *et al.* [137] have shown, using zirconium acetate, that sols prepared by different methods exhibit also different rheological behavior, such as Newtonian, shear thinning, or thrixotropic flow [69].

Spinnability is a term, usually used to describe materials ability to elongate under applied external forces and to form long slender liquid threads with the ultimate aim to prepare fibers. Additionally, the term spinnability can also be used to describe materials behavior in preparation of films and other structures. When using alkoxide solutions, the best spinnability is observed when the viscosity behavior is highly shear thinning but not thixotropic [138]. Shear thinning behavior alone however is not sufficient for spinnability. Apparently a very high viscosity without premature gelation is necessary to prevent the drawn liquid jet from breaking up into droplets. From the aqueous polymerization-condensation processes with silicon alkoxides it is noted that for any particular concentration and extent of condensation, weakly branched "extended" structures, e.g., chains or rods, are more efficient than compact structures, e.g., uniform particles, in increasing the viscosity. Overlapped extended structures interact at lower concentrations, which also explain the concentration dependence of the reduced viscosity [93].

1.3.3. Fibers from liquid jets and structures from viscous sols

Collimated streams of matter with more or less columnar shape, i.e. jets, have fascinated researchers already from 1833 when Savart observed tiny undulation on the jet surface just prior the homogeneous flow of water disintegrated to droplets [139]. Researchers were able to demonstrate later on that cohesive properties of liquids, most often surface tension, are promoting the breakup of once formed jet. Besides fiber formation, discussed more thoroughly afterwards, the knowledge about jet formation and disintegration has been

implemented successfully into technological, scientific and everyday achievements such as medical diagnostics, sprays and coatings, nuclear fission, ink-jet printing, diesel engine technology, micro- and optoelectronic, agricultural irrigation and so on [140]. Jet dynamics can also be used to evaluate liquids surface tension, viscosity or non-Newtonian rheology – important properties of precursor materials for many industrial applications and processes [140].

The factors leading to jet failure are summarized in the Ullmann's Fibers Handbook [127] as follows: A fluid as-spun filament is thought to break by two mechanisms [141]. The first of these is cohesive failure in which fracture occurs when the tensile stress exceeds the tensile strength of the material at some point along the path of filament formation. Tensile strength depends on the energy of cohesion (critical elastic energy) of the material. Tensile stress can built up if the fluid, in contrast to ideal viscous Newtonian media, is able to store energy of deformation, i.e. if it is viscoelastic. The second failure mechanism is termed capillary wave failure and depends on the ratio of surface tension to viscosity. The larger the ratio, the more rapid is increase in the amplitude of initially minute waves on the filament surface. After a certain distance, the capillary filament is divided into droplets and breaks [127].

To obtain a fiber from high-viscous precursor one needs also to solidify the liquid jet before breakup via drying (dry pulling), cooling (melt pulling), osmosis (wet pulling) or as a result of chemical reaction [127, 142]. Fiber diameter is limited by the precursor material properties and jetting method. For example, because of the breakup, it is fairly difficult to mechanically draw fibers thinner than 1μm. The theoretical calculations predict that fundamentally it is not possible to mechanically draw fibers thinner than 200 nm, while electrospinning allows obtaining fibers with diameters less than 100 nm [143]. The characteristics of the precursor material also determine the outcome fiber structure and dimensions as was demonstrated by Ondarcuhu *et al.* who used concentrated oligomeric precursor solutions instead of polymer solutions to draw fibers thinner than 200 nm [144]. The explanation for the result is that the oligomeric solution with low molecule mass does not consist of entanglements compared to polymeric systems and so the cohesive forces are largely reduced.

Precursors for fiber preparation from metal alkoxide sols are achieved by controlling materials chemical composition with the *R*-values (aqueous hydrolysis-condensation) or with the heating temperature (non-aqueous processes). High viscosities are generally achieved by concentration of the sol trough solvent evaporation [131]. During the fiber processing from metal alkoxide sols, particles start sliding under external forces, forming long slender viscous jets that solidify (gel) upon removal of the solvent and cross-linkage of the particles [145]. Further solvent evaporation that accompanies fiber drawing presumably causes a sufficient increase in viscosity to stabilize the drawn fiber due to the strong concentration-dependence of viscosity [93]. On the other hand, removal of solvents during the fibers formation would lead to formation of fibers with noncircular cross-section [146].

When suitable sol concentrations and viscosities are selected, thin films onto suitable substrates can be deposited using dip-, spin- or spray -coating [147]. Reedo *et al.* has also demonstrated that gel films can be used to obtain spontaneously formed microrolls (1 µm to 50 µm in diameter and up to 2 mm long). For that, only the surface layer of the precursor is gelled by exposing it to humid air, remaining sol layer under it un-gelled. Using suitable solvents and under proper conditions the gel sheets have a tendency to spontaneous roll-up, which can be explained by mechanical stress imbalance that originates from drying and polymerization-condensation processes [148]. Formation and dimensions of the microrolls are controlled with the precursor viscosity and with the extent of the gelling processes in the initial film [147].

In molding of structures from sol-gel materials, hydrodynamic flow of the sol and gelation at sols surface play important role in the process. Naturally, also the sols intrinsic properties such as viscosity should be counted. The higher the viscosity, the faster the gelation takes place and the smaller are distortions of smeared structures caused by capillary forces and by mass loss during gelation. If gelation is too fast and sample thickness is too large, cracks can appear. If thick films or even monoliths are needed to prepare, the number of unwanted cracks can be minimized in several ways, for instance, by modifying the precursor by adding different stabilizers into it [71]. Also environmental conditions (especially humidity) are significant, since speed of gelation process depends directly on the amount of water vapour in the environment [149].

1.4. Carbon nanotube reinforced ceramic matrix composites

Materials science community has exploited the CNTs potential as reinforcements and/or toughening agents for brittle ceramics to develop advanced ceramic matrix composites (CMCs) with superior mechanical performance and tailored thermal and electrical properties [150]. High aspect ratio of this tubular form of carbon can be utilized for alignment of the CNTs by shear forces to create composite materials with additional level of hierarchy. Furthermore, CNTs high aspect ratio becomes advantageous when their percolation at low concentrations is needed [151]. Electrical conductivity and mechanical strength of the composites can be greatly enhanced by addition of a small amount of CNTs needed for the creation of homogeneous network throughout the host material [150]. A wide variety of polycrystalline ceramic matrices including Al_2O_3, MgO, ZrO_2, SiC, TiN, $BaTiO_3$ etc. [152] has been reported as potentially applicable in fuel cells, supercapacitors, gas sensors, ferroelectric capacitors, photocatalytic films, thermal barriers, tissue engineering, electromagnetic shielding, armours etc. technologies [150]. Tailoring CNTs unique properties with aforementioned ceramics can result in composite materials that could enhance existing applications and open ways to new ones.

According to Zapata-Solvas *et al.* [150] the properties of CNT-reinforced CMCs depend on: (i) degree of homogeneity of the dispersion of CNTs within the matrix ensuring the absence of CNTs agglomerations; (ii) avoiding damage of CNTs while processing, either during dispersion or consolidation; (iii) optimum bonding between CNTs and ceramic matrix interface with the aim of originating interfacial compatibility and strong adhesion. CNTs dispersions throughout ceramic matrix are mostly achieved by conventional powder processing [153], colloidal processing [154], electrophoretic deposition [155], *in situ* growth of CNTs by e.g. catalytic chemical vapour deposition (CVD) [156] or by sol-gel processing [157].

Compared to sol-gel processing, aforementioned competing methods for obtaining CMCs have several drawbacks. For example, powder processing uses mostly ultrasounds or ball milling to mix raw CNTs and ceramic particles under wet conditions followed by powder drying, crushing and sieving and finally densifying the mixture by hot pressing. However, the absence of any driving force to distribute the CNTs from the powder particle surface into the bulk results in nonhomogeneous composite material with agglomerated CNT bundles [152]. Another method, electrophoretical deposition, is only suitable for production of coatings and films [158] achieved via the motion of charged particles in a suitable aqueous solution towards an electrode under applied electric field (Figure 15) [152]. Colloidal processing use dispersants, surfactants or chemical functionalization based surface modifications of CNTs to increase suspension stability and interaction between the tubes and ceramic matrix. Heterocoagulation is generally used to initiate matrix particles deposition from suspension to nanotube surface. Ceramic coating on CNTs in turn screens the undesirable attractive interaction between the tubes, preventing agglomeration and facilitating the production of well-dispersed composites. However, the sintering and removal of dispersants and surfactants from composites without damaging CNTs can be challenging [152]. CVD, described in chapter 1.1.2, can be used to grow CNTs directly on the surface of ceramic matrix grains due to metal impurities doping the surface and acting as catalysts. As shown by Peigney *et al.*, *in situ* growth of CNTs on ceramic particles enables composites with reasonably well-distributed networks of CNTs [159] but the downside of the method are poor sinterability and the undesirable presence of amorphous carbon in the final composites [156].
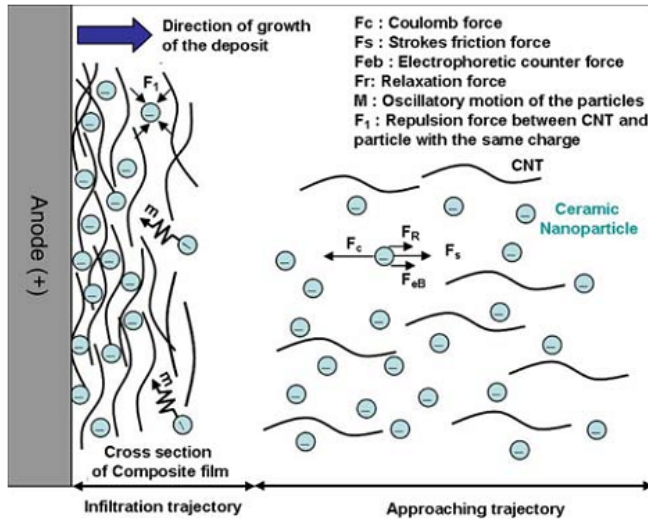
Figure 15. Schematic illustration of the electrophoretic co-deposition of composite films containing CNTs and ceramic nanoparticles. From Boccaccini *et al.* [158].

1.4.1. CNT-reinforced CMCs by sol-gel method

Sol-gel method, when used to prepare CMCs, involves the production of metal oxide nanoparticles based solid gel network, wherein CNTs are mixed and entrapped, followed by the calcination of the dried gel mixed with CNTs [150]. Up to date the vast majority of sol-gel prepared CNTs composite works have been focused on the silica systems such as SiO_2 glass [160] or alumino-borosilicate [161, 162]. Only a limited amount of works are available on CNT-reinforced metal oxide systems, which describe the preparation of CNT-metal oxide powders [163] and thin films on substrates [164] by sol-gel techniques.

The main issues when preparing CMCs by sol-gel methods are related to breaking CNT agglomerates during the sol-gel processing. It has been fre-quently demonstrated that simple mixing techniques seldom have led to satisfactory results. Thus for instance, Mo *et al.* were able to demonstrate a good dispersion of pristine CNT in aluminium tri-sec-butoxide based powders without using any surfactants. However, obtained Al_2O_3-MWCNT composites still contained some agglomerates and only moderate increase in fracture toughness was achieved [157]. Therefore nowadays more elaborate mixing techniques are used such as utilization of surfactants, various pre-treatments, ultrasound methods etc. For example, using sodium and ammonium stearates as surfactants, MWCNT-ZrO_2 composite crystalline powders have been success-fully obtained from mixing 0.5% CNT with zirconium (IV) propoxide sol [165]. Authors observed MWCNTs with fully coated zirconia matrix which is a result of a very good adhesion between the tubes and oxide layer.

It has been observed by Vincent *et al.* that compared to simple mixing of oxide precursor with CNTs, pristine CNTs solutions are more stable when the oxide nanoparticles are produced in the presence of CNTs [166]. Investigating dip-coated thin films with transmission electron microscope revealed oxide nanoparticles on the surface of the tubes that screen the undesirable attractive interaction between the nanotubes and thus prevent agglomeration. Jitianu *et al.* proved using titanium(IV)propoxide and titanium(IV)ethoxides that CNTs can be coated by a thin continuous oxide layer [167], which parameters can be controlled by process parameters, such as reaction time [168], reaction composition, and the choice of metal precursor [169]. By using sol-gel method to coat CNTs with a thin layer of Al_2O_3 [170], TiO_2 [171] or SnO_2 [172], it was possible to synthesize well-dispersed discrete composite fibers or functionalize CNTs in order to manipulate adhesion/bonding between CNTs-composite fibers and a ceramic matrix [150].

It is also interesting to note that dip-coated CNT-tantalum oxide based thin films, for example, proved to be mechanically more resistant to mechanical scratching and had good sticking strength with the substrate [164]. Note that not only mechanical properties but also other properties can be enhanced using CNTs. Thus e.g. SnO_2-SWCNT composite thin films prepared by Gong *et al.* showed up to three magnitudes of greater sensitivity and faster response time when used as gas sensors [173].

1.4.2. CNT percolation theory and electrical conductivity of CNT-reinforced CMCs

The ceramic matrix of composites are usually considered as electrically non-conductive (10^{-10} to 10^{-15} S/m) [174]. Electrical conductivity in CNT-ceramic composites is the result of the percolated network of CNTs throughout the ceramic matrix. Percolation effect involves a sudden change in a macroscopic property at a critical percolation threshold [150]. The property, electrical conductivity in this case, can be related to the concentration by scaling law as follows [175],

$$\sigma_m = \sigma_c (f_{CNT} - f_c)^t \text{ for } f_{CNT} > f_c \tag{11}$$

where σ_m is the electrical conductivity of the CNT-reinforced CMC, f_{CNT} is the volume fraction of CNTs in the composite, f_c is the critical volume fraction or percolation threshold and σ_c and t are fitted constants related to intrinsic electrical conductivity of the CNTs and the dimensionality of the system, respectively [150]. From the theoretical considerations the percolation threshold depends mainly on the aspect ratio of the conductive filler; the higher the aspect ratio the lower is the percolation threshold [176]. In practise, also other factors, such as filler hardness, filler distributions, matrix properties and processing

techniques, can also have effects on percolation and conductivity [177, 178]. Therefore, electrical percolation thresholds in CNT reinforced CMCs have been reported to range from as low as 0.18 wt% to more than 30 wt%, and most of the measured electrical conductivities range from 10^{-2} to 10^3 S/m [150]. Typical dependency of conductivity on CNT concentration in CMCs is demonstrated in Figure 16. Near the percolation threshold the conductivity follows the power law and exhibits a typical insulator-conductor transition [151].
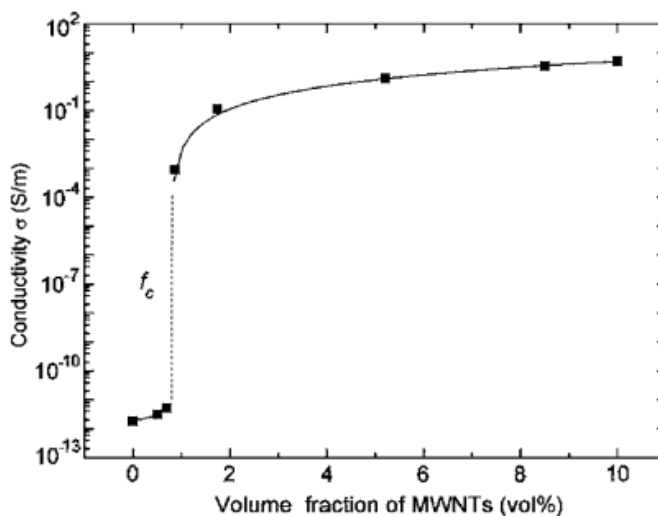

Figure 16. Plot of conductivity of alumina/MWCNT powder composites as a function of the MWCNT content at room temperature. From Ahmad *et al.* [151].

From the viewpoint of resistor circuits, there are only two sources of resistance for a percolating network of carbon nanotubes. One is the resistance along the nanotube itself, and the other is the contact resistance between crossing nanotubes [174]. Electrical properties of pure CNT networks are dominated by the contact resistance between CNTs, which depends on several structural parameters such as the chirality, contact angle, and tube-tube distance. For instance, metal-metal and semiconductor-semiconductor contacts form tunnel junctions whereas a metallic-semiconductor contact behaves as a Schottky diode and thus the reported resistances vary from tens of kilo ohms to hundreds of mega ohms [176]. However, when CNTs are dispersed in a ceramic matrix, a thin insulating film may form between a pair of junction nanotubes, which increases the contact resistance [179].
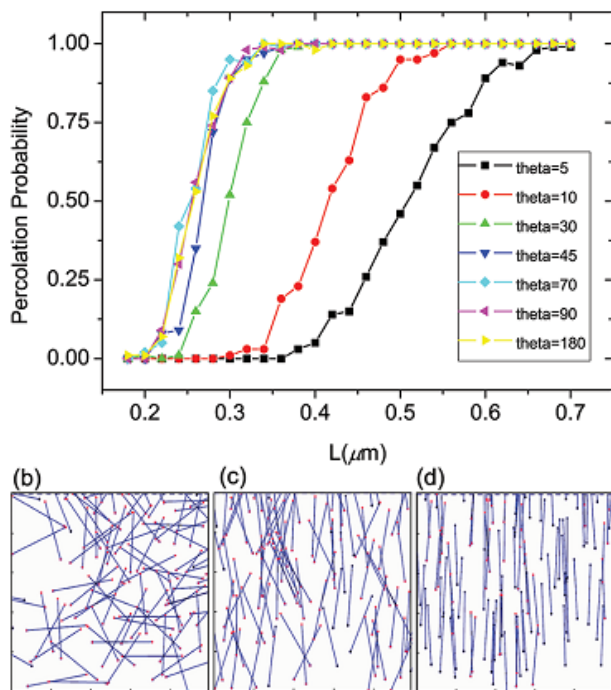
Figure 17. (a) Theoretically calculated percolation probability of as a function of length for different angular distribution of 100 CNTs within the simulation cell. (b,c,d) Typical distributions of CNTs when the anisotropic angle θ is 90°, 30°, and 5°, respectively. From Zeng *et al.* [181].

Investigating CNT films, Behnam *et al.* found that the film conductivity depends on the alignment of nanotubes such that the highest conductivity is obtained at partially aligned CNTs [180]. This can be explained by the fact that, as the nanotubes become more aligned, they form conduction paths with fewer junctions and shorter lengths between the source and drain. However, as anisotrpy is further reduced, resistivity starts to increase significantly. This is due to the fact that, as the nanotubes become even further aligned, the number of conduction paths begins to decrease significantly. For example, in the case of almost perfect alignment, each nanotube forms only very few junctions with its neighbours, since it lies almost parallel to them. As a result of this competition between the decrease in the number of junctions and lengths of the conduction paths (which decreases the resistivity) and the decrease in the number of conduction paths (which increases the resistivity), the resistivity minimum occurs for a partially aligned rather than a perfectly aligned nanotube film [180]. To summarize, decrease in the degree of anisotropy in CNT dispersion leads to a corresponding increase in the percolation probability (Figure 17), thereby lowering the electrical percolation threshold [181].

High aspect ratio nanotubes have been observed to tend to curl up and also form bundles in composites. Although the theoretical simulations reveal that the percolation threshold increases with an increase in the degree of waviness [182], the effect of waviness to percolation threshold remains relatively small compared to aforementioned effects [183]. Grujicic *et al.* [184] has calculated the effect of bundles on percolation and, as expected, the percolation threshold increases with increasing the bundle radius [183].

1.4.3. Rheology of CNT-filled systems

Characterization of CNT-reinforced sol-gel systems by rheology helps to understand influence of CNTs on sol-gel transition, nano- and microstructure of the obtained materials, and also enables better control over processing parameters [145]. The rheological parameters are influenced by interactions between constituents in the system, their state of dispersion, as well as by the shape and orientation of the dispersed particles. Therefore, rheological measurements could reflect morphological changes in CNT-filled sol-gel systems. Studies referring to CNT-reinforced sol-gel rheology are quite rare. Majority of the experimental and theoretical rheology studies on CNT-filled systems are done with polymers or epoxy resins. However, many results and conclusions are expected to be similar with alkoxide based sol-gel systems.

Addition of nano-particles into a liquid changes the suspension viscosity η expressed as

$$\eta = \eta_0(1 + [\eta]\phi_c + h\phi_c^2)$$ (12)

where η_0 is the fluid viscosity, $[\eta]$ is a suspension intrinsic viscosity, ϕ_c is a particle volume fraction and h is the Huggins coefficient, which characterizes the strength of particle-particle pair interactions [185]. According to standard models, increasing suspension viscosity is related to the fact that particles acquire a stable adsorbed layer with a hydrodynamic size larger than the core particle diameter. On the other hand, if the matrix segments adsorb weakly or not at all, a depletion of the segments at the particle surfaces will lead to an attractive potential of mean force, again raising h but reducing $[\eta]$ [185]. As indicated above, positive intrinsic viscosities are associated with adsorbed layers at the particle surface. According to Kim *et al.* [185], negative values are less well understood and are associated with i) particles whose diameter is on the order of the size of the polymer radius of gyration (R_g) [186], ii) the polymer being above the entanglement molecular weight [187], and iii) particle spacing being on the order of the polymer radius of gyration [188–190].

Experimental study by Tuteja *et al.* [191] demonstrated that addition of polystyrene nanoparticles to linear polystyrene leads to viscosity reduction only when the polymer molecule is entangled and confined. A large decrease in the

viscosity of a semicrystalline polymer with the addition of *in situ* prepared silica nanoparticles in a narrow concentration window was demonstrated by Jain *et al.* [192].Viscosity drop was explained by selective adsorption of long polymer chains on the nanoparticles and by interparticle distance (Figure 18).
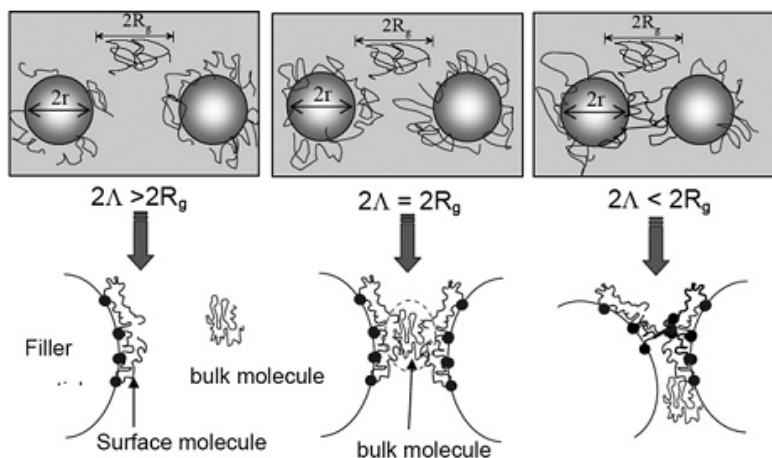

Figure 18. Schematics showing the effect of interparticle distance (Λ) on the particle–particle and particle-polymer interactions. (A) If the interparticle distance is larger than the radius of gyration of polymer (R_g) then there are interactions or entanglements of polymer chains adsorbed on the surface. As the interparticle distance approaches R_g, the adsorption approaches a maximum and when the interparticle distance is lower than R_g, the adsorbed polymer chains start to feel the presence of other particles and parts of the chains also adsorb on other particles forming bridges. (B) Schematics showing the bridging effect when the interparticle distance is less than R_g, resulting in network formation or superstructures in the melt which increase the viscosity. From Jain *et al.* [192]

Theoretical simulations demonstrate a pronounced change in viscosity affected by the nature of the nanoparticle–matrix interaction (i.e. attractive, neutral or repulsive interactions). The viscosity is increased for attractive interactions and reduced for repulsive systems [193]. In the presence of even insignificant amount of fillers, such as CNTs or carbon nanofibers (CNFs), the initially Newtonian liquids will exhibit non-Newtonian behavior [194]. Investigating SWCNT-epoxy suspensions, Advani *et al.* [195] have demonstrated that similarly to the percolation threshold the rheological response is a function of CNTs orientation, aspect ratio, concentration, and surface treatment. The rheological behavior and morphology investigation of melt phase polystyrene/CNF (50–150 nm in diameter) composites show that both shear and extensional viscosities increase with increasing nanofiber concentration [196]. CNTs suspensions on the other hand show a much stronger shear thinning effect when compared to CNFs or carbon black suspensions with the same concentrations [197]. This is

probably because of the more pronounced effect of high aspect ratio of the CNTs [198].

CNTs addition increases also storage modulus G' and loss modulus G'' of the composites, however, the effect on G' is generally larger [197, 199]. At low frequencies, the storage modulus shows a plateau that is usually observed at high CNT loadings indicating the presence of a physical network of CNTs [200]. Ma *et al.* [201] studied the rheological behavior and microstructure of the low viscosity CNT-epoxy resin and showed that treated CNT suspensions generally revealed a smaller shear thinning effect compared with untreated CNT suspensions. The addition of chemically treated CNT to the fluid was found to significantly increase the filament breakup time in extensional flow as a result of CNT orientation along the filament stretching direction. Additionally, the filaments from the chemically treated CNT suspensions were smooth, while the filaments from untreated CNT suspensions behaved in a non-uniform way with local fluctuation in filament diameter [201].

2. AIM OF THE STUDY

The main purpose of the thesis was to study formation mechanisms of nano- and microstructures from metal alkoxides, and to search for ways to increase their electrical properties by doping with carbon nanotubes.

The original contribution of the work is divided into two main parts. The aim of the first part of the study was to find new approaches for preparing nanostructured oxide materials from highly viscous metal alkoxide sols. The second part of the study focuses at carbon nanotubes/oxide composite materials, their formation methods, characterization, and properties. The particular objectives of the study were:

- elaboration of suitable precursors for preparing nanostructured oxides;
- elaborating different methods applicable for preparation of controlled shape nanostructured oxides from the precursors;
- determination of internal and external parameters affecting shaping of gel structures;
- analysis of the structure formation of the precursors and oxide structures;
- elaboration of methods for introducing CNTs into precursor materials;
- analysis of CNT influence on precursor material properties;
- characterization of CNT-oxide composite structures.

3. EXPERIMENTAL METHODS

Experimental work of this Ph.D. thesis can be divided into four parts – precursor materials preparation, characterization of precursor materials, preparation of metal oxide structures, and characterization of final oxide materials.

During the research a large variety of different alkoxides were used. Whenever possible, commercial alkoxides were utilized. Commercially unavailable metal alkoxides were synthesized following generally known routines. Precursor materials for gel structures preparation were obtained by aqueous (AQ) or non-aqueous (NAQ) treatment of metal alkoxides. The process of metal alkoxide hydrolysis-condensation with water was similar for all used alkoxides, and after the excess solvent and water was removed, highly viscous samples were obtained. Ultrasonication procedures were used in preparation of precursors of metal-oxo-alkoxides composites with carbon nanotubes.

In the second step, precursor materials were characterized by conventional methods and also sometimes by unconventional techniques when conventional methods were not applicable.

Next, obtained viscous precursor materials were used to prepare different gel structures with and without CNTs. Several experimental set ups and instruments were developed in order to prepare specialty shapes. Initially obtained xerogel structures were further processed into dense oxide ceramics.

Finally, obtained dense ceramic nano- and microstructures were imaged and characterized.

3.1. Precursor materials preparation

Neat alkoxides for precursor materials preparation (Papers I–VIII)

$Ti(OPr)_4$, $Ti(OBu)_4$, $Zr(OPr)_4$, $Zr(OBu)_4$ and $Hf(OBu)_4$ were commercially available. Metal alkoxides like $Sn(OPr)_4$, $Sn(OBu)_4$ and $Ce(OBu)_4$, that were commercially unavailable were synthesized prior further experiments.

Syntheses of $Sn(OPr)_4$ and $Sn(OBu)_4$ were carried out as described in [202]. Detailed synthesis of $Ce(OBu)_4$ is described in Paper I. After removal of solvents in vacuum, the alkoxides were obtained as viscous syrup-like brown liquids.

Precursor materials preparation by AQ treatment of metal alkoxides (Papers I–VIII)

Typically five to ten grams of alkoxide aliquots was used as the starting material for the precursor preparation. Hydrolysis-condensation process was initiated by adding water solution in the corresponding alcohol (butanol or propanol) acidified with concentrated HCl. If necessary, the mixture could be doped with other metals just after the addition of water. This was necessary in order to improve the materials conductivity for further electron microscopy

observations, for example (see chapter 4.4). To transform the obtained mixtures into viscous samples, the solvents and low molecular mass organics were removed by evacuation. The main parameter affecting the precursor materials viscosity, $R=[H_2O]/[M(OR)_n]$, is different for every alkoxide. Hence, the value of R was selected according to the desired metal alkoxide gel viscosity and particular experiment.

Exposing the precursors to air resulted in immediate formation of thin solid layer on the materials' surface due to polymerization-condensation caused by water vapour in air. In closed plastic syringes the precursors remained stable for at least several months.

Precursor materials preparation by NAQ treatment (thermolysis) of metal alkoxides (Paper I)

NAQ treatment, which is an alternative method for obtaining viscous precursor materials from metal alkoxides, was demonstrated using $Sn(OBu)_4$. In thermolysis the condensation was initiated by slowly increasing the temperature of a reaction flask containing $Sn(OBu)_4$ over 8 h period until reaching 275 °C. At this temperature primary tin alkoxides transform to oxides, as pointed out by Maire *et al.* [203]. To achieve uniform heating, the flask with a vigorously stirred substance was heated in a silicone oil bath.

CNT doped precursor materials preparation (Papers III, VI–VIII)

AQ treatment of titanium and tin alkoxides with different types of CNTs were used to prepare CNT-reinforced CMCs. All CNTs were synthesized by CVD and were not functionalized or pretreated before introducing them into metal alkoxides.

In the stage of preparation of an initial suspension, CNTs (e.g. 0.01 g) were first added into corresponding alcohol (e.g. 10 mL) inside a 15 mL metric cylinder and were then treated with ultrasonic wand (24 kHz and 200 W) for 30 minutes. Preliminary high powered ultrasonic agitation in relatively small beaker was necessary to successfully de-agglomerate individual CNTs from bundles. The suspension was then introduced into titanium(IV)propoxide (e.g. 10 g) and a water-propanol solution was added to the mixture. The molar ratio of water to titanium(IV)propoxide was chosen to be the same as when precursor without CNTs was prepared. During removal of the excessive solvent with a rotary evaporator, an ultrasonic bath (37 kHz and 80 W) was used instead of ordinary heating bath. Although high powered sonication is very effective for producing uniform CNT suspensions, prolonged exposures to ultrasonic waves could also damage CNTs to extent where their electrical properties are significantly decreased [204]. For this reason, relatively mild sonication conditions (80 W) sufficient to maintain high quality dispersion without severely damaging CNTs were selected in the solvent removal stage. Importance of the sonication was decreased when the viscosity of the metal-oxo-alkoxide/CNT suspension increased up to 10–10000 poise [138] as the

tubes remained separated from each other due to the high viscoelastisity of the matrix. After removal of the solvent, visually homogeneous samples were obtained for further investigation.

3.2. Precursor materials characterization

Precursor materials were characterized by evaluating their viscosity, surface tension rheological properties and morphology. In the present work two methods for rheological characterization of precursor samples were used: conventional rotational rheometry and original technique developed in collaboration with Tallinn University of Technology [205]. Inner structure of the precursors was investigated by using infrared spectroscopy, X-ray diffraction analysis and small-angle X-ray scattering analysis.

Viscosity measurements (Papers I, II, IV)

One of the important parameters describing the properties of a sol-gel material is its viscosity. Typical sols used in conventional technological processes like spin and dip coating include large amount of solvents that needs to be evaporated before the beginning of gelation process. The viscosities of such sols are usually around 1 poise. In our case, the sols did not contain any solvents and therefore their viscosities were at least two orders of magnitude larger. Viscosities were determined by Stokes method measuring free falling time of a 0.032 g metal ball that was dropped into the mixture. A calibration test proved that the method enabled us to measure the viscosities of the precursors from 100 poise up to several thousand poise with an uncertainty less than 10%.

Measurements of the surface tension coefficient (Paper I)

The surface tension coefficient was measured by the inverted vertical pull surface tension method as described in [206]. To avoid solidification of the sample surface, the measurements were performed inside a reaction flask in which alkoxide materials were in equilibrium with their vapours. A platinum rod, 0.5 mm in diameter, was first immersed into the liquid and was then pulled out from it in 0.01 mm steps. The force of the liquid acting on the rod in effective steady-state motion was measured using balances with the resolution of 0.1 mg. The surface tension coefficient was calculated from the value of the force measured immediately before breaking up of the liquid jet.
The method was calibrated in the high-viscosity region using standard liquids like glycerol, and the accuracy was within 5%.

Conventional rotational rheometry characterization (Paper I)

Rotational rheometry is a powerful technique for the measurement of complex shear rheology for a wide range of liquids, varying from dilute solution to highly viscoelastic composite materials. The liquid sample is filled into the

space between the two plates, cone and plate or between concentric cylinders (Figure 19). The measurement is carried out by rotating one of the geometries while the other is fixed. This method has proved to be very useful for flow behavior of sols for sol-gel materials [69].
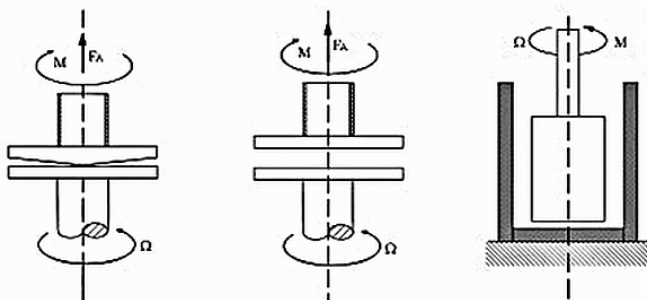

Figure 19. Schematic drawings of various measuring geometries (cone-plate, plate-plate and concentric cylinders) [207].

The rheological characterization of samples was carried out with a Haake rotational rheometer Mars II using the plate-and-plate test geometry (plate diameter 20 mm), at 20 ± 0.1 °C and humidity below 20%. The data on viscosity versus shear rate were averaged over 30 s for each shear rate value. Oscillation stress sweep tests were carried out at the frequency of 10 rad s^{-1} and strain amplitudes of 0–30%. Oscillation frequency sweep tests were performed for frequencies between 0.01 and 20 Hz at the strain amplitude of 0.1%, that is, within the linear viscoelastic region.

Extensional rheology technique (Paper III)
As extensional flows can have a tremendous effect on final properties of sol-gel materials, the extensional rheology parameters are important for fiber spinning, thermoforming, film blowing, foam production etc. Because of high reactivity of metal alkoxides with humidity, their rheological properties have to be studied under the conditions of equilibrium state with inherent vapor and in a dry air [205]. The main advantage of the technique is the possibility of the measurements of the materials parameters in the vessel where they were prepared.

A schematic diagram of the experimental configuration is shown in Figure 20. A rigid metallic rod (4) with a circular plain endplate of 0.5 cm in diameter is inserted into a bulb (5) filled with a sample liquid. The rod is then pushed down until it touches the liquid surface. The endplate is then quickly moved apart to a final separation of 1.5 cm by servomotor (1) and the relaxation of the jet is monitored [205]. During the period of relaxation, the profile of the thread in mid-filament region is monitored. The geometrical dimensions and parameters of the motion-control system determine the range of experimental parameters accessible in a given filament thinning device. The filament thinning

under the combined actions of surface tension, gravity and rheological effects in the mid-filament region was monitored by a high-speed camera MC1310 Mikrotron GmbH (7), with maximum resolution of 1280×1024 pixels at 500 fps. After the test, the video frames were processed using a specially developed computer program. As a result, evolution of a minimum filament diameter until thread breakup was obtained [205].
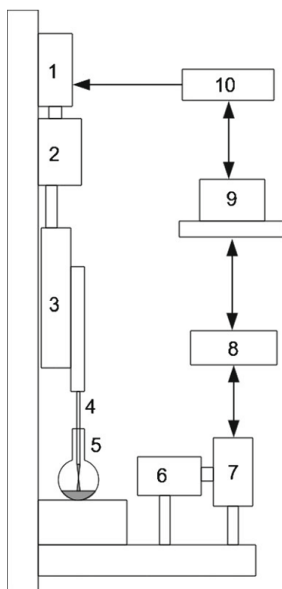

Figure 20. The scheme of the test device for measuring extensional rheology parameters: *1* servomotor, *2* multiplier, *3* moving platform, *4* rod, *5* transparent bulb, *6* optics, *7* high-speed camera, *8* frame grabber, *9* computer, *10* servomotor controller. From the Hussainov *et al.* [205].

Fourier transform infrared spectroscopy (Paper I)

Fourier transform infrared spectroscopy (FTIR) is used to acquire broadband near-infrared to far-infrared spectra of a sample. FTIR spectrometer obtains infrared spectra by first collecting an interferogram of the sample signal using an interferometer, and then performs a Fourier transform of the interferogram. Method is extensively used to determine nature of chemical bonds in samples and thus identify containing substances [208].

X-ray diffraction analysis (Paper I)

X-ray diffraction (XRD) is a technique for determination of the crystal structure, orientation of crystallites and the mean size of crystallites of a sample. The three-dimensional structure of non-amorphous materials is defined by regular, repeating planes of atoms that form a crystal lattice. When a focused

X-ray beam interacts with these planes of atoms, part of the beam is diffracted by the sample and we can measure the distances between the planes of the atoms that constitute the sample [209].

Small-angle X-ray scattering analysis (Paper I)

Small-angle X-ray scattering (SAXS) method uses monochromatic beam of X-ray, synchrotron or neutron source to illuminated the sample from close range and scattered radiation is registered by a detector. SAXS has a resolution of 1–3 nm that is sufficient to measure the shapes and sizes of nanoparticles and large molecules [210].

3.3. Preparation of different gel structures with and without CNTs

Fibers preparation (Paper I, III, VI–VIII)

The fibers were directly drawn from the precursors using two different procedures – pulling from dry to humid atmosphere and pulling in humid atmosphere.

In the first method, the fibers were drawn from precursors by immersing a glass rod into the precursor liquid and pulling it out from the reaction bulb at a speed of ~1 m/s. The surface of the formed liquid precursor jet solidifies immediately in ambient atmosphere (relative humidity 20–50%) as the reaction with water vapours generates -O- bonds between metal-oxo nanoparticles (Figure 21a).
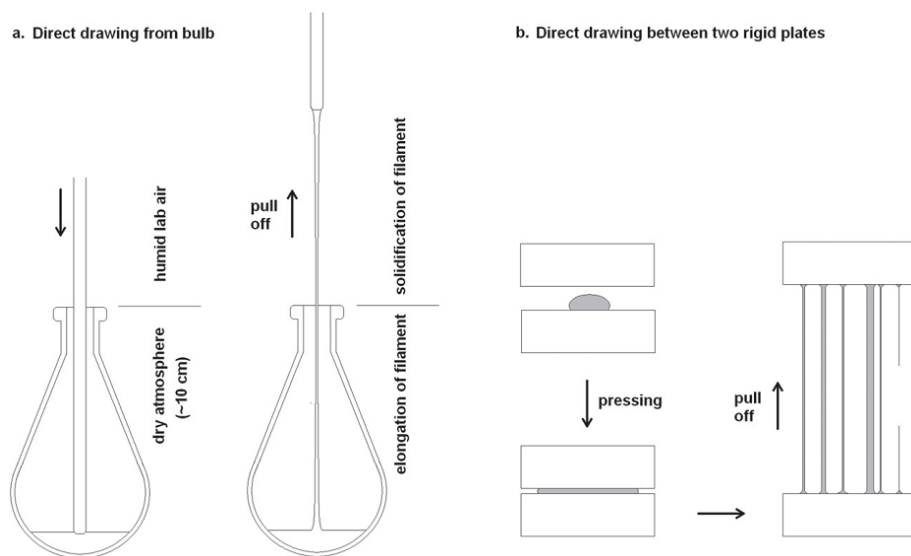

Figure 21. Principles of fiber drawing: (a) from dry atmosphere in the flask into humid atmosphere and (b) in humid atmosphere. From Paper I.

For the fiber pulling in humid atmosphere, a 10–20 mg drop of the precursor was pressed into 100–200 μm film between two glass plates, which were then pulled apart at a speed of ~1 m/s. This method differs from direct drawing from the flask in that the jets are exposed to humid air all the time (Figure 21b).

As-prepared fibers were aged for 1 week under normal laboratory conditions (relative air humidity 20–50%). Finally, the samples were baked at temperatures from 200 to 600 °C. As a result of described processes, 10–50 millimeters long fibers with diameters from 5 to 70 microns were obtained.

Preparation of needles (Paper II)

The needles were prepared from the viscous precursor materials as depicted in Figure 22. A special filament-stretching device was designed and constructed for pulling the needles. Unlike exponential pulling speed models usually exploited for viscosity analyses [211], our instrument maintains a constant speed in a range from 0.015 to 4 cm/s. In order to avoid polymerization-condensation of the precursor surface before starting the pulling, the instrument was designed to expose the liquid surface to humid air just prior to starting the pulling motion. The operations were carried out in controlled environments varying the relative humidity from 1.5 to 100% at room temperature (22.0 °C).
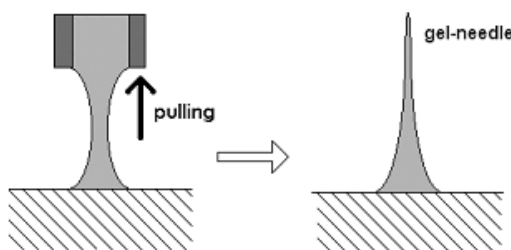

Figure 22. Schematic illustration of formation of the oxide needles by pulling viscous precursor jets. From Paper II.

Prepared needles were removed from the substrates about 15–30 s after their fabrication. Freshly prepared sticky needles were carefully positioned on quartz plates and left for ageing at room conditions for a week. Typically, after some hours the thicker part of the filament that was attached to the surface of the plates cracked due to mechanical stresses caused by shrinkage of the fragile material. After the 'ageing' the structures were baked in air, raising the temperature up to 520 °C.

Structured film preparation by tape casting (Paper IV)

Tape casting (also called doctor's blade method) is an industrial scale method, where a slurry is casted onto a substrate through a slit between the substrate and a blade. A film is produced which thickness is determined by the width of the slit. Suitable slurries are generally multicomponent mixtures of ceramic powders, solvents, plasticizers, and binders. The nature of the slurries is very

different compared to homogeneous sols used in sol-gel chemistry. However, it is interesting to note, that ceramic powders as one components of slurries are sometimes prepared by sol-gel methods (see, e.g. [212, 213]). Smearability and preservation of their geometrical shape after the coating are requirements for slurries in the tape casting. Typical viscosities of slurries are in the range of 0.1–100 poise [214].

Figure 23 shows the principle scheme of the tape casting machine. The sample holder is fixed onto the linear translation stage, which is driven from one side by a servo motor and stabilized from other side with two springs. Above the linear translation stage there is located a blade, which is pressed against the substrate. A high viscosity sol is directed to the moving substrate behind the immobile blade that smears the sol onto the substrate. The speed of the linear motion, blade pressure and the angle between the blade and the substrate can be varied. It is also possible to use either sharp and uniform, or structured blades from different materials.
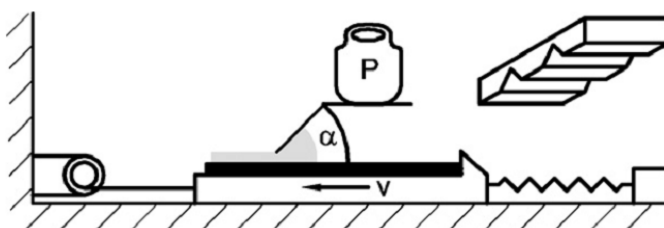

Figure 23. Working principle of the tape casting machine. Substrate is driven with speed V, on the immobile blade is applied pressure P and angle between the blade and the substrate is α. Substrate is black and sol is marked with grey. Inset on the right demonstrates the shape of structured blade. From Paper IV.

We used a structured blade prepared from a cleaved silicon monocrystal to demonstrate the feasibility of the sol-gel tape casting method. The structure was etched on silicon (1 0 0) surface and consisted from one-dimensional array of channels with triangular cross-section on the smooth wafer (see Figure 23). Etched structure had a period of approximately 14 μm. Base and depth of etched triangular channels were approximately 6 and 4 μm, respectively. The tape casting method sets no fundamental limitations to substrate material. In our case, the structured oxide precursor films were deposited onto an ordinary glass plate for convenience.

Powders preparation (Paper V)

A preparation of powders by the current sol-gel procedure can be considered to be the simplest, compared with the preparation of fibers for example. The precursor material was simply left to age in a humid atmosphere. The powder was formed during a couple of weeks of ageing as a result of the fragmentation of the precursor as the capillary forces overcame the strength of the gel. The powder was grinded in mortar and annealed in air.

3.4. Characterization of final oxide shapes

Electrical measurements (Paper III, VI–VII)

The electrical properties of the materials were measured by 4-point method. 4-point method is one of the most popular techniques for investigation materials conductivity because of its relatively low cost and simplicity of implementation. The simplest configuration to use with bulk samples consists of two current electrodes and two potential electrodes, as shown in Figure 24.
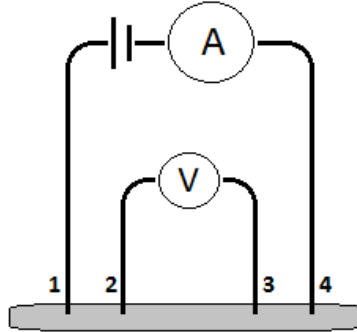

Figure 24. 4-point measurement of resistance between voltage connections 2 and 3. Current is supplied via connections 1 and 4.

The main problem in accurate electrical measurement is the inaccuracy of determination of the contact resistance between the measurement electrodes and the specimen. This is clearly the case for samples with low resistivity, but can also be a problem for more resistive samples if either the contact resistance is high or the contact is non-ohmic [215]. With the configuration shown in Figure 24, any effect of contact resistance is avoided, providing the contact resistance is much smaller than the input resistance of the voltmeter.

To ensure a firm electrical and physical contact between measuring electrodes and fiber material, indium-gallium alloy was used to fix fibers on the electrodes. The fiber was placed perpendicularly across the electrodes on In-Ga alloy droplets, as shown in Figure 25. The developed apparatus with the computer controlled switch enabled to measure 10 samples simultaneously. A SEM was used to measure dimensions of the fibers needed for calculating the electrical conductivity σ [215] using the following formula:

$$\sigma = \frac{l}{S \cdot R} \tag{13}$$

where l is the length of the fiber, S is the cross-sectional area of the fiber and R is the resistance of the fiber.
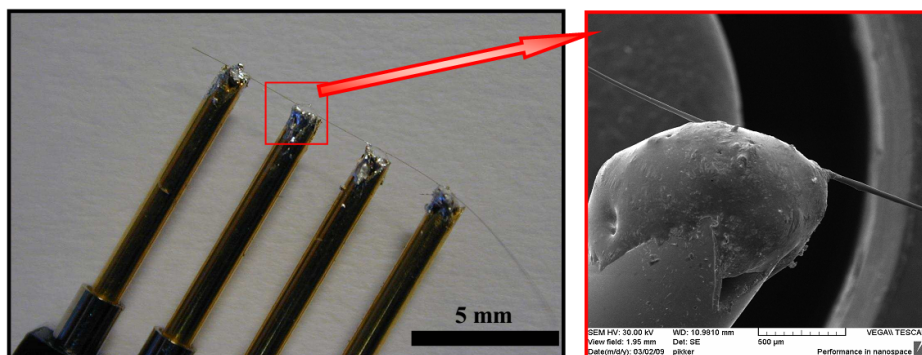
Figure 25. Image of a fixed fiber on In-Ga alloy contacts (left) and a SEM image of one of the contacts showing that the fiber is firmly in contact with the metal alloy (right).

Scanning electron microscopy and focused ion beam (Papers I–IV, VI–VII)

Scanning electron microscopy is used for inspecting materials surface topography. SEM uses a focused beam of electrons to generate a variety of signals at the surface of solid specimens. Image is generated by the signal of secondary or backscattered electrons collected from the interaction "points" over a selected area of the surface of the sample. The SEM is also capable of performing analyses of selected point locations on the sample; this approach is especially useful in qualitatively or semi-quantitatively determining chemical compositions (using energy-dispersive X-ray spectroscopy, EDS or wavelength-dispersive X-ray spectroscopy, WDS), crystalline structure, and crystal orientations (using electron backscatter diffraction, EBSD) [216].

A few instruments combine nowadays a SEM and focused ion beam (FIB) column. The FIB system uses typically a gallium ion beam to raster over the surface of a sample in a similar way as the electron beam in SEM. The generated secondary electrons are collected to form an image of the surface of the sample. Generally the ion beam is used for milling and the electron beam for imaging. SEM allows non-destructive imaging at higher magnifications and with better image resolution, and also more accurate control of the progress of the milling. The ion beam allows the milling of small holes in the sample at well localized sites, so that cross-sectional images of the structure can be obtained or that modifications in the structures can be made (Figure 26) [217].

During the course of this Ph. D. thesis three scanning electron microscopes were used. LEO 1430 VP was used to image tape casting films and parts of the needles. Tescan VEGA II microscope was used to evaluate dimensions of the fibers needed for the electrical conductivity calculations. FIB-SEM instrument FEI Helios NanoLab 600 (equipped with an EDS detector, Oxford Instruments) was used to image CNT-metal oxide composite fibers. The composite fibers were cut along their axis with focused ions to reveal inner morphology of the fibers and CNT distribution inside the material (Figure 42 and Figure 44).
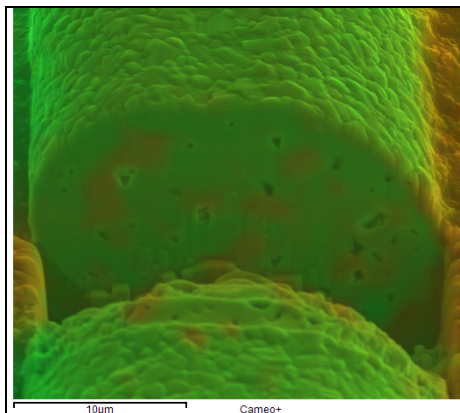
Figure 26. A SEM image of a Ni doped TiO_2 fiber, which has been cut with the FIB. EDS detector has been used to "map" the cut area and reveal Ni impurities (red) inside the fiber.

Atomic force microscopy (Paper I, IV)

Atomic force microscopy (AFM) relies on a scanning technique to produce very high resolution, 3D images of sample surfaces. The AFM measures ultra-small forces (less than 1 nN) present between the AFM tip surface and a sample surface. These small forces are measured by measuring the motion of a very flexible cantilever beam having an ultra-small mass. AFMs are capable of investigating surfaces of both conductors and insulators on an atomic scale if suitable techniques for measurement of cantilever motion are used [218]. AFM measurements are usually carried out in atmospheric condition using so called contact or tapping modes.

SMENA-B instrument (NT-MDT) used to acquire AFM images of structured films and nanofibers. AFM was operated in the intermittent contact mode with NSG11 cantilevers (NT-MDT).

Transmission electron microscopy (Paper II)

Transmission Electron Microscopy (TEM) uses energetic electrons to provide morphologic, compositional and crystallographic information of samples. TEM produces a high-resolution, contrast image from the different transmission rates of the electrons through different regions of the samples. These differences provide information on the structure, texture, shape and size of the sample [219]. Samples for TEM analysis have to be thin or sliced to thin enough for electrons to pass through.

The geometric composition and surface structures of the needles were visualized using a transmission electron microscope Philips TECNAI 10. The needles were glued to metal washers, ensuring sufficient electrical contact for removal of surface charges due to the electron beam.

4. RESULTS AND DISCUSSION

4.1. Preparation and properties
of metal alkoxide based sols (Paper I)

Viscosity and rheological properties of metal alkoxide sols are the main parameters responsible for formation of the specific shape of oxide structures *via* sol-gel processes, especially in preparation of fibers. Viscosity of sol precursors in turn is affected by the particle size [220] and is known to increase upon agglomeration [91]. The viscous nature of neat alkoxides is notable as it distinguishes primary alkoxides (ethoxides, propoxides, butoxides, etc.) of metals (Ti, Zr, Hf, Sn, Ce, etc.) from their silicon analogues and from secondary and tertiary alkoxides of these metals, which have the viscosity lower by several orders of magnitude. As mentioned earlier, this property is explained by the extremely high acidity of metal alkoxides in the Lewis sense that facilitates self-agglomeration [79, 81].

In this work, polymerization-condensation processes of multiple metal alkoxides and the corresponding materials properties were investigated and characterized (see Table 1). $Sn(OBu)_4$ sol formation, inner structure and flow parameters relations with applied polymerization-condensation methods were investigated more thoroughly. To certain extent the results can be generalized to other metal alkoxides.

Table 1. Water/alkoxide molar ratios in the precursors used for fiber drawing. From Paper I.

Alkoxide	R
$Sn(OBu)_4$	0.5–0.8
$Sn(OPr)_4$	0.2–0.3 (decomp.)
$Ti(OBu)_4$	0.6–0.9
$Ti(OPr)_4$	0.5–0.8
$Zr(OBu)_4$	0.4–0.6
$Zr(OPr)_4$	0.4–0.6
$Hf(OBu)_4$	0.4–0.6
$Ce(OBu)_4$	0
$Ce(OPr)_4$	0

Aqueous (AQ) and non-aqueous (NAQ) methods were applied to prepare $Sn(OBu)_4$ based viscous precursor materials consisting of metal-oxo-alkoxide nanoclusters to investigate similarities and differences of both methods in respect to morphology and rheology of precursor materials. Temperature dependence of precursor consistence in the NAQ procedure was investigated by removing fractions of precursors at different temperatures from the reaction bulb and a mass loss curve was constructed to describe the decomposition of $Sn(OBu)_4 \cdot x$BuOH (Figure 27).
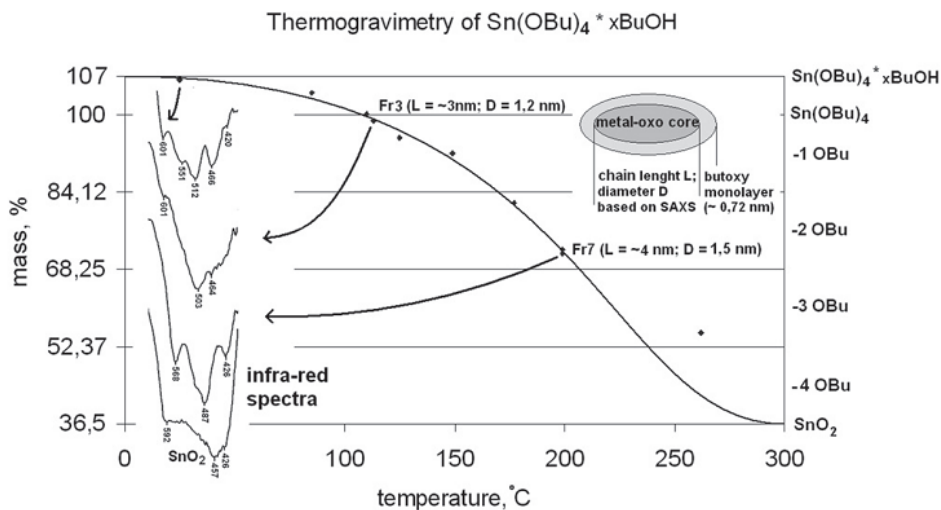
Figure 27. Thermogravimetry curves of Sn(OBu)$_4$. The evolution of the chemical structure during the measurement is indicated on the right Y-axis where -1 OBu, -2 OBu, etc., denote numbers of eliminated butoxy groups per Sn(OBu)$_4$. The starting point on the left Y-axis has been set at 107% because the sample contained 7 wt% of solvated butanol. The FTIR spectra show the range of the Sn–O-skeletal vibrations. The deviation of the final point (at ~270 °C) from the general trend could be explained by inhomogeneities due to the difficulty in stirring the highly viscous liquid. From Paper I.

Pure Sn(OBu)$_4$ is known to exist as a mixture of trimers and tetramers that form particles 0.9 nm in diameter and 2 nm in length [221, 222]. Our SAXS analysis revealed that the particles of Sn(OBu)$_4$-based samples have elongated shapes, with a mean length of 4 nm and mean diameter of 2 nm for both AQ ($R = 0.7$) and NAQ (at 200 °C) precursors. NAQ sample heat-treated up to 110 °C contained clusters up to 2 nm in length. Metal oxo-alkoxides are known to consist of nanospheres [79, 81, 222], and thus the elongated shape can be explained by the formation of secondary particles. Such behaviour of metal alkoxides is well known and could finally lead to the formation of a 3D solid network and gelation [79, 81].

XRD analysis did not detect any crystalline phases in the case of AQ-prepared precursors while NAQ sample analysis revealed the presence of cassiterite crystalline structure. To verify the presence of cassiterite and estimate its crystallite size, a simulation based on Debye function was compared with the experimental data and the best agreement was achieved for 1 nm particles (Figure 28). This result agrees well with the outer shape of Sn(OBu)$_4$ particles deduced from the SAXS analysis. The elongated particles detected by SAXS probably consist of two to four spherical particles merged in one direction. The internal structure of the primary spherical particles has some short-range order that corresponds to the structure of cassiterite. Crystallization of SnO$_2$ nanoparticles during the NAQ treatment could be explained by the

60

tendency of metal oxides to self-crystallize, which in many cases could occur even at room temperature because of the low enthalpy of crystallization [223].
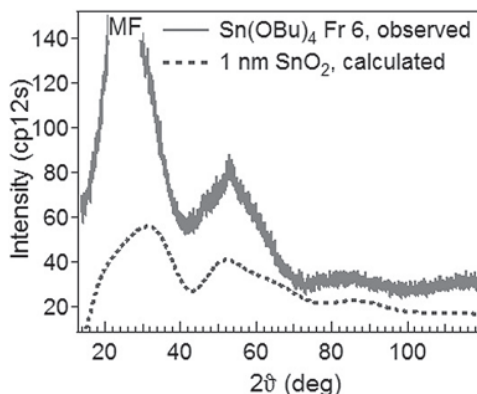

Figure 28. Observed XRD pattern (solid curve) from the NAQ $Sn(OBu)_4$ precursor (at 175 °C) and a pattern calculated with the Debye function (dotted curve) for a spherical 1 nm SnO_2 (cassiterite) particle. The difference at angles below 40° is caused by a strong contribution from Mylar foil. From Paper I.

Concluding results from the FTIR, SAXS and thermogravimetry analysis of NAQ precursor analysis are shown in Figure 27. The thermogravimetry curve of $Sn(OBu)_4$ that is based on the solid content analysis of each fraction fits well to the earlier data [203]. Sn–O stretching vibrations signal from NAQ precursors showed characteristic changes in the range of 400–600 cm^{-1}, proving the evolution of well-defined alkoxide structure with increasing temperature until formation of SnO_2. The sharp FTIR peaks belong to trimeric or tetrameric butoxy clusters of pure $Sn(OBu)_4$ having well-defined inter- and intramolecular structures [224]. The transformation of these peaks into a broad band in the first stages of heating at temperatures up to 130 °C could be explained by the release of solvated butanol, which vacated the coordination sites of Sn. Formation of new intermolecular bonds results in an irregular structure corresponding to the broad band; these stronger intermolecular forces also increase the viscosity. The viscosity decreases again upon heating to 150 °C and above. The appearance of clearly distinguishable FTIR peaks in this temperature range reveal the formation of another well-ordered structure, and the similarity of the peak positions in the region of Sn–O vibrations for the fractions 5–7 and SnO_2 suggests that this structure is based on metal oxide. This observation is supported by the XRD measurements that identify the cassiterite structure. The decreased coordination number leads to a lower viscosity as a result of the diminished ability to form intermolecular bonds.

Sn(OBu)₄ AQ-prepared precursors viscosity dependence on water/alkoxide mole ratio can be seen in Figure 29. Viscosities were determined using Stokes method. The viscosities of other alkoxide systems in this study followed the

same basic tendency, with the exception of cerium alkoxides which already have syrup-like viscosity without any additional polymerization-condensation processes. Another exception is $Sn(OPr)_4$, which is slowly decomposing already at the room temperature. The nearly exponential growth of viscosity with R could be related to the increase of the particle size [221].
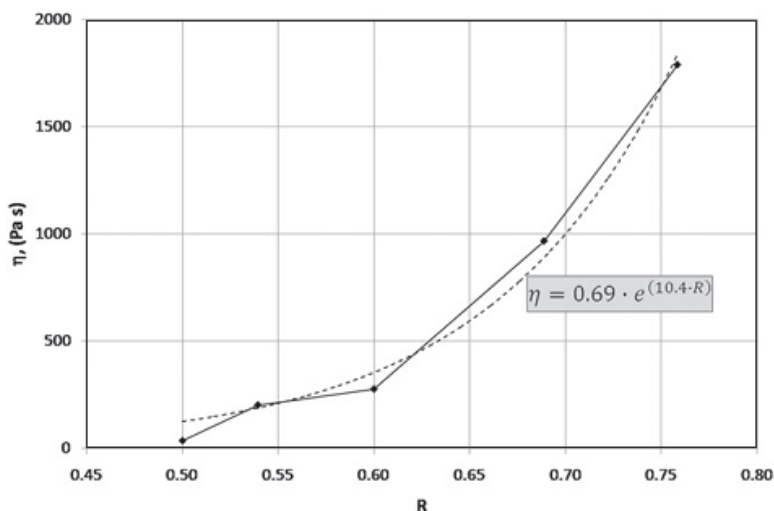

Figure 29. Dependence of the viscosity η of $Sn(OBu)_4$ AQ concentrates on the water/alkoxide mole ratio R. From Paper I.

Precursors spinnability can be confirmed empirically by immersing a tip of a glass rod into the sample and drawing up the rod. If a long, continuous fiber can be drawn, the spinnability is "Good" and judgement is "Yes". If no fiber can be drawn, we judge "No". "Poor" means only short fibers can be drawn [69]. Suitable R-values (water/alkoxide mole ratio) for studied alkoxide systems are presented in Table 1, however, the concentrates of $Ce(OR)_4$ were spinnable as prepared. Spinnability was achieved after concentrating the obtained solutions in vacuum.

After the initial spinnability evaluation more detailed rheological studies were carried out for AQ (mole ratio $R = 0.7$) and NAQ-treated (treated up to 170 °C) products of $Sn(OBu)_4$. Those particular samples of tin butoxide sol were selected as they showed the best spinnability and materials rheological properties are considered to be most interesting and more revealing in that region.

Several mathematical models have been developed to describe the relationship between shear stress and shear rate of non-Newtonian fluids. These models are used to characterize flow properties to determine the ability of a fluid to perform specific functions [225]. As shown in Figure 30, the shear stress–strain curves show a Bingham pseudoplastic behaviour of pronounced

yield stress σ_y for the condensed liquids. The values of the parameters in the Bingham model ($\sigma = \sigma_y + \eta\,\dot{\gamma}$) were measured for the shear rates from 0.1 to 50 s^{-1} and are listed in Table 2.
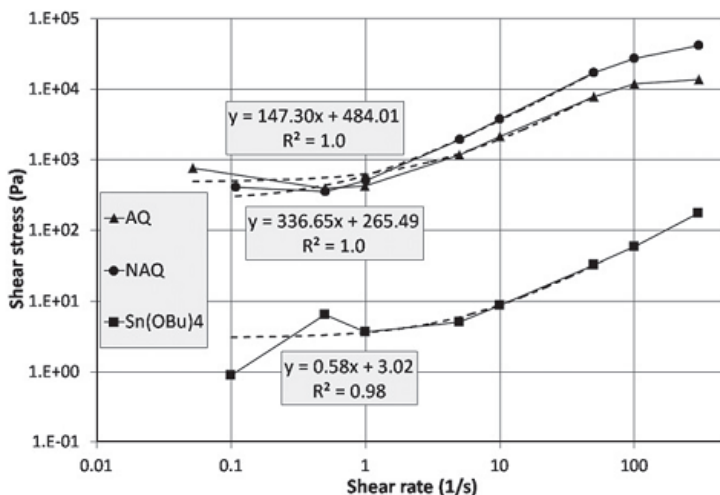

Figure 30. Shear stress versus shear rate for Sn(OBu)$_4$ systems. Dashed lines show the fit by the Bingham model. From Paper I.

Table 2. Bingham model parameters for the Sn(OBu)$_4$ systems. From Paper I.

Sample	η (Pa s)	σ_y (Pa)
Sn(OBu)$_4$	0.58	3.02
AQ-treated	147.3	484.01
NAQ-treated	336.65	265.49

As seen from viscosity versus shear rate plot (Figure 31), as-prepared Sn(OBu)$_4$ experience a pronounced zero-shear plateau and shear thinning effect. AQ and NAQ treated samples have also shear thinning region but their viscosities are higher.

Viscosity values of 0.58, 121 and 273 Pa s for as-synthesized, AQ and NAQ polymerized Sn(OBu)$_4$ were obtained at shear rates of 100 s^{-1}. The viscosities were two times higher for NAQ-processed than AQ-processed samples at high shear rates, while the shear thinning behaviour was more pronounced for the AQ samples.
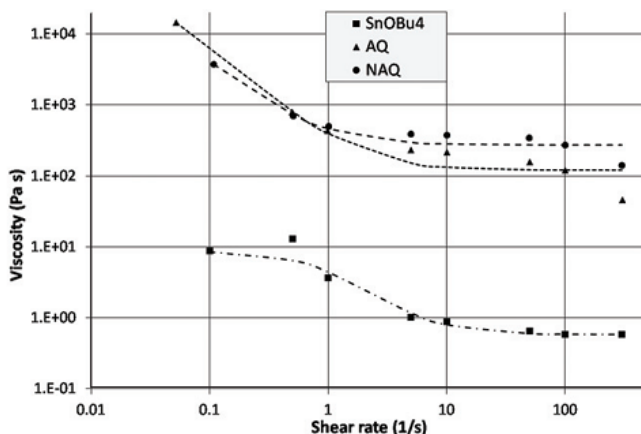
Figure 31. Viscosity of Sn(OBu)$_4$ systems plotted versus the shear rate. From Paper I.

Schematic explanation of the viscosity dependence on the shear rate is presented in Figure 32. We suggest that the as-synthesized, AQ or NAQ-treated Sn(OBu)$_4$ exhibit a typical behaviour of non-Newtonian liquids. For all measured liquids the apparent viscosity decreases with the shearing rate, which is typical for polymeric liquids and can be explained by the alignment and sliding of elongated particles under applied stress (Figure 31).

a)   b)

shear rate < 1 s^{-1} (low pulling speed),   shear rate > 10 s^{-1} (high pulling speed),
gel-like behavior   liquid behavior
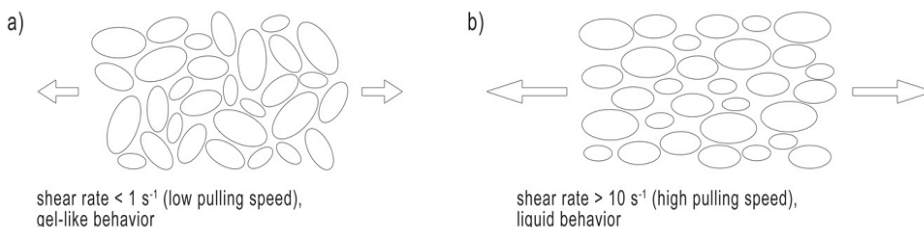
Figure 32. Alignment of elongated particles by external forces. From Paper I.

Oscillatory measurements of viscous and elastic properties were performed to characterize the rheological state of the alkoxide systems. Firstly, the storage modulus G' (materials elastic response) was measured to determine the linear viscoelastic region where the inner structure of a liquid remains intact. Figure 33 shows that NAQ-treated Sn(OBu)$_4$ has the widest linear viscoelastic region. Breakdown of the network occurs at the strain amplitude higher than 2%. Initial and AQ-treated Sn(OBu)$_4$ have roughly the same linear viscoelastic region of the stable network up to 0.2% strain amplitude.

Figure 33. Determination of the linear viscoelastic limit for $Sn(OBu)_4$ systems: dependence of the storage modulus G' on strain amplitude Y at a frequency of 10 rad s^{-1}. From Paper I.
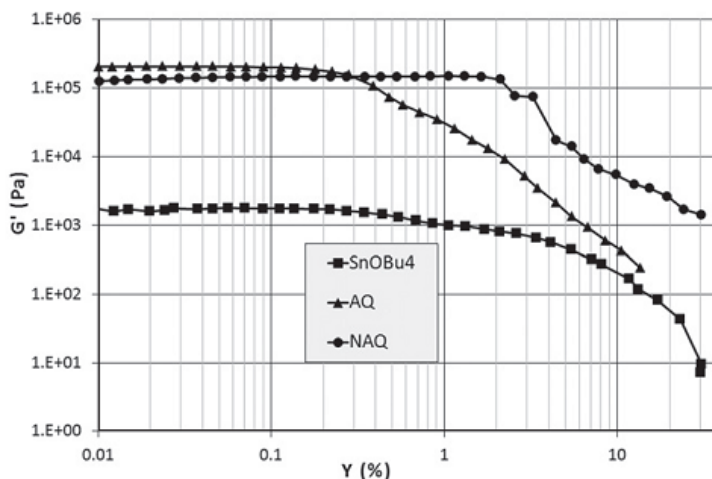
Frequency sweep results for the neat, AQ-treated and NAQ-treated tin butoxide systems at a strain amplitude of 0.1% (within the linear viscoelastic region) indicated to a predominantly elastic behavior of the materials. It was also concluded that compared to AQ precursors, NAQ treated $Sn(OBu)_4$ inter-molecular cross-links are stronger [226] and particle weight is larger at similar particle weight distributions.

Surface tension also affects formation of structures from viscous metal alkoxide concentrates and therefore the surface tension coefficients were measured for the studied liquids as described in chapter 3.2. The initial, AQ and NAQ-prepared $Sn(OBu)_4$ samples had the corresponding values at 26.6, 32.7 and 18.0 mN m^{-1}. The higher value for the AQ-treated samples can be explained by stronger intermolecular forces in their precursors. Note that the rheology analysis indicated higher elasticity for the NAQ-prepared precursors. Thus the surface tension measurements suggest different properties at the surface and in the bulk of the liquid phase, probably due to the contact with the atmosphere saturated with alcohol vapours. We suggest that the strength of the forces between the precursor particles depends mostly on the nature of their oxide cores. Sn centers at the surface of denser NAQ particles are better stabilized; therefore, they are less acidic in the Lewis sense and less readily form the intermolecular bonds.

4.2. External parameters influence on formation of shapes from metal alkoxide sols (Paper II)

Besides viscosity, other parameters affecting structure formation from viscous sols are water content in the surrounding atmosphere where the shaping is conducted and the shear rate used to shape the viscous material. The influence of relative humidity (RH) was studied on the formation of needles using a 55 Pa s viscosity precursor. The RH was found to have relatively strong impact on the shapes of the needles. At 80% and higher RH only irregular needles were formed while below 80% RH mostly regular cones were formed. At 2–4% RH also only regular cones were formed. We compared the results with Eggers' theory that models the disintegration of liquid jets [227]. The theory relates the minimal possible diameter of a filament, D_{min}, to the material's intrinsic parameters (surface tension and viscosity):

$$D_{min} = 0.0304 \frac{\gamma}{\eta}(t_0 - t) \tag{14}$$

where γ is the surface tension of the liquid, η is the dynamic coefficient of viscosity, t is time and t_0 the moment of the pinch-off. According to this equation the pulling speed does not affect the shape of the forming filaments. However, in the case of our alkoxide materials there was a clear dependence between the cone angles of the formed needles and the pulling speed (Figure 34).
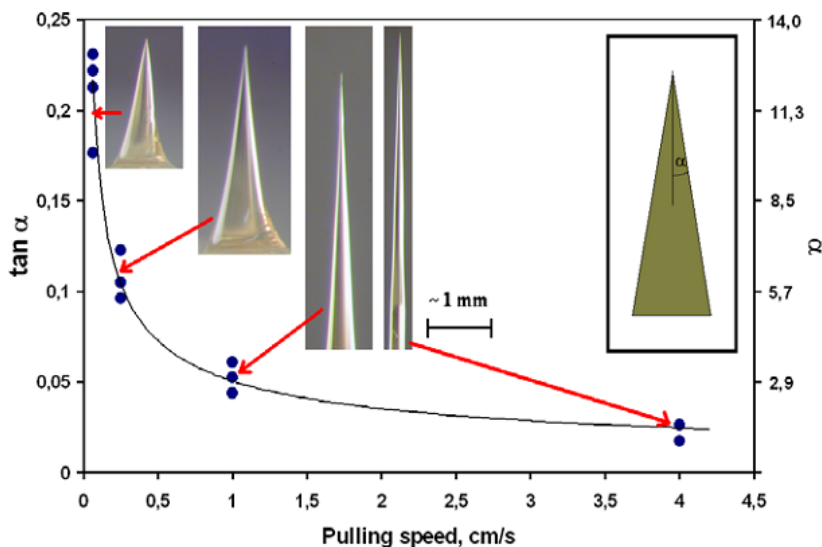

Figure 34. Cone angles of the needles versus pulling speed. The precursor's viscosity was 55 Pa s and RH was 2–4%. Each point means one experimental sample. From Paper II.

We can derive the following empirical relation, which holds at least in the measurement range:

$$\tan\alpha = \frac{C}{\sqrt{\upsilon_p}}$$ (15)

where α is the cone angle of the tip, υ_p is the pulling speed and C is an empirical coefficient. Such a relation most likely originated from the polymerization-condensation processes initiated by air humidity, leading to increasing viscosity during fiber formation. Thus, at viscosities below the gelation point [228] the alkoxide needles form regular cones, whose angles are determined by the pulling speed.

At 20–30% RH regular shaped cones were more likely than irregular shaped cones. Formation of irregular shaped needles at 80–95% RH-s can be explained by the increase of surface viscosity beyond the gelation point before pinching due to quicker polymerization of the material.

When the precursors viscosities are 0.1–10 Pa s and the pulling speed is very low (in our experiment 37.5 μm s^{-1}) so called *earthworm*-shaped filaments are formed, which do not converge conically (Figure 35). We argue that in this parameter range the stretching speed was much slower than the surface gelation, leading to a two-step process rather than continuous formation of fibers. The system resembles a solid tube filled with a low viscosity liquid (Figure 35). Thus, when stretching it a series of crackings–regelations occur, resulting in formation of an *earthworm* shaped filament. All those kinds of filaments were wrecked during ageing in air, which was because of the bulkiness and non-uniformity of these structures.
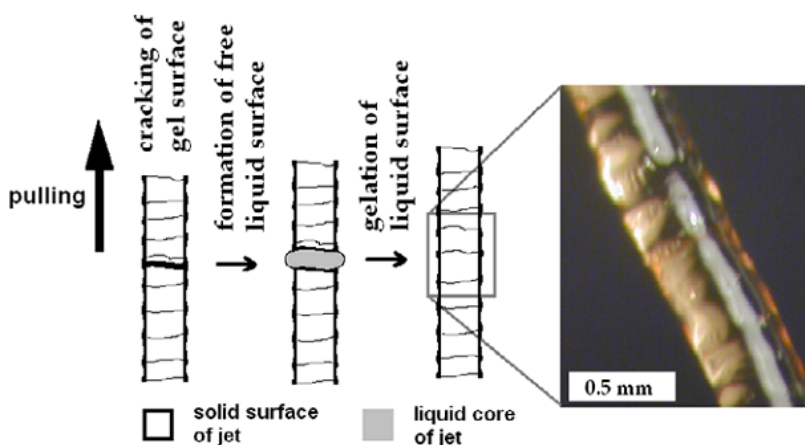

Figure 35. Schematic illustration of the mechanism that causes formation of non-uniform (earthworm) fibers. The photograph shows a fresh fiber pulled from 7 Pa s precursors applying 37.5 μm s^{-1} linear pulling motion at 30% RH of surrounding atmosphere. From Paper II.

4.3. CNT influence on metal alkoxide based sols rheological parameters (Paper III)

Method for producing metal-oxo-alkoxide/CNT suspensions is described in chapter 3.1. The CNTs effect on metal alkoxide based sols rheological behaviour was studied with extensional rheometry by using specially constructed device, described in chapter 3.2.

For calculation of rheological parameters from evolution of a filament minimum diameter, two types of approximations of the experimental data were applied [229]. From the approach for initial and intermediate stages of evolution, which reflects visco-elastic regime, the steady-state extensional viscosity $\eta_{E\infty}$ and the longest relaxation time λ_E of liquid were calculated. At the final stage of filament evolution just before break-up, the inner structure of liquid becomes aligned and extremely elongated and the filament diameter change in time is similar to Newtonian liquids. The approximation of this stage allows obtaining zero shear viscosity η_s of a liquid with a specific inner structure such as aligned CNTs and precursor particles [230]. The measurements were carried out for a pure liquid as well as for the liquids with CNTs concentration of 0.01, 0.02, 0.05 and 0.1 mass%.

Extensional viscosity measurements confirmed the results of rotational rheometry (chapter 4.1.), that initially pure precursors are weakly strain-hardening viscoelastic liquids. Measurements with precursors containing CNTs showed that the dispersion of small amount of CNTs in the titanium(IV)-propoxide (Ti(OPr)$_4$) dramatically decrease the time of a filament break-up. Change in filament break-up time dependence on CNTs concentration could be explained by clumps (CNT aggregates and bundles) formation due to unreliable dispersion of CNTs as the similar results were reported for the epoxy resin reinforced by carbon nanotubes [201]. However, the surfaces of the produced filaments in current study were smooth at all concentrations of CNTs and evolution of the minimal filament diameter with time passed gradually without significant heterogeneities. This points to the fact that the decrease of filament break-up time is not related to the clumps formation because of poor dispersion of CNTs.

The effect of CNT concentration on the rheological parameters is shown in Figure 36. It should be mentioned that the values of zero shear viscosity correspond to the shear viscosity of a liquid with preliminary aligned CNTs and precursor particles. Extensional and zero shear viscosities have the same tendency: a small increase in the case of concentrations equal to 0.01% and strong decrease (by several times) in the CNT concentration up to 0.05%. For larger concentrations (0.1%) of CNTs the parameters do not change significantly. The relaxation time decreases with increasing CNTs content.
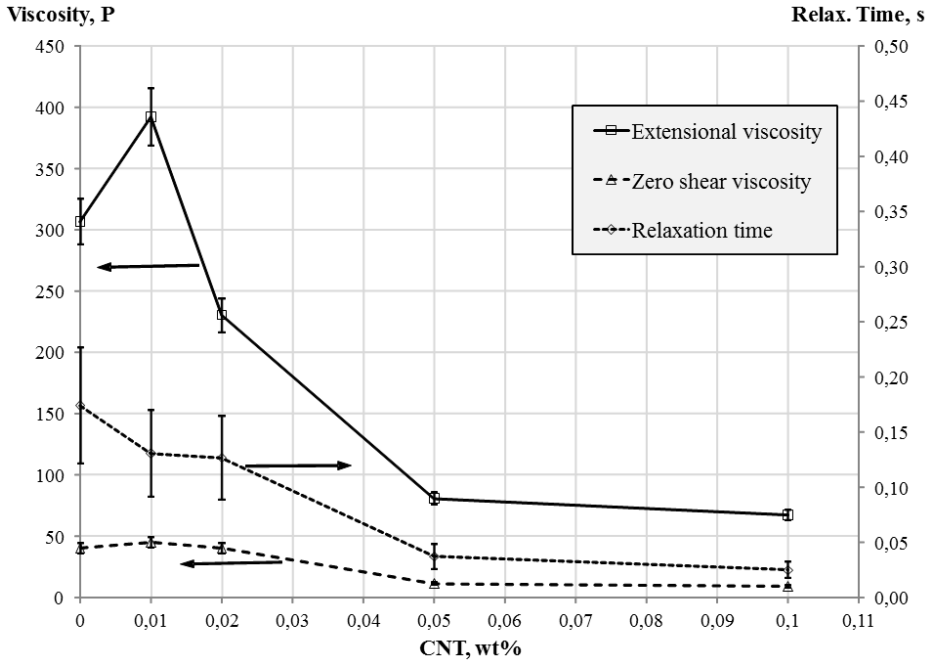
Figure 36. The rheological parameters (steady-state extensional viscosity $\eta_{E\infty}$, zero shear viscosity η_s and longest relaxation time λ_E) as a function of CNT concentration. From Paper III.

Decrease in viscosity and relaxation time for suspensions filled with nanoparticles may be observed under definite conditions, for example, when the filler particles are smaller than a radius of gyration [231, 188]. In our case this condition is not held because, as demonstrated in chapter 4.1., the liquid particle size was ~2 nm while CNT diameter was 10–20 nm. CNT influence on rheological parameters could be explained by fluid layers on the particle surface. As demonstrated by Wang *et al.* [232], the parameters responsible for viscosity variations are stated to be an adsorbed layer thickness, its viscosity, and slipping at the particle surface. The hydrodynamic model of a liquid layer at the nanoparticle–liquid interface has indicated that the viscosity and density of the layer differ from that of the bulk liquid. When the layer thickness is larger than the nanoparticle radius and the layer viscosity is lower than that of the bulk liquid, the viscosity of the fluid can be dramatically reduced [232]. Chemical structure of the sol-gel precursors and its interaction with CNTs lead to a reduced viscosity in the fluid layers on the particle surface. The latter effect in turn increases fluidity of the mixture, revealed as the decrease of a bulk viscosity.

4.4. Preparation of structures (shapes) from viscous metal alkoxide based sols (Papers I–VIII)

The aim of this chapter is to introduce the possibilities to obtain structures with various shapes from precursors with different viscosities.

Preparation and characterization of fibers

Using suitable *R*-values, it was possible to draw fibers with both methods described in chapter 3.3. The first method – direct drawing from dry to humid atmosphere from a flask – allows to pull fibers one by one, from all AQ precursors for the *R*-values listed in Table 1, and from the NAQ fractions 4–7 of Sn(OBu)$_4$ concentrates (Figure 27). Obtained fibers have a typical length of 10–50 cm and a diameter of 1–50 μm depending on the amount of material used for the drawing. Microscopic images of the fibers are shown in Figure 37. The second method, i.e. pulling in humid atmosphere, typically results in a simultaneous formation of 10–100 fibers of different diameters. Because of the spread in the initial amount of material the fiber diameters vary widely, from 200 nm to 10 μm. The minimum diameter is typically 500 nm for the AQ-treated samples and 200 nm for the NAQ fractions 4 and 5. Fibers with more uniform diameters are obtained from NAQ precursors. The respective aspect ratios are usually 1000 and 10 000 for the AQ and NAQ precursors, respectively. The better performance of the NAQ precursors could be explained by their higher elasticity compared to the AQ precursors. The smaller minimum diameter relates to the lower surface tension of the NAQ precursors, which also lead to the break-up of the jets. Another reason is the higher chemical stability of the NAQ precursors that allows prolonged fiber drawing in air before the onset of solidification. In good agreement with Sakka *et. al.* [146], the cross-section of our fibers is always strictly circular owing to the use of highly concentrated precursors. AFM imaging over a 5 μm distance along the fiber axis revealed a surface roughness of 1–2 nm or less, that is at the atomic level (Figure 37).

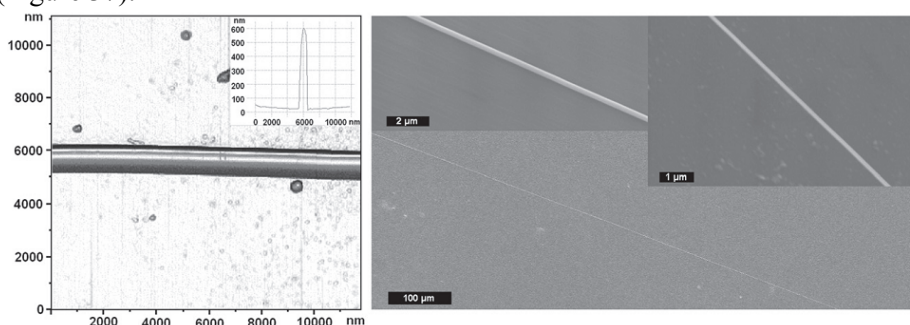**Figure 37.** AFM (left) and SEM (right) images of SnO$_2$ fibers obtained from NAQ-treated Sn(OBu)$_4$ precursors. The inset of the left image shows an AFM line profile of a fiber resting on the substrate. Images are taken after heat treatment. From Paper I.

It was possible to densify the structure and to burn out organic components from all the studied materials. The fibers did not crack during the heating even when they were thinner than a few microns and were supported by a solid substrate. These results open future perspectives of direct drawing of metal oxide fibers for integrated optoelectronic devices.

Preparation and characterization of needles

The viscous jet pinching process is mainly affected by precursor's viscosity, atmospheric humidity and the pulling speed of the jet. At room temperature with 20–30% relative humidity, the viscosity range between 30 Pa s and 150 Pa s was suitable for pulling the needles. Within this range the viscosity values had very little impact on the shapes of the needles. Note that relatively simple and slowly varying relations between flow parameters (e.g. viscosity) and intrinsic parameters (e.g. molecular mass M) were expected within the investigated range because the mass range of 1000–3000 amu [233] remained considerably below the typical entanglement molecular weight Me ($M<Me$) [220, 234] and above which correlative motion effects appear and the material usually transforms into being unspinnable [228].

From the TEM images it can be seen that obtained needles are nanometrically sharp having typically tip curvature radii of 15–25 nm (Figure 38a). The cross-sections of the needles is perfectly round (Figure 38b, inset), which can be considered as a valuable characteristic in optical applications [235–237]. The shape of the needles was observed to resemble those that had been pulled from silica melts [236], which could be explained by similar flow
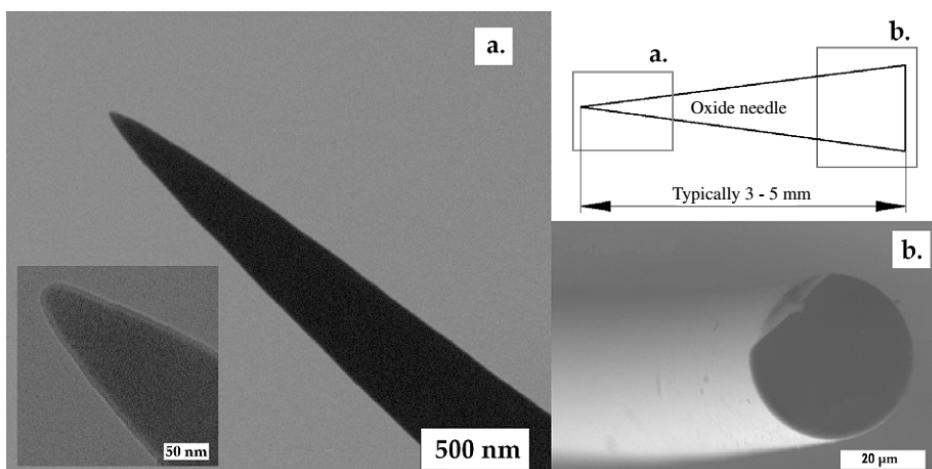

Figure 38. Electron microscopy images of typical sol-gel needles from metal alkoxides. From Paper II.

properties and solidification kinetics in both cases. Generally, the post treatment of gel bulks decreases equally in all dimensions, having little impact on the shape of the body [146]. During ageing most of the alkoxy groups in gel material turn to -OH groups or -O- bridges, as a result of reaction with water [105]. Both ageing and baking cause the material to shrink up to 50% because of densification and crystallization, and the release of organic residues.

Preparation and characterization of structured films

The sols used for tape casting had viscosities approximately 24 Pa s. Realization of desired structures demands careful optimization of many technological parameters. In our device (described in chapter 3.3.) we can control shape and material of the blade, pressure on the blade and angle between the blade and the substrate, as well as the speed of the substrate relative to the blade. Also sols viscosity and humidity of surrounding environment can be controllably varied. The sample shown in Figure 39 and Figure 40 was prepared at room temperature at relative humidity 20%, using relative speed of the blade 1 mm/s, which are typical values applied in our method. The method was tested in gaseous environments with different humidity. It was found that normal air humidity of our laboratory (20±5%) was well suited for tape casting of linear structures. Humidity of the environment affects the speed of gelation process and existence of water vapour in the environment is absolutely necessary, since water molecules take part in gelation process.
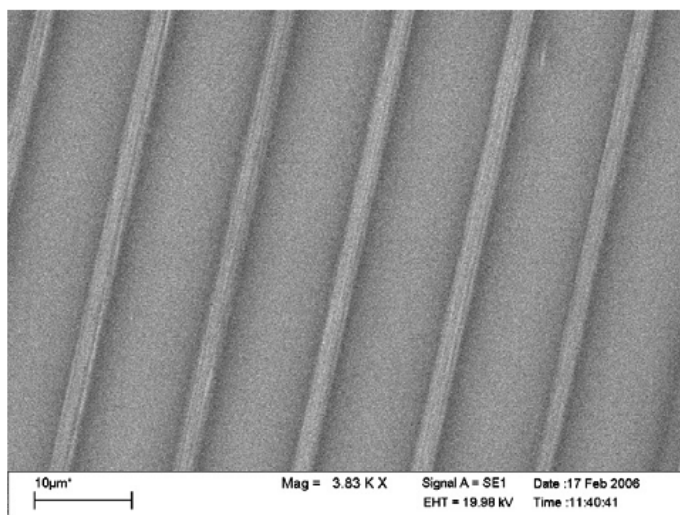

Figure 39. Image of tape casted microstructure film obtained by SEM. Approximate length-scale is depicted in the figure. From Paper IV.

Figure 39 shows SEM image of a typical casted microstructured film and Figure 40 demonstrates three-dimensional AFM image of the same microstructured sample measured in tapping mode. In the present study, the focus was set on the creation of linear structures and therefore structures were prepared explicitly without additional sol-gel layer underneath the structures. Absence of additional sol-gel material between structures and substrate was verified using AFM imaging and optical microscopy.
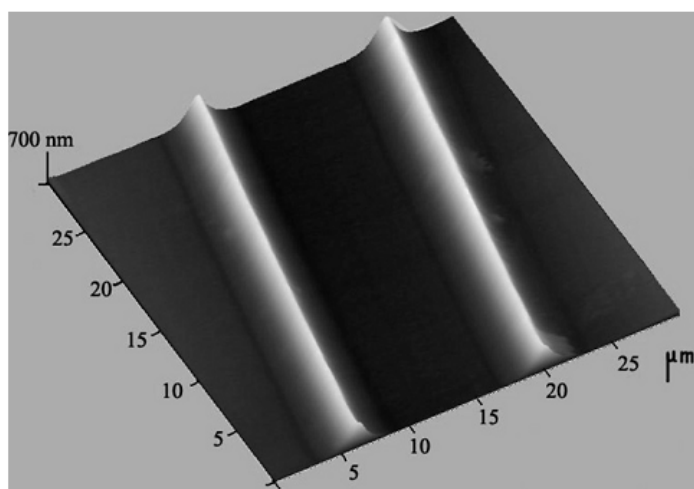
Figure 40. AFM 3D image of tape casted microstructure film (period approximately 14 μm). From Paper IV.

Figure 39 and Figure 40 clearly demonstrate that tape casting method can successfully be applied for production of well-defined linear structures. The overall resemblance of formed structures to the blade is good, e.g. the structures periodicity is very close to the blades one. It means that horizontal shrinkage of the structures during gelation process is almost negligible, since formed structures are strongly connected with the substrate. Note however, that in the shown example, the shape of a groove is not identical replica of the blades structure and the shrinkage of the structures in vertical direction during the gelation process is up to four times. Although the replication quality can be greatly improved by using higher viscosity sols, the cracks appearance due to different forces acting during the gelation process becomes significant when such large structures are formed.

Preparation and characterization of powders
Using any of the above mentioned methods it is also possible to produce oxide powders. In fact, oxide powders are often a "side products" as a result of a cracked films or fibers. Grinding can be used to optimize the size of the powder particles.

4.5. Sol-gel prepared CNT-ceramic composites properties (Papers III, VI–VIII)

In the current study we describe sol-gel preparation of CNT-reinforced TiO_2 fibers and their characterization in terms of optical, electrical and mechanical properties. TiO_2 was chosen as a matrix because it is one of the most well-known metal oxide ceramic materials that has broad applicability due to its good mechanical properties, high corrosion resistance, photocatalytic properties and chemical stability [238]. Similarly prepared precursors from alkoxides of other metals such as tin, hafnium and zirconium could also be prepared to obtain variously structured (thin films, structured films, fibers, etc.) transition metal oxide/CNT composites.

Composite fibers were prepared by pulling jets from CNT-alkoxide concentrates. Obtained fibers diameters depend on the visco-elasticity of material, applied pulling speed, humidity of the surrounding air and nanotube aggregates remained in the matrix after sonication. Although numerous CNT functionalization procedures to improve solubility of CNT-s in different mediums can be found in literature [55], in the present work pristine MWCNTs were used due to their higher mechanical stability and electrical conductance.

Annealing of sol-gel materials is generally used to oxidize amorphous organic remnants and to densify the resulting structures [69]. Additionally, the prepared sol-gel amorphous materials can be crystallized at elevated temperatures [239]. At the same time, thermal stability of pristine MWCNTs in the composite materials is known to depend strongly on processing parameters [21]. The heat treatment series was carried out to determine a temperature where materials maximum crystallinity is achieved while carbon nanotubes physical attributes are still preserved. As seen from Figure 41, electrical conductivity of TiO_2 fibers with 1% MWCNTs was decreased by several orders of magnitude when heated up to 500 °C, indicating that CNT are burned out from the oxide matrix.
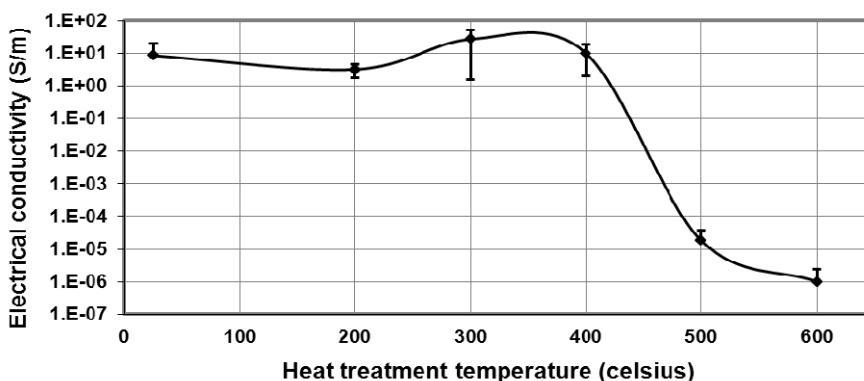

Figure 41. Electrical conductivity of 1% MWCNT doped titanium dioxide fibers heat treated at different temperatures.

Besides thermal oxidation, the processes that could decrease carbon nanotube physical properties in the final composite structures include sonication, functionalization and mixing [58]. Sonication is usually known to break bigger CNTs clusters and bundles into smaller bundles, MWCNT ropes or single MWCNTs [56]. Preliminary SEM analysis revealed that CNT-oxide fibers surfaces were generally smooth although individual irregularities could be seen on fibers with higher CNT concentrations. These surface irregularities are probably caused by small CNT ropes and bundles. Imaging of the area cut by using FIB proved clearly that most of tubes in the material were dispersed into single tubes, ropes or very small bundles (Figure 42).
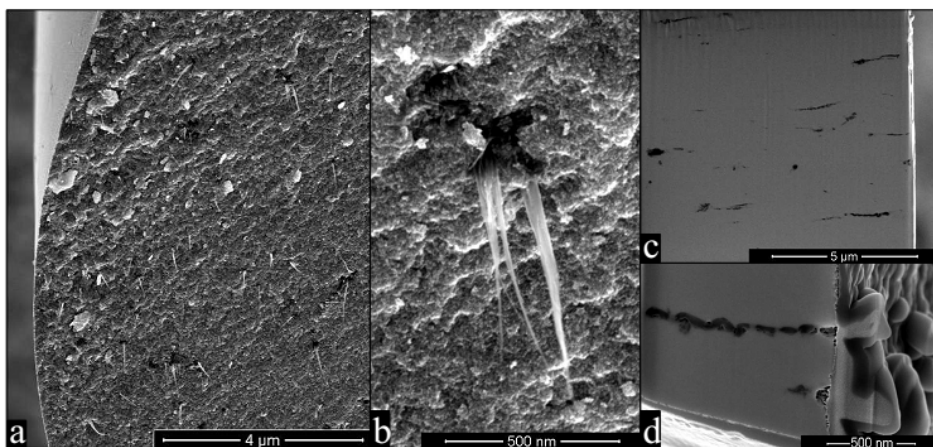
Figure 42. In order to image the cross-section, by using scanning electron microscopy (SEM) and focused ion beam analysis (FIB), the fibers were mechanically broken prior to imaging. SEM image of CNT doped oxide fibers cross-section (a). Although CNT-s disperse well in oxide matrix, some still remain arranged into "ropes" (b). FIB analysis proved that CNT-s are oriented along the fiber axis (c, d). From Paper VII.

Emerging of a CNT percolation network with increasing CNT concentrations can be visually followed in the series of composite materials with 0.01; 0.02; 0.05; 0.1 and 1 mass % of CNTs (Figure 43). At 0.05 mass % and below, CNTs remained scattered in matrix while in the fibers with 0.1 mass % of CNTs, areas with percolating networks could be seen. When 1 mass % of CNTs were inserted into titanium dioxide matrix, the CNT percolation was sufficient for electrical conductivity detection on the composite material. The conductivity of the samples containing 1% of CNTs and heat treated up to 400 °C was in the range of 50 S/m while the conductivity of the fibers containing 0.1 mass % of CNTs remained below detection limit of the used equipment. When the fibers containing 1% of CNTs were heat treated up to 600 °C, the resistance decreased down to 10^{-6} S/m. The CNT percolation threshold between 0.1 and 1 mass % indicates that the current CNT dispersion method is very effective. For com-

parison, the carbon nanotube network formation in polymer based composites take place when CNT concentrations are between 0.5 and 10 mass% [240].
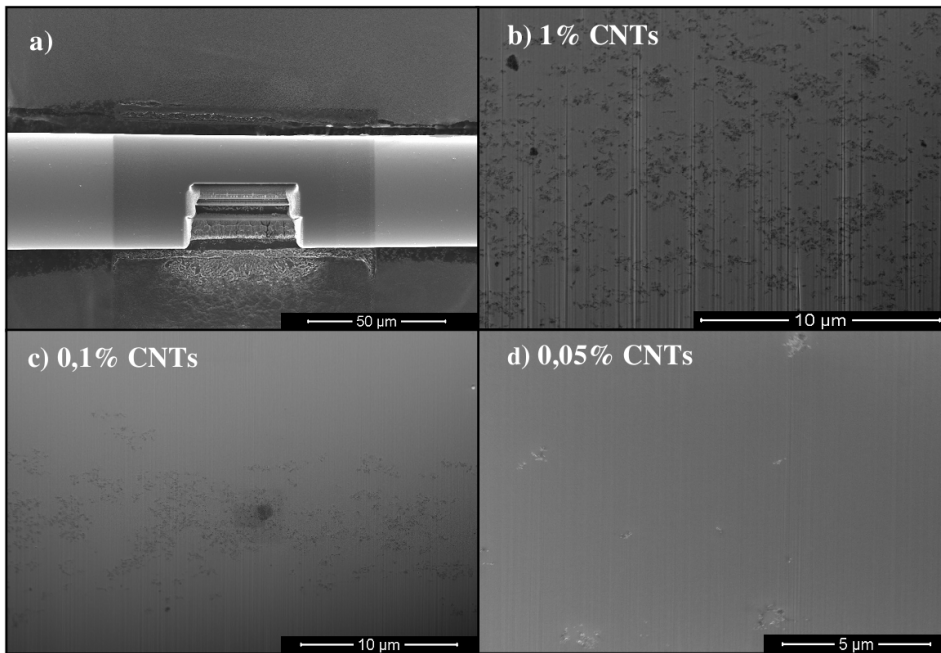
Figure 43. Scanning electron microscope (SEM) images of (a) focused ion beam (FIB) prepared fiber for CNTs imaging inside the material; (b–c) MWCNTs distribution in material with different concentrations. 0.01% and 0.02% CNT-composite fiber nanotube distribution was similar to the 0.05%. From Paper III.

It can be seen from the Figure 42c-d and Figure 44 that during the pulling process, CNTs are oriented along the direction of the fiber axis by elongational forces. Also it seems from the SEM-FIB analysis that big "loose" bundles are stretched out in the direction of pulling and that matrix material solidifying via formation of −O− bridges between metal-oxo nanoparticles prohibits CNTs to lose achieved orientation (Figure 41b-c). Although in the current study mechanical properties of the composites were not measured, it is known from the experiments with polymer/CNT fibers that the orientation of the carbon nanotubes can enhance overall mechanical strength of the material [241].
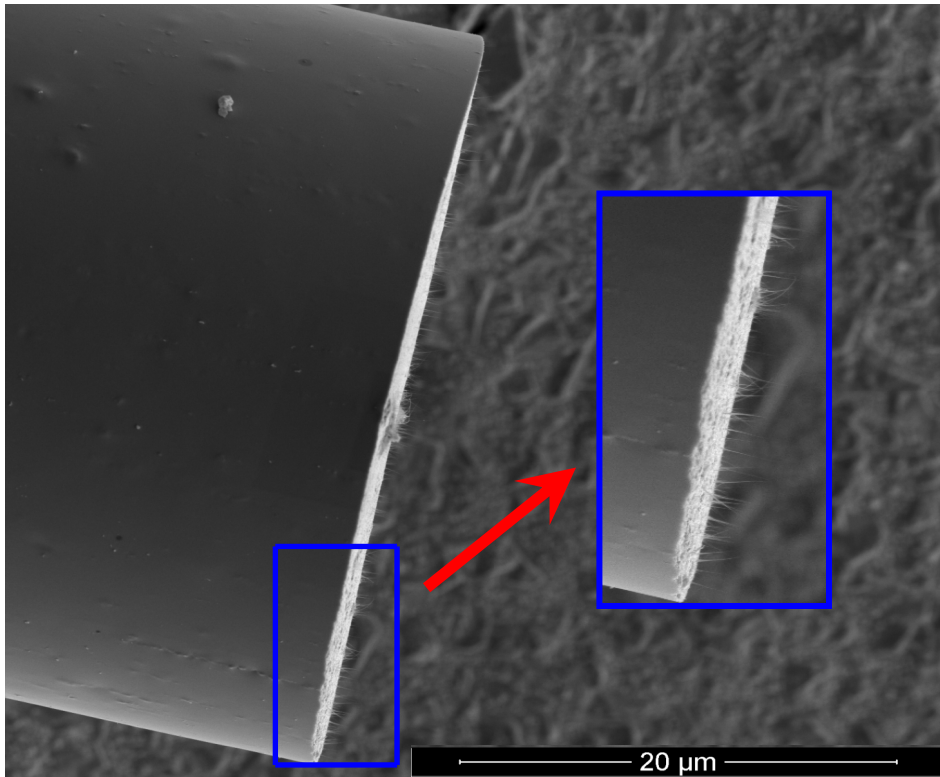
Figure 44. SEM images of a CNT-doped oxide fiber. The fiber was mechanically broken prior to imaging in order to reveal the doped CNT-s. It can be seen that CNT-s are oriented along the axis of the fiber. From Paper VIII.

5. MAIN RESULTS AND CONCLUSIONS

Integration of two naturally very different classes of materials to bring out their best properties, while "cancelling" their worst ones, to make a better material is one of the main challenges of modern material science. The thesis deals with the synthesis and characterization of composite material based on metal oxides and carbon nanotubes. The goal of this dissertation was to study formation mechanisms of oxide nano- and microstructures from metal alkoxides by sol-gel methods, and to search for ways to increase their electrical properties by doping with carbon nanotubes. Besides conventional techniques, peculiarity of the investigated system forced to develop new methods for shaping and characterization of precursors and final oxide materials.

Viscosity and rheological properties of metal alkoxide sols are the main parameters responsible for formation of the specific shape of oxide structures *via* sol-gel processes. Sol precursors viscosity in turn is affected by the sol particle size, in this study evaluated by SAXS analysis to be approximately 4 nm in length and 2 nm in diameter. XRD measurements revealed that the sol particles in NAQ samples consisted of 1 nm cassiterite particles whereas the particles of AQ samples were amorphous. Multiple metal alkoxides polymerization-condensation processes and the corresponding materials properties were investigated and characterized. The best spinnabiliy conditions, i.e. material ability to form liquid thread, were also determined for different metal alkoxides.

Rheological tests proved that the metal alkoxide precursors behave as typical non-Newtonian fluids. The observed shear thinning flow behaviour was explained by the formation of linear supramolecular aggregates in the material, which slide under external stress similarly to polymer particles in shear thinning systems. Rheological studies of precursor doped with carbon nanotubes demonstrated unusual decreasing of elongational viscosity and relaxation time with increase in CNTs content at low concentrations (less than 0.1wt%).

During this Ph. D. study, metal oxide fibers with a high aspect ratio of up to 10 000 have been drawn from different concentrated metal alkoxide precursors. The fiber diameter could be as small as 200 nm, reaching the limit for polymer systems. The best fiber drawing performance, including the highest uniformity and smallest diameter, was achieved for the NAQ precursors and attributed to their higher elasticity compared to the conventional AQ precursors. The preparation of thinner fibers is also promoted by the lower surface tension and higher chemical stability of the NAQ precursors, so that fibers can be drawn for a longer time in air before solidification occurs.

The pinching-off of alkoxide based jets in air was demonstrated as a reproducible route for preparing novel structures – nanometer level sharp oxide needles. Electron microscopy images demonstrated good quality and 15–25 nm sharpness of the needles. The results suggest that polymerization-condensation of pinched jets is notably quicker than surface tension caused drop formation at

the apex of the tip. The conical shape of needles correlates the profiles measured earlier with sharp fibers pulled from silica melts.

It was shown that the modified tape casting can be used to prepare either smooth and/or linearly structured sol-gel films from high-viscosity sol. The process is very different compared to existing sol-gel coating methods which use low viscosity sols. It is possible to prepare tape casted sol-gel films with thicknesses up to some microns. Also, the adapted method is applicable to large areas of substrate and to cover only one side of substrate (in contrast to widely used dip-coating).

Pristine CNTs without further functionalization were introduced into metal alkoxide and SEM and FIB analysis revealed that the overall dispersion of CNTs inside the final oxide material was good. Furthermore, from the SEM-FIB images it was evident that pulling concentrated alkoxide/CNT viscous threads orients the nanotubes inside the matrix. At 1% CNT loadings, the final CNT reinforced CMC material electrical conductivity was measured to be in the range of 10 S/m. As the conductivities at lower CNTs concentrations were several orders of magnitude lower, the effect is explained by CNT percolation network throughout the oxide matrix. Demonstrated method is applicable to obtain a variety of shapes from CNT reinforced CMCs with different metal oxide matrices.

As a conclusion, the following several key findings of the thesis can be extracted:

- AQ and NAQ treated metal alkoxides consist elongated particles with approximately 4 nm in length and 2 nm in diameter. Additionally, NAQ-sample particles have cassiterite crystalline structure;
- jetting of AQ or NAQ treated metal alkoxides evoke nanometer-sized particles to form linear supramolecular aggregates, which causes material non-Newtonial fluid behavior;
- at precursors viscosities below the gelation point and contradiction to theoretical predictions, the shape of the formed fibers and needles is influenced by the pulling speed;
- CNTs in viscous sols decrease elongational viscosity and relaxation time with increasing CNTs content at low concentrations (less than 0.1wt%);
- fibers drawn from AQ or NAQ precursors differed in minimum dimensions as a result of different surface tension;
- at defined conditions, jet pinching from high-viscosity sols can lead to formation of solid needles;
- modified tape casting can be used to prepare either smooth and/or linearly structured sol-gel films from high-viscosity sol;
- CNTs can be homogeneously distributed into metal oxide ceramics obtained *via* metal alkoxide based sol-gel processes;
- through formed supramolecular aggregates in metal alkoxide sol material, jetting induces CNT orientation along the jet axis;

- electrical conductivity in CNT/metal oxide material is increased by several orders of magnitudes at low CNT concentrations which can be explained by CNTs percolation;

Novelty of the results:
- The pinching-off of metal alkoxide based liquid threads in air was demonstrated as a reproducible route for preparing novel structures – nanometer level sharp oxide needles;
- A modified sol-gel tapecasting (also called doctors blade) method was developed for the first time to prepare structured oxide films;
- For the first time fibers as thin as 200 nm were directly drawn from metal alkoxides using sol-gel methods;
- CNT-reinforced CMC fibers preparation from viscous metal alkoxide based precursors was demonstrated for the first time;
- Rheological parameters for fiber drawing from alkoxide/CNT material were determined;

6. SUMMARY IN ESTONIAN

Kokkuvõte

Töö „**Metalloksiidsete süsiniknanotorukomposiitide süntees: sool-geel prot-sess, reoloogia ning struktuurilised ja funktsionaalsed omadused**" käsitleb materjaliteaduses väga aktuaalset teemat – kahe (või enama) erineva materjali sidumist üheks liit(komposiit)materjaliks selliselt, et säilivad mõlema alg-materjali parimad omadused. Saadud materjalide kasutamiseks praktilistes rakendustes on oluline, et saadud komposiitmaterjale oleks võimalikult lihtne vormida väga erineva geomeetrilise kujuga struktuurideks (pinnakatted, fiibrid, monoliidid, jne.). Komposiitmaterjalide arendusprotsess nõuab enamasti erine-vate füüsika ja keemia valdkondade omavahelist tihedat sünergiat, sest uue materjali väljatöötamiseks läheb vaja teadmiseid ja oskuseid alates orgaanilisest keemiast kuni teoreetilise füüsikani.

Käesoleva töö eesmärgiks oli seatud sool-geel meetodil valmistatud oksiid-sete mikro- ja nanostruktuuride moodustumise mehhanismide uurimine, sellis-tesse struktuuridesse süsiniknanotorude viimise metoodika väljatöötamine ning saadud struktuursete komposiitmaterjalide omaduste uurimine. Töö käigus kasutati mitmeid konventsionaalseid meetodeid, kuid materjalide erilisuse tõttu tuli välja töötada ja kasutada ka mitmeid uudseid tehnikaid oksiidsete mikro- ja nanomaterjalide formeerimiseks ning iseloomustamiseks.

Nanomõõtmeliste kerakujuliste süsinikstruktuuride ehk fullereenide avasta-misest alates 1985. aastal, on järgnevatel kümnenditel kirjeldatud ja sünteesitud veel rida süsiniknanomaterjale – mitmeseinalised süsiniknanotorud (1991), ühe-seinalised nanotorud (1993), süsiniknanotoru köiestruktuurid (1996), süsinik-nanovaht (1999), „kalasaba" ja „bambuse" struktuuriga süsiniknanofiibrid (2006, 2005), süsiniknanorõngad (2009) jne. Neist üks enim tähelepanu pälvi-nud süsiniknanomaterjale on kindlasti suurepäraste füüsikaliste ja keemiliste omadustega süsiniknanotorud. Fenomenaalse tugevuse ning väga hea elektri- ja soojusjuhina nähakse neid praktilistes rakendustes näiteks ehituses, lennun-duses, elektroonilistes seadmetes, päikesepaneelides, sensorites, jne. Süsinik-nanotorude omadused, mis ühelt poolt võiksid potentsiaalselt kasu tuua, on teiselt poolt takistuseks nende reaalsel kasutamisel. Süsiniknanotorude potent-siaal erinevates rakendustes on siiani jäänud realiseerimata paljuski nende väga väikeste mõõtmete, pikkuse ja läbimõõdu suhte ning spetsiifiliste omaduste tõttu. Peamiselt on lahendamata jäänud mitmesugused probleemid, mis tekivad süsiniknanotorude sünteesimisel, nanotorude puhastamisel sünteesi kõrvalpro-duktidest ning nanotorude dispergeerimisel ja sidumisel erinevate kekskonda-dega. Materjalide tugevamaks ja elektrit juhtivamaks muutmise eesmärgil on kõnealuseid, kuni mitme sentimeetri pikkuseid ja tavaliselt 3–50 nanomeetrise läbimõõduga, süsinikstruktuure lisatud enamasti mitmesugustesse plastikutesse. Eeldusel, et täitematerjal on ühtlaselt jaotunud ning täitematerjali ja maatriksi vahel on saavutatud piisav interaktsioon, on tulemuseks puhtast maatriksist

mitmeid suurusjärke parema elektrijuhtivuse ja/või tugevusega komposiit-materjal.

Lisaks eelmainitud plastikutele on erinevates rakendustes tähtsad keemiliselt vastupidavad, stabiilsed ja tihtipeale heade optiliste omadustega keraamilised ning klaasmaterjalid. Enamasti on keraamiliste materjalide puuduseks haprus ning suur elektritakistus. Mitmed teadustööd on näidanud, et süsiniknanotorude lisamisel keraamilisse maatriksisse on võimalik valmistada optiliselt ja elektriliselt juhtivaid, mehaaniliselt tugevaid ning keemiliselt stabiilseid komposiit-materjale. Üks paljulubavamaid meetodeid keraamiliste komposiitide valmistamiseks on niinimetatud sool-geel metoodika. Sool-geel metoodika nimetus tuleneb protsessist, mille tulemusena väga väikesed osakesed lahuses („sool") interakteeruvad üksteisega kuni moodustub läbi kogu lahuse ulatuv tahke kolme-mõõtmeline struktuur („geel"). Selle protsessi tulemusena kaotab lahus suure osa oma voolavusest ja ning geelistub. Sool-geel meetodi peamisteks eelisteks on meetodi lihtsus ning paindlikus. Kuna kogu protsess toimub vedelas olekus ning madalal temperatuuril, on lõpptulemusena saadavate keraamiliste ja klaasmaterjalide koostist, homogeensust ning lisandite lisamist lihtne kontrollida. Lisaks eelnevale on erinevalt konkureerivatest meetoditest (näiteks: kuumpressimine, eelnevalt valmistatud oksiidide seguks jahvatamine), sool-geel meetodiga võimalik keraamilisse maatriksisse viia termiliselt ebastabiilseid lisandeid ning isegi elus rakke. Rakenduslikust küljest on selle meetodi eelisteks võimalus katta suuri pindu, meetodi madal hind ning võimalus valmistada väga erineva geomeetriaga mikro- ja makroskoopilisi oksiidseid struktuure (kiled, fiibrid, monoliidid, torud, teravikud jne.).

Oksiidsete materjalide valmistamiseks sool-geel tehnoloogiaga on üheks enim kasutatavaks lähteainete rühmaks mitmesugused alkoksiidid. Siiani on kõige rohkem teaduslikult uuritud ja tööstuses oksiidsete materjalide saamiseks kasutatud räänialkoksiide. Enamasti kasutatakse alkoksiididest sooli saamiseks lähteaine reageerimist veega (hüdrolüüsimist), vähem on levinud alkoksiidide termiline kondenseerimine sooliks. Kuna räni- ja metallialkoksiididel on palju sarnaseid keemilisi ja füüsikalisi omadusi, siis eeldati, et metalli alkoksiidid käituvad näiteks veega reageerides sama moodi nagu räänialkoksiidid. Viimasel kümnendil on aga hakatud mõistma, et toimuvad hüdrolüüsi-kondensatsiooni protsessid on kummagi alkoksiidide rühma korral erinevad. Selle tõttu on ka metallialkoksiididest saadud soolide struktuur ja omadused teistsugused kui vastavatel räänühenditel. Soolide omadused ning struktuur aga omakorda määravad edasised struktuuride formeerimise tingimused.

Sool-geel meetodil saadavate geelstruktuuride moodustumist mõjutavad kõige enam kasutatava sooli viskoossus ja reoloogilised parameetrid. Sooli viskoossus sõltub omakorda temas sisalduvate osakeste mõõtmetest ning omadustest. Käesolevas töös uuriti töötlemata metallialkoksiidide, hüdrolüüsitud alkoksiidide ning termiliselt töödeldud alkoksiidide struktuuri ning omadusi. Lisaks määrati erinevate alkoksiidide fiibriks tõmbamise optimaalsed tingimused. Erinevaid mõõtemeetodeid kasutades leiti, et fiiberstruktuuride saamiseks

enim sobilikud tina(IV)butoksiidi soolid sisaldasid keskmiselt 4 nanomeetrit pikki ja 2 nanomeetrilise läbimõõduga piklike osakesi. Termiliselt töödeldud proovide osakesed sisaldasid omakorda ~1nm suuruseid kassiteriidi osakesi. Ülejäänud proovide osakesed olid amorfsed.

Metallialkoksiidide ja neist valmistatud soolide reoloogilised mõõtmised näitasid, et need käituvad nagu tüüpilised anomaalviskoossusega vedelikud (*ing. k. non-Newtonian fluid*). Materjalide joaks tõmbamisel tekkivat nihkevedeldumise (*ing. k. shear thinning*) efekti võib seletada eelnevalt kirjeldatud piklike osakeste omavahelise libisemisega materjalis. Sarnased nihkevedeldumise mehhanismid toimuvad ka polümeersete plastikute voolamisel. Süsiniknanotorude mõju hindamiseks alkoksiidsete materjalide voolamisomadustele kasutati spetsiaalset eelnevalt väljatöötatud metoodikat ja aparatuuri, mille korral materjalidest joa tõmbamine toimus reaktsioonikolvis. See oli vajalik vältimaks alkoksiidide reageerimist õhuniiskusega. Materjali venitamisel tekkinud joa mõõtmete analüüsimisel saadud andmetest lähtus, et süsiniknanotorude kontsentratsiooni suurenedes (kuni 0,1 massi %) väheneb alkoksiidse materjali viskoossus.

Käesoleva doktoritöö käigus kasutati kahte erinevat meetodit fiiberstruktuuride valmistamiseks alkoksiidsetest lähteainetest. Esimesel juhul tõmmati vedel materjali juga algsest veevabast keskkonnast kõrge õhuniiskusega keskkonda, kus joa pind veeaurudega reageerides tahkestus. Selle tulemusena moodustus tahke geelfiiber, mida hiljem kuumutades saadi kristallilise struktuuriga oksiidne fiibermaterjal. Teisel juhul toimus kogu tõmbamise protsess kõrge õhuniiskusega keskkonnas. Valmistatud fiibrite pikkuse ja diameetri suhe oli kuni 10 000 ning minimaalne diameeter 200 nanomeetrit. Kõige ühtlasemaid ja väikseima diameetriga fiibreid oli võimalik valmistada termiliselt töödeldud lähtematerjalidest, sest võrreldes hüdrolüüsitud lähteainetega, on need keemiliselt stabiilsemad, elastsemad ja madalama pindpinevusega. Need omadused võimaldavad sellist juga enne tahkestumist niiskes keskkonnas võimalikult pikaks ja peenikeseks venitada.

Sõltuvalt lähteaine omadustest ja ümbritseva keskkonna tingimustest, toimub lõpuks lähtematerjalist tõmmatud joa katkemine. Käesolevas töös demonstreeriti, et lähteaine ning ümbritseva keskkonna omadusi optimeerides ja metalli alkoksiidist tõmmatud joa katkemist ära kasutades on võimalik valmistada väga väikese tipuraadiusega oksiidseid teravike. Elektronmikroskoobi kujutistelt ilmnes, et teravikstruktuurid olid ka nanoskaalal ühtlase koonilise profiiliga. Oksiidsete teravikstruktuuride tipuraadiused olid 15–25 nanomeetrit. Selliste struktuuride teke on seletatav lähtematerjali väga kiire tahkestumisega, mis toimub enne, kui pindpinevusest tingituna jõuab katkemise kohta hakata moodustuma vedela materjali tilk.

Väga levinud kilede valmistamise meetoditeks madala viskoossusega soolgeel lähtematerjalidest on nn. vurr-katmine (*ing. k. spin coating*) ja sukelduspindamise meetod (*ing. k dip coating*). Vurr-katmise puhul tilgutatakse pöörlevale substraadile lähtematerjali, mis tsentrifugaaljõudude toimel kile moodustab.

Sukelduspindamise meetodi puhul kastetakse substraat lihtsalt teatud ajaks lähtematerjali sisse. Kumbki meetod ei võimalda valmistada väga pakse ega struktuurseid pinnakatteid. Käesoleva doktoritöö käigus näidati, et kasutades nn. modifitseeritud määrimismeetodit (*ing. k. tape casting*), on kõrge viskoossusega lähtematerjalidest võimalik valmistada struktuurseid kilesid ja/või siledaid kilesid paksusega kuni mõni mikromeeter. Samuti sobib selline meetod suurte pindade katmiseks.

Antud töös kasutati nanotorude paremaks dispergeerimiseks oksiidse komposiitmaterjali lähteaines ainult ultraheliseadmeid. Oksiidse komposiitmaterjali uurimisel elektronmikroskoobi ja fokusseeritud ioonkiire abil näidati, et väljatöötatud meetodil saadud materjalis on nanotorude jaotus ühtlane. Lisaks demonstreeriti, et materjali joaks tõmbamine orienteerib nanotorusid tõmbamise suunas. Kõige parema elektrijuhtivusega (10 S/m) olid materjalid, millesse oli lisatud 1 massi % süsiniknanotorusid. Väiksemate nanotorude kontsentratsioonide korral oli elektrijuhtivus mitu suurusjärku madalam. Selline juhtivuse hüppeline kasv on seletatav süsiniknanotorude võrgustiku e. perkolatsiooni tekkimisega, mis leidis samuti kinnitust elektronmikroskoobi kujutiste analüüsimisel. Demonstreeritud meetod süsiniknanotorudega dopeeritud komposiitmaterjalide valmistamiseks võimaldab formeerida väga erineva geomeetriaga struktuure väga erinevate metallide oksiididest.

Töö olulisemad uudsed tulemused:
- Hüdrolüüsitud ning termiliselt töödeldud metalli alkoksiidid sisaldavad piklikke osakesi, mis on keskmiselt 4 nanomeetrit pikad ja 2 nanomeetri laiused. Termiliselt töödeldud proovide osakestel on kassiteriidi struktuur.
- Hüdrolüüsitud ning termiliselt töödeldud metalli alkoksiidide joaks tõmbamisel moodustavad eelpool mainitud piklikud osakesed suuremaid lineaarseid agregaate, mis põhjustavad viskoossete alkoksiidsete materjalide anomaalviskoosset voolamist.
- Erinevalt teoreetilistest ennustustest mõjutab joa tõmbamise kiirus moodustuvate fiibrite ning nõelstruktuuride kuju.
- Süsiniknanotorude kontsentratsiooni (kuni 0,1 massi %) suurendamisel metallialkoksiidides väheneb kogu materjali viskoossus.
- Hüdrolüüsitud ning termiliselt töödeldu alkoksiidid võimaldasid erineva pindpinevuse tõttu neist tõmmata erinevate mõõtmetega fiibermaterjale.
- Esmakordselt näidati, et kasutades termiliselt töödeldud metallialkoksiide on sool-geel meetodil võimalik valmistada minimaalselt kuni 200 nanomeetrilise läbimõõduga oksiidseid fiibreid.
- Esmakordselt näidati, et sõltuvalt lähteaine omadustest ja ümbritseva keskkonna tingimustest, viib viskoossest alkoksiidsest lähtematerjalist tõmmatud joa katkemine väga väikese tipuraadiusega nõelstruktuuride tekkimiseni. Samuti on viskoosset lähtematerjali, kontrollitud keskkonna tingimusi ja modifitseeritud määrimismeetodit (*ing. k. tape casting*) kasutades võimalik valmistada siledaid või struktuurseid pinnakatteid.

- Demonstreeriti, et sool-geel metoodikat kasutades on keraamilistes materjalides võimalik saavutada süsiniknanotorude ühtlane jaotus.
- Esmakordselt demonstreeriti süsiniknanotorudega dopeeritud metalloksiidsete fiibrite valmistamist sool-geel meetodil ja määrati optimaalsed reoloogilised parameetrid sellise fiibermaterjali formeerimiseks.
- Süsiniknanotorudega lisandatud kontsentreeritud alkoksiidse sooli joaks tõmbamisel orienteeritakse materjalis olevad süsiniknanotorud tõmbamise suunas.
- Väikeste koguste süsiniknanotorude lisamine metalloksiididesse suurendab nende materjalide elektrijuhtivust mitu suurusjärku. See on seletatav süsiniknanotorude võrgustiku e. perkolatsiooni tekkimisega.

REFERENCES

[1] J. D. Bernal, *P. Roy. Soc. Lond. A Mat.* **106**, 749–773 (1924).

[2] A. Loiseau, P. Launois, P. Petit, S. Roche, J.-P. Salvetat (Eds.), Understanding carbon nanotubes – From Basics to Applications, Springer, Berlin 2006.

[3] H.W. Kroto, J.R. Heath, S.C. O'Brien, R.F. Curl, R.E. Smalley, *Nature* **318**, 162–163 (1985).

[4] S. Iijima, *Nature* **354**, 56–58 (1991).

[5] S. Iijima, T. Ichibashi, *Nature* **363**, 603–605 (1993).

[6] D. S. Bethune, C. H. Klang, M. S. de Vries, G. Gorman, R. Savoy, J. Vazquez, R. Beyers, *Nature* **363**, 605–607 (1993).

[7] L. V. Radushkevich, V.M. Lukyanovich, *J. Phys. Chem. Russia* **26**, 88–95 (1952).

[8] M. Hillert, N. Lange, *Z. Kristallogr.* **111**, 24–34 (1958).

[9] A. Oberlin, M. Endo, T. Koyama, *J. Cryst. Growth* **32**, 335–349 (1976).

[10] J. Abrahamson, P.G. Wiles, B.L. Rhoades, Structure of carbon fibers found on carbon arc anodes, "14th Biennial Conference on Carbon American Carbon Society", University Park, PA, June (1979).

[11] Z. Ren, Y. Lan, Y. Wang, Aligned Carbon Nanotubes – Physics, Concepts, Fabrication and Devices, Springer-Verlag, Heidelberg, 2013.

[12] S. Amelinckx, X. B. Zhang, D. Bernaerts, X. F. Zhang, V. Ivanov, J. B. Nagy, *Science* **265**, 635–639 (1994).

[13] A.Thess, R. Lee, P. Nikolaev, H. Dai, P. Petit, J. Robert, C. Xu, Y. H. Lee, S. G. Kim, A. G. Rinzler, D. T. Colbert, G. E. Scuseria, D. Tomanek, J. E. Fischer, R. E. Smalley, *Science* **273**, 483–487 (1996).

[14] B. W. Smith, M. Monthioux, D. E. Luzzi, *Nature* **396**, 323–324 (1998).

[15] A. V. Rode, S. T. Hyde, E. G. Gamaly, R. G. Elliman, D. R. McKenzie, S. Bulcock, *Appl. Phys. A* **69**, S755–S758 (1999).

[16] J. Li, C. Papadopoulos, J. Xu, *Nature* **402**, 253–254 (1999).

[17] T. Uchida, D. P. Anderson, M. L. Minus, S. Kumar, *J. Mater. Sci.* **41**, 5851–5856 (2006).

[18] A. V. Melechko, V. I. Merkulov, T. E. McKnight, M. A. Guillorn, K. L. Klein, D. H. Lowndes, M. L. Simpson, *J. Appl. Phys.* **97**, 041301(1)–041301(39) (2005).

[19] A. G. Nasibulin, P. V. Pikhitsa, H. Jiang, D. P. Brown, A. V. Krasheninnikov, A. S. Anisimov, P. Queipo, A. Moisala, D. Gonzalez, G. Lientschnig, A. Hassanien, S. D. Shandakov, G. Lolli, D. E. Resasco, M. Choi, D. Tománek, E. I. Kauppinen, *Nat. Nanotechnol.* **2**, 156–161 (2007).

[20] R. Jasti, C. Bertozzi, "Process for preparation of carbon nanohoops compounds" US Patent 20110166390, (2011).

[21] S. C. Tjong, Carbon Nanotube Reinforced Composites – Metal and Ceramic Matrices, Wiley-VCH, Weinheim, 2009.

[22] M. Meyyappan, Carbon nanotubes – science and applications, CRC Press, Boca Raton 2005.

[23] E. Thostenson, Z. Ren, T. Chou, *Compos. Sci. Technol.* **61**, 1899–1912 (2001).

[24] M. S. Dresselhaus, G. Dresselhaus, R. Saito, *Carbon* **33**, 883–891 (1995).

[25] C. Kane, L. Balents, M.P.A. Fisher, *Phys. Rev. Lett.* **79**, 5086–5089 (1997).

[26] N. Hamada, S.-I. Sawada, A. Oshiyama, *Phys. Rev. Lett.* **68**, 1579–1581 (1992).

[27] R. Saito, M. Fujita, G. Dresselhaus, M.S. Dresselhaus, *Phys. Rev. B* **46**, 1804–1811 (1992).

[28] R. Saito, M. Fujita, G. Dresselhaus, M.S. Dresselhaus, *Appl. Phys. Lett.* **60**, 2204–2206 (1992).

[29] T. W. Odom, J.-L. Huang, P. Kim, C. M. Lieber, *Nature* **391**, 62–64 (1998).

[30] J. W. G. Wildöer, L. C. Venema, A. G. Rinzler, R. E. Smalley, C. Dekker, *Nature* **391**, 59–62 (1998).

[31] C. N. R. Rao, R. Voggu, A. Govindaraj, *Nanoscale* **1**, 96–105 (2009).

[32] C. Shen, A. H. Brozena, Y. Wang, *Nanoscale* **3**, 503–518 (2011).

[33] S. Frank, P. Poncharal, Z. L. Wang, W. A. de Heer, *Science* **280**, 1744–1746 (1998).

[34] X. Wang, Q. Li, J. Xie, Z. Jin, J. Wang, Y. Li, K. Jiang, S. Fan, *Nano Lett.* **9**, 3137–3141 (2009).

[35] M. F. L. De Volder, S. H. Tawfick, R. H. Baughman, A. J. Hart, *Science* **339**, 535–539 (2013).

[36] X. Zhao, M. Ohkohchi, S. Inoue, T. Suzuki, T. Kadoya, Y. Ando, *Diam. Relat. Mater.* **15**, 1098–1102 (2006).

[37] T. Guo, P. Nikolev, A. Thess, D. T. Colbert, R. E. Smalley, *Chem. Phys. Lett.* **243**, 49–54 (1995).

[38] M. Endo, T. Hayashi, Y.-A. Kim, *Pure Appl. Chem.* **78**, 1703–1713 (2006).

[39] P. Launois, M. Chorro, B. Verberck, P. A. Albouy, S. Rouziere, D. Colson, A. Forget, L. Noe, H. Kataura, M. Monthioux, J. Cambedouzou, *Carbon* **48**, 89–98 (2009).

[40] A. Jorio, G. Dresselhaus, M. S. Dresselhaus (Eds.), Carbon Nanotubes: Advanced Topics in the Synthesis, Structure, Properties and Applications, Springer-Verlag, Berlin (2008).

[41] Z. F. Ren, Z. P. Huang, J. W. Xu, J. H. Wang, *Science* **282**, 1105–1107 (1998).

[42] D. N. Futaba, K. Hata, T. Yamada, T. Hiraoka, Y. Hayamizum Y. Kakudate, O. Tanaike, H. Hatori, M. Yumura, S. Iijima, *Nat. Mater.* **5**, 987–994 (2006).

[43] Y. Hayamizu, T. Yamada, K. Mizuno, R. C. Davis, D. N. Futaba, M. Yumura, K. Hata, *Nat. Nanotechnol.* **3**, 289–294 (2008).

[44] M. De Volder, S. H. Tawfick, S. J. Park, D. Copic, Z. Zhao, W. Lu, A. J. Hart, *Adv. Mater.* **22**, 4384–4389 (2010).

[45] M. Zhang, K. R. Atkinson, R. H. Baughman, *Science* **306**, 1358–1361 (2004).

[46] K. Jiang, Q. Li, S. Fan, *Nature* **419**, 801 (2002).

[47] J. L. Zimmerman, R. K. Bradley, C. B. Huffman, R. H. Hauge, J. L. Margrave, *Chem. Mater.* **12**, 1361–1366 (2000).

[48] S. Porro, S. Musso, M. Vinante, L. Vanzetti, M. Anderle, F. Trotta, A. Tagliaferro, *Physica E* **37**, 58–61 (2007).

[49] F. Li, H. M. Cheng, Y. T. Xing, P. H. Tan, G. Su, *Carbon* **38**, 2041–2045 (2000).

[50] K. L. Lu, L. M. Lago, Y. K. Chen, M. L. Green, P. J. Harris, S. C. Tsang, *Carbon* **34**, 814–816 (1996).

[51] Y. Wang, J. Wu, F. Wei, *Carbon* **41**, 2939–2948 (2003).

[52] N. Pierrard, A. Fonseca, Z. Konya, I. Willems, G. Van Tendeloo, J. B. Nagy, *Chem. Phys. Lett.* **335**, 1–8 (2001).

[53] R. Chavan, U. Desai, P. Mhatre, R. Chinchole, *Int. J. Pharm. Sci. Rev. Res.* **13**, 125–134 (2012).

[54] H. T. Ham, Y. S. Choi, I. J. Chung, *J. Colloid Interf. Sci.* **286**, 216–223 (2005).

[55] A. Hirsch, *Angew. Chem. Int. Edit.* **41**, 1853–1859 (2002).

[56]   J. Hilding, E. A. Grulke, Z. G. Zhang, F. Lockwood, *J. Disper. Sci. Technol.* **24**, 1–41 (2003).

[57]   X. Li, Y. Qin, S. T. Picraux, Z.-X. Guo, *J. Mater. Chem.* **21**, 7527–7547 (2011).

[58]   S. W. Kim, T. Kim, Y. S. Kim, H. S. Choi, H. J. Lim, S. J. Yang, C. R. Park, *Carbon* **50**, 3–33 (2012).

[59]   C. W. W. Ostwald, "Die Welt der Vernachlässigten Dimensionen", 4th edn. Steinkopf, Dresden, (1921).

[60]   International Union of Pure and Applied Chemistry, Compendium of Chemical Terminology (Gold Book), Version 2.3.2, 19.08.2012.

[61]   M. Ebelmann, *Ann. Chem. Phys.* **16**, 129 (1846).

[62]   S. S. Kistler, *Nature* **127**, 741 (1931).

[63]   W. Geffcken, E. Berger, "Changing the reflective capacity of optical glass", DE Patent 736411, (1943).

[64]   H. Dislich, P. Hinz, R. Kaufmann, "Preparation of transparent, vitreous, crystalline inorganic multiple component materials, especially in thin layers, at temperatures far below their melting points", DE Patent 1941191, (1971).

[65]   H. Dislich, *Angew. Chem. Int. Edit.* **10**, 363–370 (1971).

[66]   http://www.bell-labs.com/org/physicalsciences/projects/solgel/solgel.html   (by Lucent Technologies).

[67]   M. Pagliaro, R. Ciriminna, G. Palmisano, *Chem. Soc. Rev.* **36**, 932–940 (2007).

[68]   D. Avnir, T. Coradin, O. Lev, J. Livage, *J. Mater. Chem.* **16**, 1013–1030 (2006).

[69]   S. Sakka, Handbook of Sol-Gel Science and Technology – Processing, Characterization and Applications, Kluwer Academic Publishers, New York, 2005.

[70]   H. Dislich, E. Hussmann, *Thin Solid Films* **77,** 129–139 (1981).

[71]   L. Klein, Sol-Gel Optics – Processing and Applications, Kluwer Academic Publishers, Dordrecht, 1994.

[72]   http://ceramics.org/ceramic-tech-today/biomaterials/continued-growth-of-sol-gel-market-predicted (by The American Ceramic Society).

[73]   http://www.companiesandmarkets.com/Market/Chemicals/Market-Research/Global-Sol-Gel-Product-Market-2012-2016/RPT1153337 (by Vertical Edge Limited).

[74]   http://www.boeingsuppliers.com/environmental/solgel.html   (by   The   Boeing Company).

[75]   T. Minami, *J. Sol-Gel Sci. Technol.* **65**, 4–11 (2013).

[76]   http://www.morganthermallillebonne.com/products/solgel-fibre-products/   (by The Morgan Advanced Materials Company).

[77]   http://www.solgel.com/biz/com.htm (by www.solgel.com).

[78]   http://www.taasi.com/what.htm (by TAASI Corporation).

[79]   V. G. Kessler, G. A. Seisenbaeva from "Sol-Gel Methods for Materials Processing", P. Innocenzi et al (Ed.), (Springer, Berlin), 139–153 (2008).

[80]   V. G. Kessler, G. I. Spijksma, G. A. Seisenbaeva, S. Håkansson, D. H. A. Blank, H. J. M. Bouwmeester, *J. Sol-Gel Sci. Technol.* **40**, 163–179 (2006).

[81]   V. G. Kessler, *J. Sol-Gel Sci. Technol.* **51**, 264–271 (2009).

[82]   G. A. Seisenbaeva, S. Gohil, V. G. Kessler, *J. Mater. Chem.* **14**, 3177–3190 (2004).

[83]   G. I. Spijksma, G. A. Seisenbaeva, A. Fischer, H. J. M. Bouwmeester, D. H. A. Blank, V. G. Kessler, *J. Sol-Gel Sci. Technol.* **51**, 10–22 (2009).

[84]   R. Lichtenberger, U. Schubert, *J. Mater. Chem.* **20**, 9287–9296 (2010).

[85]   G. Westin, U. Bemm, R. Norrestam, M. Nygren, *J. Sol-Gel Sci. Technol.* **8**, 23–28 (1997).

[86] N. Y. Turova, E. P. Turevskaya, V. G. Kessler, M. I. Yanovskaya, The Chemistry of Metal Alkoxides, Kluwer Academic Publishers, New York, 2002.

[87] M. Kallala, C. Sanchez, B. Cabane, *Phys. Rev.* E **48**, 3692–3704 (1993).

[88] J. Livage, M. Henry, C. Sanchez, *Prog. Solid State Ch.* **18**, 259–341 (1988).

[89] I. Chilibon, J. N. Marat-Mendes, *J. Sol-Gel Sci. Technol.* **64**, 571–611 (2012).

[90] J. H. Wengrovius, M. F. Garbauskas, E. A. Williams, R. C. Going, P. E. Donahue, J. F. Smith, *J. Am. Chem. Soc.* **108**, 982–989 (1986).

[91] D. C. Bradley, D. G. Carter, *Can. J. Chem.* **40**, 15–21 (1962).

[92] J. M. Nedelec, *J. Nanomater.* **2007** *, 8 pages (2007).*

[93] C. J. Brinker, G. W. Scherer, Sol-Gel Science – The Physics and Chemistry of Sol-Gel Processing, Academic Press, Boston, 1990.

[94] M. T. Harris, A. Singhal, J. L. Look, J. R. Smith-Kristensen, J. S. Lin, L. M. Toth, *J. Sol-Gel Sci. Technol.* **8**, 41–47 (1997).

[95] U. Schubert, N. Hüsing, Synthesis of inorganic materials, Wiley-VCH, Weinheim, 2000.

[96] K. C. Fortner, J. P. Bigi, S. N. Brown, *Inorg. Chem.* **44**, 2803–2814 (2005).

[97] G. Fornasieri, L. Rozes, S. Le Calve, B. Alonso, D. Massiot, M. N. Rager, M. Evain, K. Boubekeur, C. Sanchez, *J. Am. Chem. Soc.* **127**, 4869–4878 (2005).

[98] A. Senouci, M. Yaakoub, C. Huguenard, M. Henry, *J. Mater. Chem.* **14**, 3215–3230 (2004).

[99] J. Livage, C. Sanchez, *J. Non-Cryst. Solids.* **145**, 11–19 (1992).

[100] C. J. Brinker, *J. Non-Cryst. Solids* **100**, 31–50 (1988).

[101] V. W. Day, T. A. Eberspacher, Y. Chen, J. Hao, W. G. Klemperer, *Inorg. Chim. Acta.* **229**, 391–505 (1995).

[102] W. J. Evans, M. A. Ansari, J. W. Ziller, *Polyhedron* **17**, 869–877 (1998).

[103] N. Y. Turova, *Russ. Chem. Rev.* **73,** 1041–1064 (2004).

[104] M. Niederberger, G. Garnweitner, *Chem. Eur. J.* **12**, 7282–7302 (2006).

[105] B. J. J. Zelinski, D. R. Uhlmann, *Phys. Chem. Solids* **45**, 1069–1090 (1984).

[106] K. A. Andrianov, Metalorganic Polymers, Wiley, New York, 1965.

[107] J. Rinse, *Ind. Eng. Chem.* **56**, 42–50 (1964).

[108] A. N. Nesmeyanov, E. M. Brainina, R. K. Freidlina, *Dokl. Akad. Nauk SSSR* **85**, 571–573 (1952).

[109] V. G. Kessler, G. A. Seisenbaeva, M. Unell, S. Håkansson, *Angew. Chem.* **47**, 8506–8509 (2008).

[110] G. Goutailler, C. Guillard, S. Daniele, L. G. Hubert-Pfalzgraf, *J. Mater. Chem.* **13**, 342–346 (2003).

[111] M. J. Uddin, F. Cesano, F. Bonino, S. Bordiga, G. Spoto, D. Scarano, A. Zecchina, *J. Photochem. Photobiol. A* **189**, 286–294 (2007).

[112] R. K. Pati, I. C. Lee, K. J. Gaskell, S. H. Ehrman, *Langmuir* **25**, 67–70 (2009).

[113] B. K. Teo, X. Shi, H. Zhang, *J. Am. Chem. Soc.* **114**, 2743–2745 (1992).

[114] M. J. Lundqvist, M. Nilsing, P. Persson, S. Lunell, *Int. J. Quantum. Chem.* **106**, 3214–3234 (2006).

[115] P. Persson, J. C. M. Gebhardt, S. Lunell, *J. Phys. Chem. B* **107**, 3336–3339 (2003).

[116] I. Djerdj, D. Arcon, Z. Jaglicic, M. Niederberger, *J. Solid State Chem.* **181**, 1571–1581 (2008).

[117] G. A. Seisenbaeva, S. Gohil, K. Jansson, K. Herbst, M. Brorson, V. G. Kessler, *New J. Chem.* **27**, 1059–1064 (2003).

[118] R. Pazik, D. Hreniak, W. Strek, V. G. Kessler, G. A. Seisenbaeva, *J. Alloy. Compd.* **451,** 557–562 (2008).

[119] G. Oskam, *J. Sol-Gel Sci. Technol.* **37**, 161–164 (2006).

[120] T. Kojima, T. Sugimoto, *J. Phys. Chem. C* **112**, 18445–18454 (2008).

[121] P. Raveendran, M. Eswaramoorthy, U. Bindu, M. Chatterjee, Y. Hakuta, H. Kawanami, F. Mizukami, *J. Phys. Chem. C* **112**, 20007–20011 (2008).

[122] B. Gauthier-Manuel, E. Guyon, S. Roux, S. Gits, F. Lefaucheux, *J. Phys-Paris* **48**, 869–875 (1987).

[123] A. P. Deshpande, J. M. Krishnan, P. B. S. Kumar, Rheology of Complex Fluids, Springer, New York, 2010.

[124] C. Kanbara, Experimental Study on High Polymers. Mechanical Properties I, Kyoritsu Shuppan, Tokyo, 1982

[125] S. Onogi, Rheology for Chemists, Kagakudonin, Kyoto, 1982.

[126] S. Okamura, A. Nakajima, S. Onogi, H. Kawai, N. Nishijima, T. Higashimura, N. Ise, Introduction to Polymer Chemistry, Kagakudonin, Tokyo, 1981.

[127] Wiley-VCH (Ed.), Ullmann's Fibers, Wiley-VCH, Weinheim, 2008.

[128] F. T. Trouton, *Proc. Roy. Soc. A* **77**, 426–440 (1906).

[129] C. J. Brinker, D. E. Clark, D. R. Ulrich, Better Ceramics Through Chemistry, North-Holland, New York, 1984.

[130] S. Sakka, K. Kamiya, K. Makita, Y. Yamamoto, *J. Non-Cryst. Solids* **63**, 223–235 (1984).

[131] S. Sakka, K. Kamiya, *J. Non-Cryst. Solids* **48**, 31–46 (1982).

[132] S. Sakka, K. Kamiya, T. Kato, *Yogyo-Kyokai-Shi* **90**, 79–80 (1982).

[133] K. Kamiya, T. Yoko, H. Suzuki, *J. Non-Cryst. Solids* **93**, 407–414 (1987).

[134] A. Einstein, *Ann. Phys.* **19**, 289–306 (1906); **34**, 591–592 (1911).

[135] Y. Abe, T. Misono, *J. Polym. Sci. Pol. Chem.* **21**, 41–53 (1983).

[136] T. Maki, S. Sakka, *J. Non-Cryst. Solids* **100,** 303–308 (1988).

[137] C. Wolf, C. Rüssel, *J. Mater. Sci.* **27,** 3749–3755 (1992).

[138] S. Sakka, T. Yoko, *J. Non-Cryst. Solids* **147/148**, 394–403 (1992).

[139] F. Savart, *Ann. Chim.* **53**, 337–386 (1833).

[140] J. Eggers, E. Villermaux, *Rep. Prog. Phys.* **71**, 036601 (79pp) (2008).

[141] A. Ziabicki, R. Taksermann-Krozer, *Kolloid Z.* **198,** 60 (1964).

[142] F. Rodriguez, Principles of Polymer systems 5th edn, Tailor and Francis, London, 2003.

[143] D. Li, Y. Xia, *Adv. Mater.* **16**, 1151–1170 (2004).

[144] T. Ondarçuhu, C. Joachim, *Europhys. Lett.* **42**, 215–220 (1998).

[145] Paper I

[146] S. Sakka, K. Kamiya, *Mat. Sci. Res.* **17**, 83–92 (1984).

[147] K. Saal, T. Tatte, M. Jarvekulg, V. Reedo, A. Lohmus, I. Kink, *Int. J. Mater. Prod. Tec.* **40**, 2–14 (2011).

[148] V. Reedo, M. Jarvekulg, A. Lohmus, U. Maeorg, *Phys. Stat. Sol. A* **205**, 1511–1514 (2008).

[149] Paper IV

[150] E. Zapata-Solvas, D. Gómez-García, A. Domínguez-Rodríguez, *J. Eur. Ceram. Soc.* **32**, 3001–3020 (2012).

[151] K. Ahmad, W. Pan, S.-L. Shi, *Appl. Phys. Lett.* **89,** 133122/1–133122/3 (2006).

[152] J. Cho, A. R. Boccaccini, M. S. P. Shaffer, *J. Mater. Sci.* **44**, 1934–1951 (2009).

[153] G. D. Zhan, J. D. Kuntz, J. E. Garay, A. K. Mukherjee, *Appl. Phys. Lett.* **83,** 1228–1230 (2003).

[154] J. Sun, L. Gao, W. Li, *Chem. Mater.* **14,** 5169–5172 (2002).

[155] J. Cho, S. Schaab, J.A. Roether, A.R. Boccaccini, *J. Nanopart. Res.* **10,** 99–105 (2008).

[156] E. Flahaut, A. Peigney, C. H. Marliere, F. Chastel, A. Rousset, *Acta Mater.* **48**, 3803–3812 (2000).

[157] C. B. Mo, S. I. Cha, K. T. Kim, K. H. Lee, S. H. Hong, *Mat. Sci. Eng. A-Struct.* **395**, 124–128 (2005).

[158] A. R. Boccaccini, J. Cho, T. Subhani, C. Kaya, F. Kaya, *J. Eur. Ceram. Soc.* **30**, 1115–1129 (2010).

[159] A. Peigney, S. Rul, F. Lefevre-Schlick, C. Laurent, *J. Eur. Ceram. Soc.* **27**, 2183–2193 (2007).

[160] A. J. López, A. Rico, J. Rodríguez, J. Rams, *Appl. Surf. Sci.* **256,** 6375–6384 (2010).

[161] G. Otieno, A. A. Koos, F. Dilon, A. Wallwork, N. Grobert, R. I. Todd, *Carbon* **48**, 2212–2217 (2010).

[162] B. T. T. Chu, G. Tobias, C. G. Salzmann, B. Ballesteros, N. Grobert, R. I. Todd, M. L. H. Green, *J. Mater. Chem.* **18**, 5344–5349 (2008).

[163] X.-M. Liu, Z.-D. Huang, S. Oh, P.-C. Ma, P. C. H. Chan, G. K. Vedam, K. Kang, J.-K. Kim, *J. Power Sources* **195**, 4290–4296 (2010).

[164] C. Arnould, T. I. Korányi, J. Delhalle, Z. Mekhalif, *J. Colloid Interf. Sci.* **344**, 390–394 (2010).

[165] V. O. Almeida, N. M. Balzaretti, T. M. H. Costa, G. B. Machado, M. R. Gallas, *J. Sol-Gel Sci. Technol.* **65**, 143–149 (2013).

[166] P. Vincent, A. Brioude, C. Journet, S. Rabaste, S. T. Purcell, J. Le Brusq, J. C. Plenet, *J. Non-Cryst. Solids* **311**, 130–137 (2002).

[167] A. Jitianu, T. Cacciaguerra, R. Benoit, S. Delpeux, F. Béguin, S. Bonnamy, *Carbon* **42**, 1147–1151 (2004).

[168] L. P. Zhao, L. Gao, *Carbon* **42**, 1858–1861 (2004).

[169] D. Eder, *Chem. Rev.* **110**, 1348–1385 (2010).

[170] K. Hernadi, E. Ljubovic, J. W. Seo, L. Forro, *Acta Mater.* **51**, 1447–1452 (2003).

[171] J. Sun, M. Iwasa, L. Gao, Q. Zhang, *Carbon* **42**, 895–899 (2004).

[172] W.-Q. Han, A. Zettl, *Nano Lett.* **3**, 681–683 (2003).

[173] J. Gong, J. Sun, Q. Chen, *Sensor. Actuat. B-Chem.* **130**, 829–835 (2008).

[174] C. Li, E. T. Thostenson, T.-W. Chou, *Compos. Sci. Technol.* **68**, 1445–1452 (2008).

[175] D. Stauffer, A. Aharony, Introduction to the percolation theory, Taylor & Francis, London, 1994.

[176] L.-P. Simoneau, J. Villeneuve, C. M. Aguirre, R. Martel, P. Desjardins, A. Rochefort, *J. Appl. Phys.* **114**, 114312/1–114312/8 (2013).

[177] R. Strumpler, J. Glatz-Reichenbach, *J. Electroceram.* **3**, 329–346 (1999).

[178] I. Balberg, D. Azulay, D. Toker, O. Millo, *Int. J. Modern Phys. B* **18**, 2091–2121 (2004).

[179] R. Holm, *J. Appl. Phys.* **22**, 569–574 (1951).

[180] A. Behnam, J. Guo, A. Ural, *J. Appl. Phys.* **102**, 044313/1–044313/7 (2007).

[181] X. Zeng, X. Xu, P. M. Shenai, E. Kovalev, C. Baudot, N. Mathews, Y. Zhao, *J. Phys. Chem. C* **115**, 21685–21690 (2011).

[182] N. Hu, Z. Masuda, C. Yan, G. Yamamoto, H. Fukunaga, T. Hashida, *Nano-technology* **19**, 215701/1–215701/10 (2008).

[183] W. Bauhofer, J. Z. Kovacs, *Compos. Sci. Technol.* **69**, 1486–1498 (2009).

[184] M. Grujicic, G. Cao, W. N. Roy, *J. Mater. Sci.* **39,** 4441–4449 (2004).

[185] S. Y. Kim, C. F. Zukoski, *Soft Matter* **8,** 1801–1810 (2012).

[186] R. G. Schmidt, G. V. Gordon, C. A. Dreiss, T. Cosgrove, V. J. Krukonis, K. Williams, P. M. Wetmore, *Macromolecules* **43**, 10143–10151 (2010).

[187] G. V. Gordon, R. G. Schmidt, M. Quintero, N. J. Benton, T. Cosgrove, V. J. Krukonis, K. Williams, P. M. Wetmore, *Macromolecules* **43**, 10132–10142 (2010).

[188] M. E. Mackay, T. T. Dao, A. Tuteja, D. L. Ho, B. Van Horn, H. C. Kim, C. J. Hawker, *Nat. Mater.* **2,** 762–766 (2003).

[189] A. Tuteja, M. E. Mackay, C. J. Hawker, B. Van Horn, *Macromolecules* **38**, 8000–8011 (2005).

[190] V. Ganesan, V. Pryamitsyn, M. Surve, B. Narayanan, *J. Chem. Phys.* **124**, 221102/1–221102/4 (2006).

[191] A. Tuteja, P. M. Duxbury, M. E. Mackay, *Macromolecules* **40**, 9427–9434 (2007).

[192] S. Jain, J. G. P. Goossens, G. W. M. Peters, M. van Duin, P. J. Lemstra, *Soft Matter* **4**, 1848–1854 (2008).

[193] G. D. Smith, D. Bedrov, L. Li, O. Byutner, *J. Chem. Phys.* **117,** 9478–9489 (2002).

[194] L. A. Hough, M. F. Islam, P. A. Janmey, A. G. Yodh, *Phys. Rev. Lett.* **93,** 168102/1–168102/4 (2004).

[195] S. G. Advani, Z. Fan, *AIP Conf. Proc.* **712**, 1619–1623 (2004).

[196] K. Miyazono, C. D. Kagarise, K. W. Koelling, M. Mahboob, S. E. Bechtel, *J. Appl. Polym. Sci.* **119**, 1940–1951 (2011).

[197] P. Potschke, T. D. Fornes, D. R. Paul, *Polymer* **43**, 3247–3255 (2002).

[198] Z. Fan, S. G. Advani, *Polymer* **46**, 5232–5240 (2005).

[199] T. McNally, P. Potschke, P. Halley, M. Murphy, D. Martin, S. E. J. Bell, G. P. Brennan, D. Bein, P. Lemoine, J. P. Quinn, *Polymer* **46**, 8222– 8232 (2005).

[200] S. B. Kharchenko, J. F. Douglas, J. Obrzut, E. A. Grulke, K. B. Migler, *Nat. Mater.* **3**, 564–568 (2004).

[201] A. W. K. Ma, F. Chinesta, T. Tuladhar, M. R. Mackley, *Rheol. Acta* **47**, 447–457 (2008).

[202] I. M. Thomas, "Method for producing stannic tertiary alkoxide" US Patent 3946056, (1976).

[203] I. J. C. Maire, *Ann. Chim.* **6**, 969–1026 (1961).

[204] J. C. Kearns, R. L. Shambaugh, *J. Appl. Polym. Sci.* **86**, 2079–2084 (2002).

[205] M. Hussainov, T. Tatte, I. Hussainova, *Rheol. Acta* **51**, 729–742 (2012).

[206] S. D. Christian, A. R. Slagle, E. E. Tucker, J. F. Scamehorn, *Langmuir* **14**, 3126–3128 (1998).

[207] http://www.mvm.kit.edu/english/697_786.php (by Karlsruhe Institute of Technology).

[208] http://www.newport.com/Introduction-to-FTIR-Spectroscopy/405840/1033/content.aspx (by Newport Corporation).

[209] http://nanoscience.huji.ac.il/unc/xrd_basics.htm (by The Hebrew University of Jerusalem).

[210] http://www.saxier.org/aboutus/saxs.shtml (by EMBL Hamburg).

[211] S. H. Spiegelberg, D. C. Ables, G. H. McKinley, *J. Non-Newton. Fluid* **64**, 229–267 (1996).

[212] A. Sacca, A. Carbone, E. Passalacqua, A. D'Epifanio, S. Licoccia, E. Traversa, E. Sala, F. Traini, R. Ornelas, *J. Power Sources* **152**, 16–21 (2005).

[213] P. K. Sharma, V. V. Varadan, V. K. Varadan, *Smart Mater. Struct.* **12**, 749–756 (2003).

[214] A. Seal, D. Chattopadhyay, A. Das Sharma, A. Sen, H. S. Maiti, *J. Eur. Ceram. Soc.* **24**, 2275–2283 (2004).

[215] T. Blythe, D. Bloor, Electrical Properties of Polymers, Cambridge University Press, Cambridge, 2005.

[216] http://serc.carleton.edu/research_education/geochemsheets/techniques/SEM.html (by Montana State University).

[217] http://www.imec.be/efug/EFUG10.html (by IMEC).

[218] B. Bhushan (Ed.), Springer Handbook of Nanotechnology, Springer, Berlin, 2004.

[219] http://www.microscopemaster.com/transmission-electron-microscope.html (by MicroscopeMaster.com).

[220] A. Isihara, *Polymer* **33**, 111–112 (1992).

[221] D. C. Bradley, E. V. Caldwell, W. J. Wardlaw, *Chem. Soc.* **79**, 4775 (1957).

[222] D. C. Bradley, R. C. Mehrotra, I. P. Rothwell, A. Singh, Alkoxo and Aryloxo Derivatives of Metals, Elsevier, NewYork, 2001.

[223] R. W. J. Scott, N. Coombs, G. A. Ozin, *J. Mater. Chem.* **13**, 969–974 (2003).

[224] M. J. Hampden-Smith, T. A. Wark, C. J. Brinker, *Coord. Chem. Rev.* **112**, 81–116 (1992).

[225] A. H. K. Garakani, N. Mostoufi, F. Sadeghi, M. Hosseinzadeh, H. Fatourechi, M. H. Sarrafzadeh, M. R. Mehrnia, *Iran. J. Environ. Health. Sci. Eng.* **8**, 255–264 (2011).

[226] A. Ponton, S. Barboux-Doeuff , C. Sanchez, *Colloid. Surface. A* **162**, 177–192 (2000).

[227] J. Eggers, *Phys. Rev. Lett.* **71**, 3458–3460 (1993).

[228] S. Sakka, H. Kozuka, *J. Non-Cryst. Solids* **100**, 142–153 (1988).

[229] S. L. Anna, G. H. McKinley, *J. Rheol.* **45**, 115–138 (2001).

[230] G. H. McKinley, A. Tripathi, *J. Rheol.* **44**, 653–670 (2000).

[231] T. Kairn, P. J. Daivis, I. Ivanov, S. N. Bhattacharya, *J. Chem. Phys.* **123**, 194905/1–194905/7 (2005).

[232] M. Wang, R. J. Hill, *Soft Matter.* **5**, 3940–3953 (2009).

[233] T. Tatte, T. Avarmaa, R. Lohmus, U. Maeorg, M.-E. Pistol, R. Raid, I. Sildos, A. Lohmus, *Mater. Sci. Eng. C* **19**, 101–104 (2002).

[234] J. K. Nielsen, H. K. Rasmussen, O. Hassager, G. H. McKinley, *J. Rheol.* **50**, 453–476 (2006).

[235] E. Betzig, J. K. Trautman, T. D. Harris, J. S. Weiner, R. L. Kostelak, *Science* **251**, 1468–1471 (1991).

[236] G. A. Valaskovic, M. Holton, G. H. Morrison, *Appl. Opt.* **34**, 1215–1228 (1995).

[237] L. Tong, R. R. Gattass, J. B. Ashcom, S. He, J. Lou, M. Shen, I. Maxwell, E. Mazur, *Nature* **426**, 816–819 (2003).

[238] B. Basu, K. Balani, Advanced Structural Ceramics, John Wiley & Sons, Hoboken, 2011.

[239] U. Joost, R. Pärna, M. Lembinen, K. Utt, I. Kink, M. Visnapuu, V. Kisand, *Phys. Status Solidi A* **210**, 1201–1212 (2013).

[240] J.-H. Du, J. Bai, H.-M. Cheng, *Express Polym. Lett.* **1**, 253–273 (2007).

[241] Z. Spitalsky, D. Tasis, K. Papagelis, C. Galiotis, *Prog. Polym. Sci.* **35**, 357–401 (2010).

ACKNOWLEDGEMENTS

Foremost, I would like to express my greatest gratitude to my supervisors, Dr. Tanel Tätte, Dr. Uno Mäeorg and Dr. Ilmar Kink for their support, encouragements and scientific advice throughout my Ph. D. studies. Current thesis and papers would not have been possible without their guidance, enthusiasm and considerable help.

I greatly appreciate all my colleagues, former colleagues, and friends from the Institute of Physics and from the Institute of Chemistry. Special thanks to Dr. Ants Lõhmus, Dr. Kristjan Saal, Dr. Tea Avarmaa, Dr. Martin Järvekülg, Dr. Martin Timusk, Dr. Sergei Vlassov, Dr. Jevgeni Šulga, Dr. Leonid Dorogin, Dr. Valter Reedo, Sirje Mäeorg, Maarja Pohl, Triin Kangur, Triinu Taaber, Fredrik Punga, Madis Lobjakas, Mikk Vahtrus, Mikk Antsov, Aare Floren and Margo Plaado.

I'm indescribably grateful to my family and relatives who have always believed in me and supported my studies. I would also like to thank all my friends for making my life more interesting and joyful. In doing so, you have unknowingly contributed to my work and to this thesis.

PUBLICATIONS

CURRICULUM VITAE

Name: Madis Paalo
Date of birth: 05.05.1983
Citizenship: Estonian
Contact: Institute of Physics, University of Tartu, Riia 142, 51014 Tartu
Phone: +372 511 8539
E-mail: madis.paalo@fi.tartu.ee

Education
2007–...   University of Tartu, Ph.D. student, materials science
2005–2007   University of Tartu, *magister scientiarum*i degree in organic chemistry
2001–2005   University of Tartu, *baccalaureus scientiarum*i degree in materials science
1989–2001   Toila Gümnaasium

Professional employment:
2005–...   Institute of Physics, University of Tartu, laboratory assistant, engineer, specialist
2006–2014   Estonian Nanotechnology Competence Center

Supervised dissertations:
2009   Ardi Lääne, BA in physics
2011   Triin Kangur, MSc in materials science
Currently under supervision: Mikk Vahtrus, MSc in physics

Awards:
2005   Student award of Institute of Physics, University of Tartu
2005   First award at the BA student competition of Estonian Ministry of Education and Research
2007   Student award of Institute of Physics, University of Tartu
2007   Second award at the MSc student competition of Estonian National Acadamy of Sciences

List of Publications:
1. P. Reemann, T. Kangur, M. Pook, **M. Paalo**, L. Nurmis, I. Kink, O. Porosaar, K. Kingo, E. Vasar, S. Kõks, V. Jaks, M. Järvekülg, "Fibroblast growth on micro- and nanopatterned surfaces prepared by a novel sol-gel phase separation method", Journal of Materials Science: Materials in Medicine, 2013, 24, 783–792.
2. **M. Paalo**, T. Tätte, M. Hussainov, K. Hanschmidt, M. Lobjakas, A. Lõhmus, U. Mäeorg, I. Kink, "Preparation and Characterization of CNT/TiO2 Based

Transparent Fiber Electrodes", IOP Conf. Series: Materials Science and Engineering, 2012, 38, 012023.

3. T. Tätte, M. Hussainov, **M. Paalo**, M. Part, R. Talviste, V. Kiisk, H. Män-dar, K. Põhako, T. Pehk, K. Reivelt, M. Natali, J. Gurauskis, A. Lõhmus, U. Mäeorg, "Alkoxide-based precursors for direct drawing of metal oxide micro- and nanofibres", Science and Technology of Advanced Materials, 2011 12(3), 1–12.

4. V. Kiisk, T. Kangur, **M. Paalo**, T. Tätte, S. Lange, S. Pikker, I. Sildos, "Structural and luminescence characteristics of SnO2:Eu and SnO2:Eu,Sb nanophosphors upon annealing at high temperatures", Materials Chemistry and Physics, 2011, 130(1–2), 293–298.

5. V. Kiisk, T. Kangur, **M. Paalo**, T. Tätte, S. Pikker, I. Sildos, "Optical characterization of sol-gel-derived SnO2:Eu nanopowders annealed at high temperatures", Physica Status Solidi (C), 2011, 8(9), 2641–2644.

6. M. Hussainov, T. Tätte, **M. Paalo**, J. Gurauskis, H. Mändar, A. Lõhmus, "Structure and Rheological Behavior of Alkoxide-Based Precursors for Drawing of Metal Oxide Micro- and Nanofibres", Advanced Materials Research, 2011. 214, 354–358.

7. **M. Paalo**, T. Tätte, E. Shulga, M. Lobjakas, A. Floren, A. Lõhmus, U. Mäeorg, I. Kink,. "Preparation and Characterization of Transparent Electrodes Based on CNT-s Doped Metal Oxides", Advanced Materials Research, 2011, 324, 133–136.

8. T. Tätte, M. Hussainov, J. Gurauskis, H. Mändar, G. Kelp, R. Rand, **M. Paalo**, K. Hanschmid, I. Hussainova, "Alkoxide-based precursors for direct drawing of metal oxide micro- and nanofibres", In: Technical Pro-ceedings of the 2010 NSTI Nanotechnology Conference & Expo – Nanotech 2010. Vol.2: Nanotechnology 2010: Electronics, Devices, Fabrication, MEMS, Fluidics and Computational, Anaheim, CA, USA, June 21–25, 2010. USA: Taylor & Francis, 2010, 245–248.

9. **M. Paalo**, T. Tätte, A. Juur, A. Lõhmus, U. Mäeorg, I. Kink, "Preparation of transparent electrodes based on CNT-s doped metal oxides", In: Technical Proceedings of the 2008 NSTI Nanotechnology Conference and Trade Show: NSTI Nanotechnology Conference and Trade Show 2008; Boston, USA; June 1.–5. 2008. Nano Science & Technology Institute, 2008, 389–391.

10. T. Tätte, R. Talviste, **M. Paalo**, A. Vorobjov, M. Part, V. Kiisk, K. Saal, A. Lõhmus, I. Kink, "Preparation and applications of transition metal oxide nanofibres and nanolines", In: Technical Proceedings of the 2008 NSTI Nanotechnology Conference and Trade Show: NSTI Nanotechnology Conference and Trade Show 2008; Boston, USA; June 1.–5. 2008, 2008, 109–111.

11. V. Kisand, J. Shulga, T. Tätte, U. Visk, M. Natali, G. Mistura, **M. Paalo**, M. Lobjakas, I. Kink, "Preparation of structured sol-gel films using tape

casting method", Materials Science and Engineering B-Solid State Materials for Advanced Technology, 2007, 137(1–3), 162–165.

12. T. Tätte, **M. Paalo**, V. Kisand, V. Reedo, A. Kartushinsky, K. Saal, U. Mäeorg, A. Lõhmus, I. Kink, "Pinching of alkoxide jets – a route for preparing nanometre level sharp oxide fibres", Nanotechnology, 2007, 18(2), 125301.

Patents:

G. Kelp, T. Tätte, U. Mäeorg, S. Pikker, A. Tamm, **M. Paalo**, "The method of preparation of nanocolloidal SnO2 water sol and its uses", Priority number: EE 2010-96; Priority date: 31.12.2010.

ELULOOKIRJELDUS

Nimi: Madis Paalo
Sünniaeg: 05.05.1983, Toila vald, Eesti
Kodakondsus: Eesti
Kontaktandmed: Tartu Ülikooli Füüsika Instituut, Riia 142, 51014 Tartu
Telefon: 511 8539
E-mail: madis.paalo@fi.tartu.ee

Haridus:
2007–...   Tartu Ülikool, materjaliteaduse doktorant
2005–2007   Tartu Ülikool, *magister scientiarum*i kraad orgaanilises keemias
2001–2005   Tartu Ülikool, *baccalaureus scientiarum*i kraad materjaliteaduses
1989–2001   Toila Gümnaasium, keskharidus

Teenistuskäik:
2005–...   Tartu Ülikooli Füüsika Instituut, laborant, insener, spetsialist
2006–2014   Eesti Nanotehnoloogiate Arenduskeskus AS

Juhendatud lõputööd:
2009   Ardi Lääne, bakalaureusetöö füüsikas
2011   Triin kangur, magistritöö materjaliteaduses
Praegu juhendamisel: Mikk Vahtrus, magistritöö füüsikas

Preemiad:
2005   Tartu Ülikooli Füüsika Instituudi üliõpilasstipendium bakalaureuseõppe üliõpilaste arvestuses
2005   EV Haridus – ja Teadusministeeriumi üliõpilaste teadustööde konkursi I preemia inseneri-, majandus- ja põllumajandusteaduste valdkonnas bakalaureuseõppe üliõpilaste arvestuses
2007   Tartu Ülikooli Füüsika Instituudi üliõpilasstipendium magistriõppe üliõpilaste arvestuses
2007   Eesti Teaduste Akadeemia üliõpilastööde II auhind magistriõppe astmes

Publikatsioonide loetelu:
1. P. Reemann, T. Kangur, M. Pook, **M. Paalo**, L. Nurmis, I. Kink, O. Porosaar, K. Kingo, E. Vasar, S. Kõks, V. Jaks, M. Järvekülg, "Fibroblast growth on micro- and nanopatterned surfaces prepared by a novel sol-gel phase separation method", Journal of Materials Science: Materials in Medicine, 2013, 24, 783–792.

2. **M. Paalo**, T. Tätte, M. Hussainov, K. Hanschmidt, M. Lobjakas, A. Lõhmus, U. Mäeorg, I. Kink, "Preparation and Characterization of CNT/TiO2 Based Transparent Fiber Electrodes", IOP Conf. Series: Materials Science and Engineering, 2012, 38, 012023.

3. T. Tätte, M. Hussainov, **M. Paalo**, M. Part, R. Talviste, V. Kiisk, H. Mändar, K. Põhako, T. Pehk, K. Reivelt, M. Natali, J. Gurauskis, A. Lõhmus, U. Mäeorg, "Alkoxide-based precursors for direct drawing of metal oxide micro- and nanofibres", Science and Technology of Advanced Materials, 2011 12(3), 1–12.

4. V. Kiisk, T. Kangur, **M. Paalo**, T. Tätte, S. Lange, S. Pikker, I. Sildos, "Structural and luminescence characteristics of SnO2:Eu and SnO2:Eu,Sb nanophosphors upon annealing at high temperatures", Materials Chemistry and Physics, 2011, 130(1–2), 293–298.

5. V. Kiisk, T. Kangur, **M. Paalo**, T. Tätte, S. Pikker, I. Sildos, "Optical characterization of sol-gel-derived SnO2:Eu nanopowders annealed at high temperatures", Physica Status Solidi (C), 2011, 8(9), 2641–2644.

6. M. Hussainov, T. Tätte, **M. Paalo**, J. Gurauskis, H. Mändar, A. Lõhmus, "Structure and Rheological Behavior of Alkoxide-Based Precursors for Drawing of Metal Oxide Micro- and Nanofibres", Advanced Materials Research, 2011. 214, 354–358.

7. **M. Paalo**, T. Tätte, E. Shulga, M. Lobjakas, A. Floren, A. Lõhmus, U. Mäeorg, I. Kink,. "Preparation and Characterization of Transparent Electrodes Based on CNT-s Doped Metal Oxides", Advanced Materials Research, 2011, 324, 133–136.

8. T. Tätte, M. Hussainov, J. Gurauskis, H. Mändar, G. Kelp, R. Rand, **M. Paalo**, K. Hanschmid, I. Hussainova, "Alkoxide-based precursors for direct drawing of metal oxide micro- and nanofibres", In: Technical Proceedings of the 2010 NSTI Nanotechnology Conference & Expo – Nanotech 2010. Vol.2: Nanotechnology 2010: Electronics, Devices, Fabrication, MEMS, Fluidics and Computational, Anaheim, CA, USA, June 21–25, 2010. USA: Taylor & Francis, 2010, 245–248.

9. **M. Paalo**, T. Tätte, A. Juur, A. Lõhmus, U. Mäeorg, I. Kink, "Preparation of transparent electrodes based on CNT-s doped metal oxides", In: Technical Proceedings of the 2008 NSTI Nanotechnology Conference and Trade Show: NSTI Nanotechnology Conference and Trade Show 2008; Boston, USA; June 1.–5. 2008. Nano Science & Technology Institute, 2008, 389–391.

10. T. Tätte, R. Talviste, **M. Paalo**, A. Vorobjov, M. Part, V. Kiisk, K. Saal, A. Lõhmus, I. Kink, "Preparation and applications of transition metal oxide nanofibres and nanolines", In: Technical Proceedings of the 2008 NSTI Nanotechnology Conference and Trade Show: NSTI Nanotechnology Conference and Trade Show 2008; Boston, USA; June 1.–5. 2008, 2008, 109–111.

11. V. Kisand, J. Shulga, T. Tätte, U. Visk, M. Natali, G. Mistura, **M. Paalo**, M. Lobjakas, I. Kink, "Preparation of structured sol-gel films using tape casting method", Materials Science and Engineering B-Solid State Materials for Advanced Technology, 2007, 137(1–3), 162–165.
12. T. Tätte, **M. Paalo**, V. Kisand, V. Reedo, A. Kartushinsky, K. Saal, U. Mäeorg, A. Lõhmus, I. Kink, "Pinching of alkoxide jets – a route for preparing nanometre level sharp oxide fibres", Nanotechnology, 2007, 18(2), 125301.

Patentsed leiutised:

G. Kelp, T. Tätte, U. Mäeorg, S. Pikker, A. Tamm, **M. Paalo**, "The method of preparation of nanocolloidal SnO2 water sol and its uses", Priority number: EE 2010–96; Priority date: 31.12.2010.

DISSERTATIONES SCIENTIAE MATERIALIS UNIVERSITATIS TARTUENSIS

1. **Martin Järvekülg.** Tubular microstructures by Hf-, Zr- and Ti-butoxide gel sheet rolling. Tartu, 2011, 112 p.
2. **Sergei Vlassov.** Investigation of nanoscale interactions and mechanical properties of nanostructures using quartz tuning fork based real-time measurements. Tartu, 2011, 171 p.
3. **Margus Kodu.** Pulsed Laser Deposition of Magnesium Oxide and Barium Ternary Oxides for Plasma Display Protective Layers. Tartu, 2011, 89 p.
4. **Rainer Pärna.** Surface studies of some oxide films. Tartu, 2011, 129 p.
5. **Jevgeni Šulga**. Self-assembly and interaction of nanostructures. Tartu, 2011, 114 p.
6. **Wojciech Kuznik.** Quantum-chemical computer simulations of the linear and non-linear optical properties of pyrazoloquinoline and dicyanopyrazine derivatives. Tartu, 2012, 89 p.
7. **Leonid Dorogin.** Structural and tribological properties of zero- and one-dimensional nanocrystals. Tartu, 2012, 193 p.
8. **Viljar Palmre.** Fabrication and characterization of microporous carbon-based electroactive polymer actuators. Tartu, 2012, 99 p.